2007 NSLS Science Highlights

Chemical Sciences

Condensed Matter Physics

Earth and Environmental Sciences

2007 NSLS Science Highlights

Life Sciences

Materials Science

2007 NSLS Science Highlights

New Techniques and Instrumentation

Soft Condensed Matter

Exploring High-Dielectric Materials Through a New Route

Using integrated techniques at the NSLS and the electron microscopy facility in Brookhaven s Condensed Matter Physics and Materials Science Department, a team of researchers developed a powerful method for probing materials that could help further miniaturize microelectronic components.

As electronic devices continue to shrink, so must components such as capacitors. However, past a certain size, the silicon-based material that's traditionally used to manufacture the critical electronic circuits starts to leak current and no longer performs as it does at larger scales. To prevent this effect, researchers have been searching for materials with high dielectric constants (or high-k), which enable the use of even smaller capacitors within the electronic world. One of the best materials for this purpose is called CCTO, which is made of calcium, copper, titanium, and oxygen.

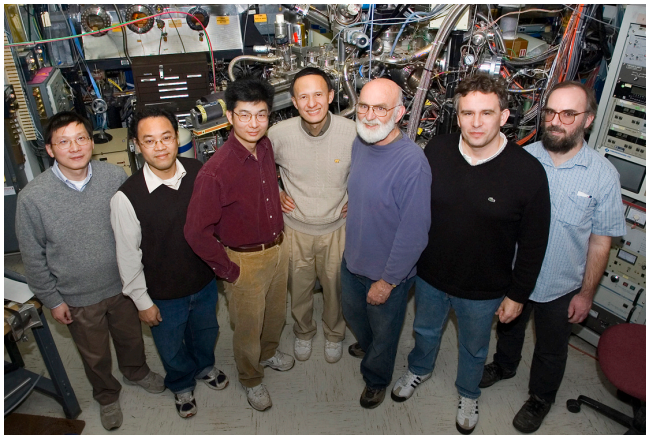

Authors (from left) Lijun Wu, Jincheng Zheng, Wei Ku, Yimei Zhu, Jonathan Hanson, Anatoly Frenkel, and Paul Northrup

"CCTO was discovered a few years ago, but only recently it was found to have one of the highest dielectric constants ever measured," said Brookhaven physicist Yimei Zhu.

Materials with a dielectric constant greater than or equal to 7 usually qualify as high-k materials. At 100,000, the dielectric constant of CCTO far surpasses that benchmark. This intriguing property offers promising technological applications, such as the miniaturization of random access memories, as well as resonators and filters for microwave and wireless communications. There's just one problem: No one could figure out why this anomaly existed. In a recent study, Zhu's team set out to find an answer.

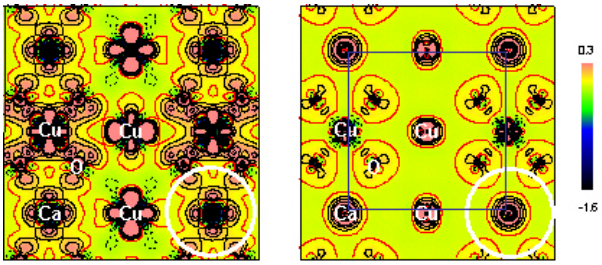

The bonding-electron distribution of CCTO containing Cu, Ca, and O atoms. (left) Experimental observation extracted from structure factor measurements using combined electron and x-ray diffraction data. (right) DFT calculation based on the ideal crystal structure.

First, using quantitative electron diffraction on single crystals of CCTO to measure valence electron distribution, the scientists identified broken symmetry in the electronic density of the material. They then further explored this nanoscale disorder with extended x-ray absorption fine structure (EXAFS) at NSLS beamlines X11A and X15B, as well as with theory calculations.

Specifically, the researchers found that a certain number of copper and calcium atoms switched positions within the material, which at least partially results in the high dielectric response. Their results were published in the July 20, 2007 issue of *Physical Review Letters*.

This type of nanoscale disorder was previously ignored

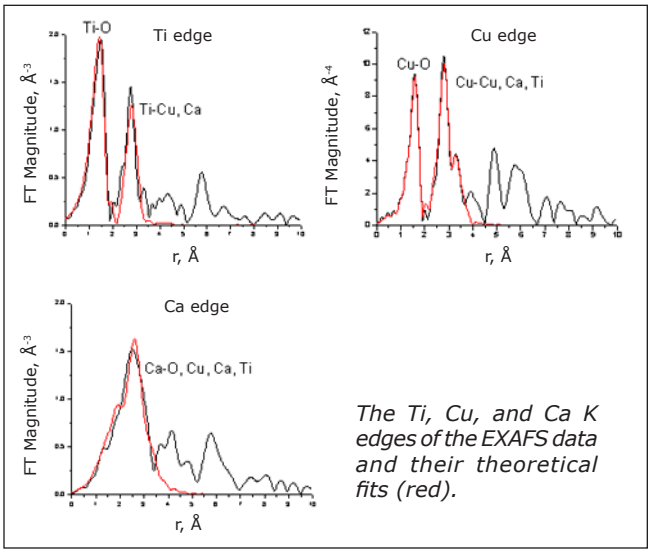

The Ti, Cu, and Ca K edges of the EXAFS data and their theoretical fits (red).

by researchers in the field because of the lack of sufficient probing tools, Zhu said.

"Our study shows how integrated experiments can work to help solve a puzzling question and also to find a new route in searching for fascinating properties of materials –especially high-dielectric ones – by tailoring local disorder and orbital symmetry," he said.

Other researchers involved were Jincheng Zheng, Lijun Wu, Jonathan Hanson, Paul Northrup, and Wei Ku, all from Brookhaven; and Anatoly Frenkel, from Yeshiva University. The research was funded by the Office of Basic Energy Sciences within the U.S. Department of Energy's Office of Science.

For more information, see: Y. Zhu, J. C. Zheng, L. Wu, A. I. Frenkel, J. Hanson, P. Northrup, and W. Ku, "Nanoscale Disorder in $CaCu_3Ti_4O_{12}$: A New Route to the Enhanced Dielectric Response," Phys. Rev. Lett., ***99****, 037602 (2007).*

— Kendra Snyder

Revealing a Key Intermediate in Green Oxidation Catalysis

As industrial processes release pollutants such as dyes, pesticides and other harmful chemicals into the Earth's water, a team of researchers is turning to a class of "green" catalysts for cleanup. Developed at Carnegie Mellon University in 1995, Fe-TAMLs – short for iron tetra-amido macrocyclic ligand activators – destroy a multitude of pollutants in water by accelerating cleansing reactions with hydrogen peroxide. Since then, researchers have worked to determine exactly how these processes work, and recently, they figured out another piece of that puzzle. Through studies that included EXAFS investigations at the NSLS, researchers from CMU and the University of Minnesota have isolated and characterized a species thought to be a key intermediate in the Fe-TAML reaction with peroxides and oxygen.

Authors (top, from left) Deboshri Banerjee, Emile Bominaar, Arani Chanda, and Terry Collins, (bottom, from left) Sujit Mondal, Eckard Münck, Filipe Tiago de Oliveira, and Lawrence Que

The results of the study, published in the February 9, 2007, issue of *Science*, lend weight to the theory that Fe-TAML catalysts work by separating hydrogen peroxide into water and an oxygen atom that is bound to the iron of the Fe-TAML. The resulting Fe-TAML-oxo complex then destroys undesirable molecules, rendering them less toxic and often proceeding to mineralization or near-mineralization. The inventor of these extremely active catalysts, CMU's Terry Collins, describes Fe-TAML reactions as "fire in water," because the activated peroxide carries out chemistry on many (but not all) carbon-containing compounds where the products resemble those of combustion.

Because of this high reactivity, the catalyst's developers had to build ligand systems that allow for the formation of iron-oxo complexes from the Fe-TAML activators without being rapidly destroyed by the highly reactive intermediates they enable.

The stable form of the iron used in the Fe-TAML starting catalyst complex is Fe(III), the state of iron found naturally in rust. However, during the reaction between peroxides and an Fe-TAML activator, the iron's oxidation state has been shown to pass through an Fe(IV) species and then proceed onto an Fe(V) species. This Fe(V)-oxo complex is thought to be a key reactive intermediate in Fe-TAML oxidation catalysis.

"For about the last 10 years, I've been convinced that the Fe(V)-oxo group existed," said Collins, the director of the Institute for Green Oxidation Chemistry at CMU's Mellon College of Science. "Proving it was another matter."

Atoms with high oxidation states, such as Fe(IV) and Fe(V), are difficult to trap because they're so reactive. In order to "catch" the Fe(V)-oxo group, the researchers set up a system in an organic solvent at a very low temperature (about –60 °C) because water's high freezing point prevented its use. They then titrated it in a very reactive peroxide.

Using x-ray absorption spectroscopy at NSLS beamline X3B, University of Minnesota researcher Lawrence Que's group combined with Collins' group and CMU's Mössbauer, EPR, and theory group (led by Eckard Münck) to reveal the long-sought chemical and electronic properties of the intermediate. This is the first characterization of an Fe(V)-oxo complex.

"This was a great challenge, and we've gotten to the top of this mountain," Que said. "Knowing these properties increases our ability to carry out the oxidation of compounds and helps us understand how iron agents might be working in environmental remediation."

That includes an increased knowledge about Collins' Fe-TAML catalysts, which have been demonstrated for a variety of uses including cleaning up water polluted at textile, pulp, and paper mills; removing sulfur from diesel fuel; destroying traces of endocrine-disrupting

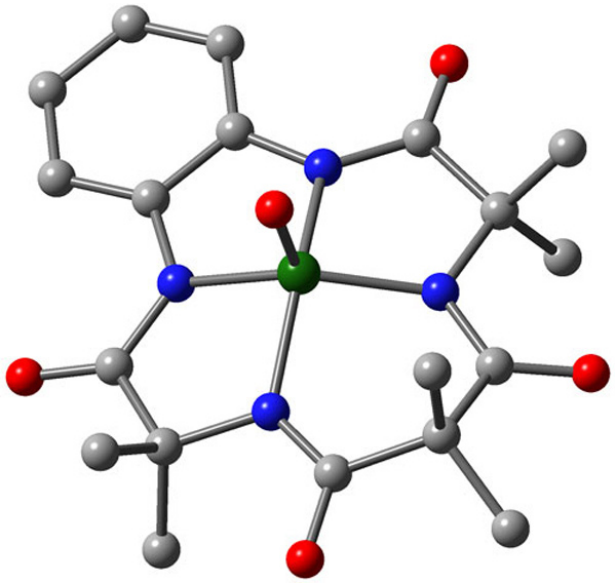

The structure of the Fe(V)-oxo complex (green, iron; red, oxygen; blue, nitrogen; and gray, carbon.) For clarity, hydrogen atoms are not shown.

chemicals in water; killing anthrax spores and other water-borne infectious microbes; and even stopping dark-colored laundry from staining whites and lights in the wash.

This research was supported by the National Institutes of Health, the Heinz Endowments, the Environmental Protection Agency, and the Heinz Family Foundation for the Teresa Heinz Scholars for Environmental Research Award. Other researchers include Filipe Tiago de Oliveira, Arani Chanda, Deboshri Banerjee, Sujit Mondal, and Emile Bominaar, all from Carnegie Mellon University; and Xiaopeng Shan, from the University of Minnesota.

For more information, see: F. Tiago de Oliveira, A. Chanda, D. Banerjee, X. Shan, Sujit Mondal, L. Que, Jr., E.L. Bominaar, E. Münck, and T.J. Collins,"Chemical and Spectroscopic Evidence for an FeV-Oxo Complex," Science, ***315****, 835-838 (2007).*

— Kendra Snyder

Featured Highlight

Brookhaven Lab Scientists Discover Gold Clusters Stabilize Platinum Electrocatalysts For Use in Fuel Cells

Platinum is the most efficient electrocatalyst for accelerating chemical reactions in fuel cells for electric vehicles. In reactions during the stop-and-go driving of an electric car, however, the platinum dissolves, which reduces its efficiency as a catalyst. This is a major impediment for vehicle-application of fuel cells.

Now, scientists at the U.S. Department of Energy's Brookhaven National Laboratory have overcome this problem. Under lab conditions that imitate the environment of a fuel cell, the researchers added gold clusters to the platinum electrocatalyst, which kept it intact during an accelerated stability test. This test is conducted under conditions similar to those encountered in stop-and-go driving in an electric car. The research is reported in the January 12, 2007, edition of the journal *Science*.

Brookhaven's Chemistry Department researchers Junliang Zhang, Kotaro Sasaki, and Radoslav Adzic, along with Eli Sutter from Brookhaven's Center for Functional Nanomaterials, authored the research paper. "Fuel cells are expected to become a major source of clean energy, with particularly important applications in transportation," said coauthor Radoslav Adzic. "Despite many advances, however, existing fuel-cell technology still has drawbacks, including loss of platinum cathode electrocatalysts, which can be as much as 45 percent over five days, as shown in our accelerated stability test under potential cycling conditions. Using a new technique that we developed to deposit gold atoms on platinum, our team was able to show promise in helping to resolve this problem. The next step is to duplicate results in real fuel cells."

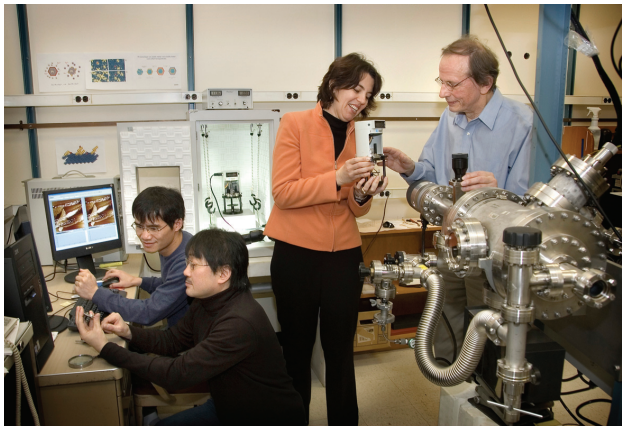

(Clockwise) Brookhaven Lab researchers Kotaro Sasaki, Junliang Zhang, Eli Sutter and Radoslav Adzic view gold clusters on a single-crystal platinum surface using a scanning tunneling microscope.

A hydrogen-oxygen fuel cell converts hydrogen and oxygen into water and, as part of the process, produces electricity. Platinum electrocatalysts speed up oxidation and reduction reactions. Hydrogen is oxidized when electrons are released and hydrogen ions are formed; the released electrons supply current for an electric motor. Oxygen is reduced by gaining electrons, and in reaction with hydrogen ions, water, the only byproduct of a fuel cell reaction, is produced.

In the unique method developed at Brookhaven, the researchers displaced a single layer of copper with gold on carbon-supported platinum nanoparticles. After being subjected to several sweeps of 1.2 volts, the gold monolayer transformed into three-dimensional clusters. Using x-rays as probes at beamlines X11B, X18B, and X19A at Brookhaven's National Synchrotron Light Source, a scanning transmission microscope at Brookhaven's Center for Functional Nanomaterials, and electrochemical techniques in the laboratory, the scientists were able to verify the reduced oxidation of platinum and to determine the structure of the resulting platinum electrocatalyst with gold clusters, which helped them to gain an understanding of the effects of the gold clusters.

In the Brookhaven experiment, the platinum electrocatalyst remained stable with potential cycling between 0.6 and 1.1 volts in over 30,000 oxidation-reduction cycles, imitating the conditions of stop-and-go driving. "The gold clusters protected the platinum from being oxidized," Adzic said. "Our team's research raises promising possibilities for synthesizing improved platinum-based catalysts and for stabilizing platinum and platinum-group metals under cycling oxidation/reduction conditions."

This research is funded through the U.S. Department of Energy's Hydrogen Program, which implements the President's Hydrogen Fuel Initiative, a five-year program that began in 2003 to sponsor research, development, and demonstration of hydrogen and fuel cell technologies. Specifically, the funding derived from DOE's Office of Basic Energy Sciences and its Office of Energy Efficiency and Renewable Energy.

*For more information, see: J. Zhang, K. Sasaki, E. Sutter, and R. R. Adzic, "Stabilization of Platinum Oxygen-Reduction Electrocatalysts Using Gold Clusters," Science, **315**, 220-222 (2007).*

— Diane Greenberg

BEAMLINES
X19A, X9B

PUBLICATION
S. Chaudhuri, J. Graetz A. Ignatov, J. J. Reilly, and J. T. Muckerman, "Understanding the Role of Ti in Reversible Hydrogen Storage as Sodium Alanate: A Combined Experimental and First-Principles Theoretical Approach" *J. Am. Chem. Soc.*, **128,** 11404 (2006).

FUNDING
U.S. Department of Energy Office of Basic Energy Sciences

FOR MORE INFORMATION
Jason Graetz, Brookhaven National Laboratory, Energy Sciences and Technology
graetz@bnl.gov

Hydrogen-Mediated Metal Transport in Complex Metal Hydrides

S. Chaudhuri[1], J. Graetz[2], A. Ignatov[3], J.J. Reilly[2], and J.T. Muckerman[1]

[1]Chemistry Department, Brookhaven National Laboratory; [2]Department of Energy Sciences and Technology, Brookhaven National Laboratory; [3]National Synchrotron Light Source, Brookhaven National Laboratory

X-ray absorption spectroscopy and density functional theory (DFT) were used to investigate the titanium environment and the role of metal catalysts in sodium alanate. Titanium atoms were found near the surface, coordinated by a shell of aluminum at a distance of 2.82 Å. Combined DFT and molecular dynamics simulations at 450 K reveal a similar local Ti environment. These results suggest that the role of Ti may be linked entirely to active catalytic sites in the metallic Al phase. The formation and migration of transient alane species is proposed as a plausible mechanism for the long-range aluminum transport that occurs during hydrogen cycling.

The demonstration of reversible hydrogen cycling in Ti-catalyzed sodium aluminum hydride has generated considerable interest in the complex metal hydrides. The reversible (de)hydrogenation occurs through a two-step reaction:

$$NaAlH_4 \leftrightarrow 1/3Na_3AlH_6 + 2/3Al + H_2 \leftrightarrow NaH + Al + 3/2H_2 \quad (1)$$

Since this discovery, a number of studies have looked at improving the catalytic effects and understanding the role of additives in H_2 cycling. However, the mechanism by which $NaAlH_4$ is activated in the presence of a small amount of a transition metal is still not well understood. One of the principle questions is "How do the Al atoms migrate the *long* distances required during the hydrogenation reaction?" In this study we investigate the atomistic transport mechanisms of the reversible complex metal hydrides using x-ray absorption spectroscopy and first-principles calculations.

The extended and near-edge structure of the Ti K-edge were used to explore the local titanium environment and valence in catalyzed sodium alanate. An estimate of the oxidation state of the dopant, based upon known standards, revealed a zero-valent titanium atom. Analysis of the near-edge and extended fine structures indicates that the Ti does not enter substitutional or interstitial sites in the $NaAlH_4$ lattice. Rather, the Ti is located on or near the surface and is coordinated by 10.2±1 Al atoms with an interatomic distance of 2.82±0.01 Å, similar to that of $TiAl_3$. The Fourier transformed EXAFS spectra revealed a highly disordered distribution of Ti-Al distances with no long-range order beyond the second coordination sphere. The similarity of the spectra in the hydrogenated and dehydrogenated samples suggests that the local Ti environment is nearly invariant during hydrogen cycling. A plot of the Ti pair distribution function is shown in **Figure 1**.

Density functional theory was used to calculate the chemical potential of Ti on an Al(001) surface with 0.125 - 0.5 monolayer coverage. Active sites that chemisorb H_2 via spontaneous or only moderately activated pathways were identified. Although Al metal has a low affinity for molecular hydrogen, when doped with 2-4% Ti the surface characteristics change significantly. The computational model identifies and ranks a host of metastable sites that promote hydrogen chemisorption at low energy costs and act as atomic-level pumps that produce atomic hydrogen. One plausible mechanism for the long-range Al transport is through migration of an aluminum hydride species (alane). Although the proposed alane clusters are

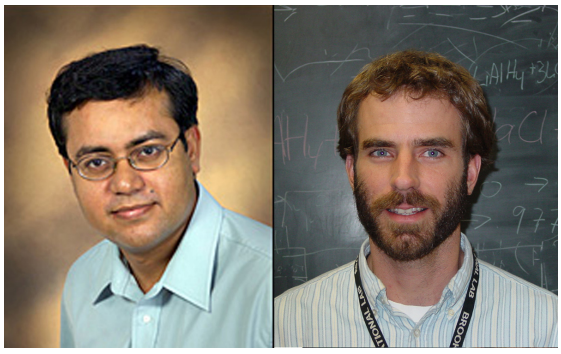

Authors (from left) Santanu Chaudhuri and Jason Graetz

difficult to observe experimentally, the stability and mobility of alanes on Al(001) were studied through temperature-dependent molecular dynamics simulations. The results indicate that larger clusters (e.g. Al_2H_6 and Al_3H_9) quickly break down to AlH_3 (and AlH_x + H) on Al(001) as shown in **Figure 2**. Therefore, the Al transport likely occurs via small clusters (e.g. AlH_3) with high diffusion rates (3×10^5 cm/s for AlH_3) driven by thermal vibrations. This work also demonstrates the that the metastable active sites progressively transform into the more stable, but less active $TiAl_3$ alloy with H_2 cycling. Therefore, maintaining well-dispersed Ti within the Al phase will be essential to mitigating capacity fade during cycling.

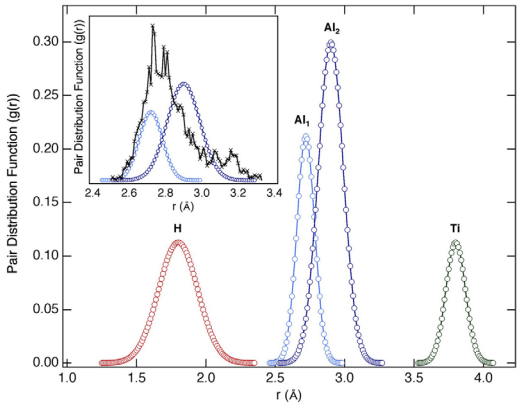

Figure 1. *Pair distribution function determined from EXAFS data on 2 mol % Ti-catalyzed $NaAlH_4$ (hydrogenated) and corrected for the phase shift. The inset shows a comparison of predicted and experimental distribution functions for Ti-Al pairs.*

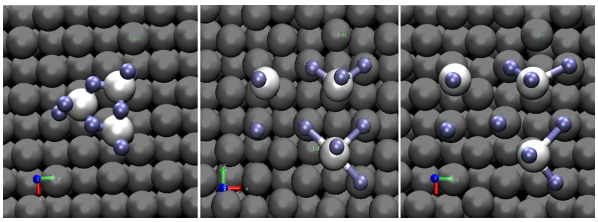

Figure 2. *Dissociation and diffusion of an Al_3H_9 cluster on an Al(001) surface showing formation of smaller fragments including a stable AlH_4 and AlH_3 cluster.*

BEAMLINE
X24A

PUBLICATION
P.S. Lysaght, G.I. Bersuker, J. Barnett, J.C. Woicik, D.A. Fischer, B. Foran, H-H. Tseng, and R. Jammy "Chemical Analysis of HfO_2/ Si (100) Film Systems Exposed to NH_3 Thermal Processing," *J. Appl. Phys.*, **101**, 024105 (2007).

FUNDING
National Institute of Standards and Technology (NIST)

FOR MORE INFORMATION
Patrick Lysaght, SEMATECH
pat.lysaght@sematech.org

Joseph Woicik, NIST
Woicik@nist.gov

SEMATECH and NIST Collaborate on Chemical Analysis of Advanced Gate Dielectrics

P. S. Lysaght[1], J.C. Woicik[2], D.A. Fischer[2], G.I. Bersuker[1], J. Barnett[1], B. Foran[3], H-H. Tseng[1], and R. Jammy[1]

[1]SEMATECH; [2]National Institute of Standards and Technology; and [3]The Aerospace Corporation

Nitrogen incorporation in thin HfO_2/SiO_2 film systems representative of high-κ gate dielectric layers in advanced metal-oxide semiconductor field-effect transistors (MOSFETs) has been investigated by synchrotron x-ray photoelectron spectroscopy to elucidate variations in chemical composition between samples annealed in NH_3 and N_2 ambient as a function of temperature. In addition, depth profiling of core-level binding energy spectra has been obtained by variable kinetic energy x-ray photoelectron spectroscopy (VKE-XPS) with tunable photon energy. An HfO_2/SiO_2 "interface effect" has been detected in the Si 1s spectra characterized by a shift of the Si^{4+} feature to lower binding energy with no corresponding chemical state change observed in the Hf 4f spectra acquired over a broad range of electron take-off angles.

One of the semiconductor industry's "grand challenges" is to develop an alternative to the SiO_2 gate dielectric that has enabled scaling (increasing integrated circuit device density, according to Moore's Law) of metal-oxide semiconductor field-effect transistors (MOSFETs) for the past 40 years. The challenge originates from the quest for integrated circuits exhibiting higher speed and lower power consumption, no longer attainable with ultra-thin (sub 2 nm) SiO_2 gate dielectrics due to their high direct tunneling leakage currents. This initiative has given rise to extensive evaluation of Hf-based oxide thin films as promising high permittivity (high-*k*) replacement material that provides a physically thicker film with lower leakage current characteristics for equivalent SiO_2 capacitance. However, intrinsic properties of hafnia, HfO_2, do not satisfy all requirements for gate dielectrics, particularly, crystallization temperature, defect density, and ion diffusivity. Modification of the hafnia structure has been undertaken by various alloying efforts including nitrogen incorporation to enhance electrical performance.

Thin (3 nm) HfO_2 blanket films deposited by atomic layer deposition on either SiO_2- or NH_3-treated Si (100) substrates have been subjected to NH_3 and N_2 anneal processing. High-resolution NIST measurements of synchrotron x-ray photoelectron spectroscopy (XPS) were coupled with grazing incidence x-ray diffraction (GIXRD) and electron energy loss spectroscopy (EELS) measurements to elucidate differences in chemical composition and crystalline structure resulting from anneal processing in NH_3 and N_2 ambient as a function of temperature to identify physical evidence for process-dependent transistor performance. Variable kinetic energy XPS (VKE-XPS), achieved via the tunable photon energy capability of synchrotron radiation, was utilized to obtain bulk thin film and interface depth profiling of the core-level electron binding energy spectra.

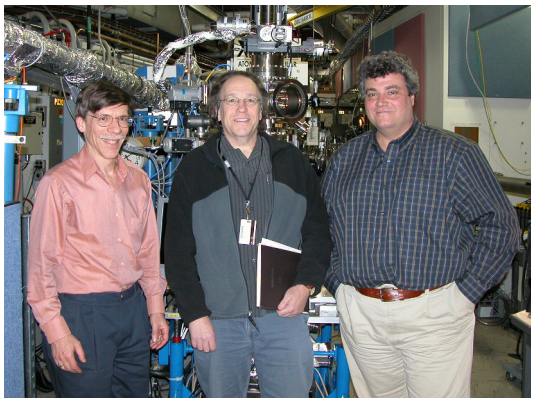

Authors (from left) Dan Fischer, Patrick Lysaght, and Joseph Woicik

An "interface effect" characterized by a shift of the Si^{4+} feature to lower binding energy at the HfO_2/SiO_2 interface has been detected in the Si 1*s* spectra illustrated in **Figure 1**. However, no corresponding chemical state change was observed in the Hf 4*f* spin-orbit energy spectra acquired over a broad range of electron take-off angles and surface sensitivities, thereby ruling out the likelihood of Hf silicate formation at the interface. The hafnia film has been shown to getter oxygen from the underlying SiO_2, thereby

rendering it substoichiometric (oxygen deficient) in the neighborhood of the interface with HfO_2.

The NH_3 anneal ambient has been shown to produce a metastable Hf-N bond component in the Hf 4*f* XPS spectra corresponding to temperature-driven dissociation kinetics while the Si 2*p* spectra indicate Si-N bond formation near the HfO_2 layer in samples exposed to 700°C/60s/NH_3 anneal. GIXRD measurements identify corresponding structural changes resulting from NH_2 (isoelectronic with O) exchange for oxygen in these HfO_2 films, although not detected in samples exposed to anneal processing in N_2 ambient. These findings are consistent with elemental profiles across the HfO_2/SiO_2/Si(100) interface determined by EELS measurements.

These SEMATECH-NIST results represent a major step toward the controlled optimization of Hf-based gate dielectrics and the development of next-generation MOSFET devices.

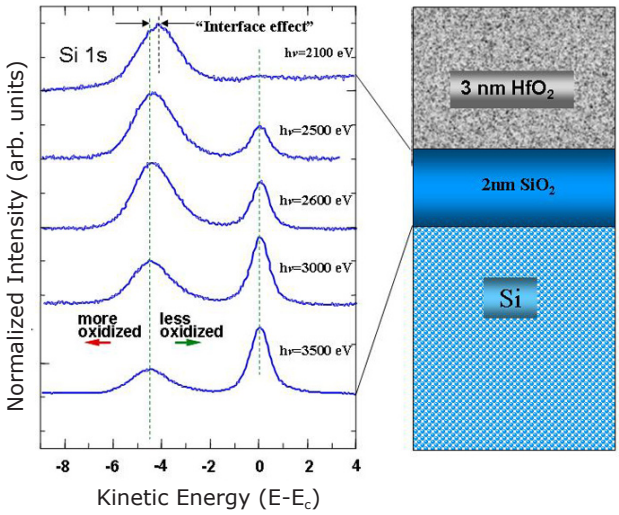

Figure 1. *Si 1s spectra from 3nm HfO_2/ 2nm SiO_2 sample recorded with variable kinetic energy XPS illustrates depth profiling sensitivity and an interface effect near HfO_2*

Researchers Discover Surface Orbital "Roughness" in Manganites

At the NSLS, researchers have shown that in a class of materials called manganites, the electronic behavior at the surface is considerably different from that found in the bulk. Their findings, which were published online in the November 18, 2007, issue of *Nature Materials* and could have implications for the next generation of electronic devices, which will involve increasingly smaller components.

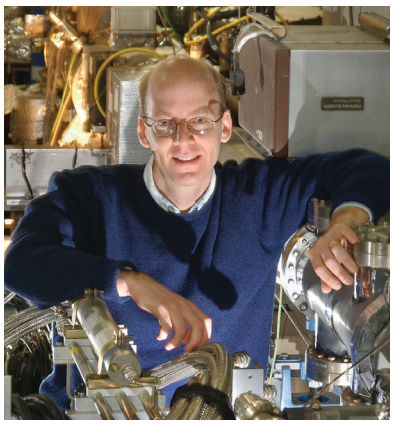

John Hill

As devices shrink, the proportion of surface area grows in comparison to the material's volume. Therefore, it's important to understand the characteristics of a material's surface in order to predict how those materials behave and how electrons will travel across an interface, said Brookhaven physicist John Hill.

Hill and his fellow researchers were particularly interested in how the outer electrons of atoms in a so-called manganite material are arranged. Manganites – consisting of a rare-earth element such as lanthanum combined with manganese and oxygen – show a huge change in electrical resistance when a magnetic field is applied. Taking advantage of this "colossal magnetoresistance effect" could be the key to developing advanced magnetic memory devices, magnetic field sensors, or transistors.

The research team, which also includes scientists from KEK (Japan), CNRS (France), Ames Laboratory, and Argonne National Laboratory, used x-ray scattering at NSLS beamlines X22C and X21 and Argonne's Advanced Photon Source to study the orbital order — the arrangement of electrons in the outermost shell — of the material at the surface and in its bulk.

"When you cool down the bulk material to a particular temperature, all the orbitals arrange themselves in a very particular pattern," Hill said. "The question is, does the same thing happen at the surface? And if not, how is it different?"

The authors found that at the surface, the orbital order is more disordered than in the bulk material. And, even though the manganite's crystal surface is atomically smooth, the orbital surface is rough. These characteristics could affect the way electrons are transferred across a material's surface and provide fundamental information for future research and development. Next, the researchers plan to look for this surface orbital "roughness" in other materials and test its effect on magnetism.

Funding for this research was provided by the Office of Basic Energy Sciences within in the U.S. Department of Energy's Office of Science.

*Y. Wakabayashi, M. Upton, S. Grenier, J. Hill, C. Nelson, J. Kim, P. Ryan, A. Goldman, H. Zheng, and J. Mitchell, "Surface Effects on the Orbital Order in the Single-Layered Manganite $La_{0.5}Sr_{1.5}MnO_4$," Nat. Mater., **6**, 972-976.*

— Kendra Snyder

Illuminating a Second "Kink" in High-Tc Superconductors

There's another kink in the mystery of high-temperature (Tc) superconductors – literally. Using photoemission studies at the NSLS, a group of researchers has revealed a new anomaly, or "kink," in

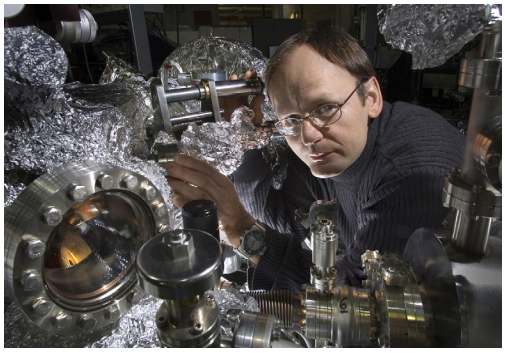

Tonica Valla

the energy spectrum of high-energy electrons in two different families of cuprate superconductors, further complicating their quest to discover exactly how the materials conduct electricity with zero resistance

In 1999, a group of researchers led by BNL physicist Tonica Valla discovered a low-energy kink in the energy bands of electrons in high-Tc superconductors just as they went through the transition temperature from their normal to superconducting state. This spectral abnormality is thought to be signature of an interaction or "coupling" between an electron and an excitation such as a phonon, which is a vibration of the ions that form the lattice of a superconductor's crystal.

"In conventional low-temperature superconductors, this is really the interaction that causes superconductivity," Valla said. "And there was a hope that when we saw a similar kink in high-temperature superconductors that maybe the mechanism of superconductivity would be resolved. But it's not that easy."

While some groups hold that the mechanism is the same as in conventional superconductors — that is, that phonons are responsible for electron pairing – other scientists believe that changes in the spin alignment, or magnetic polarity (magnons), of adjacent electrons are responsible. However, because both excitations are found in the energy range of the low-energy kink – between 40 and 70 meV – it's difficult to determine which mechanism is correct.

And recently, Valla's group has thrown another complication into the mix, unveiling a second and

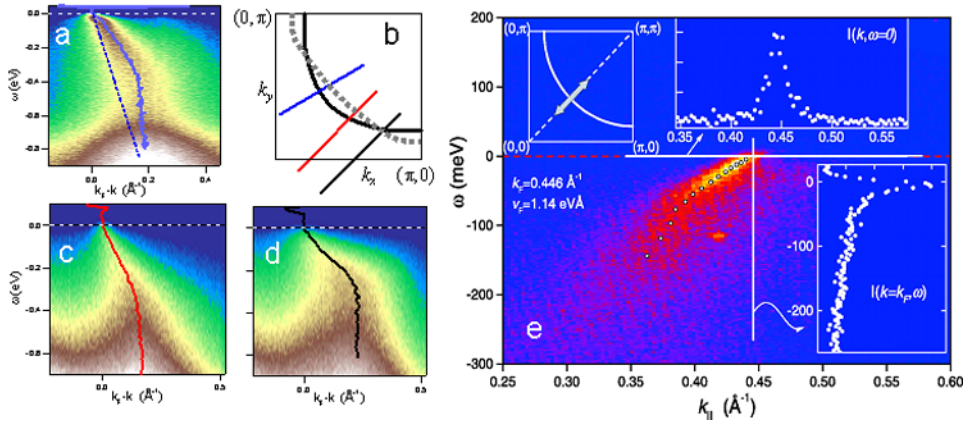

Figure caption: "Big kink" (left) vs. "small kink" (right). a) OP91 BSCCO (T=10K). b) Brillouin zone (BZ) and Fermi surface (FS) for BSCCO (solid line) and LBCO (dashed line). Straight lines represent the momentum lines probed in the spectra with correspondingly colored dispersion. c) and d) LBCO spectra at x=0.125 for two different momentum lines as indicated in b). e) ARPES intensity from the nodal line in superconducting state in optimally doped BSCCO. The velocity or rate of dispersion changes in the vicinity of the Fermi level, resulting in a "kink" in dispersion at ~60 meV bellow the Fermi level. "Small kink" image from "Evidence for Quantum Critical Behavior in the Optimally Doped Cuprate $Bi_2Sr_2CaCu_2O_{8+d}$" T. Valla, A. V. Fedorov, P. D. Johnson, B. O. Wells, Q. Li, G. D. Gu, and N. Koshizuka, Science 285, 2110 (1999).

much larger kink in the high-Tc superconductors "LBCO" (named for the elements it contains: lanthanum, barium, copper, and oxygen) and "BSCCO" (containing bismuth, strontium, calcium, copper, and oxygen). Using high-resolution spectrometers at NSLS beamline U13UB, Valla's group measured the energy and the angle at which the electrons were emitted from the superconducting crystals, allowing them to reconstruct the original electrons' state. This time around, the research team found a large anomaly in the energy spectrum of the materials at 350 meV, the details of which are published in the April 20 edition of *Physical Review Letters*.

"It was a piece of cake to see because it's so huge, but you have to look deep enough," Valla said, adding that the lower energy kink makes just a small contribution to the total kink. "Now, the question is, 'What's the cause of this big one?'"

Because they only exist at lower energies, the researchers immediately ruled out phonons as a possible culprit. In fact, Valla's group now believes that both the large and small kinks are caused by something different: spin fluctuations. This excitation occurs when the spin of one atom is changed, causing a domino effect as its neighbors flip in order to get back into the proper alignment, whether its ferromagnetic (spins pointing in the same direction) or antiferromagnetic (spins pointing in opposite directions). Spin fluctuations occur at up to 400 meV, and they appear to die out when a material's superconductivity disappears, providing a further link for their involvement in the mechanism of high-Tc superconductors.

"For conventional superconductors, it is clear that the observation of a kink is related to superconductivity," Valla said. "In high-Tcs we are seeing kinks all over the place and some of them might also be closely related to superconductivity. Maybe the low-energy kink is the only important one, but it also might be that the total interaction at higher energies is important as well."

Valla said that future studies will extend to other materials to verify that the high-energy kink is present in all high-Tc cuprate superconductors and to further investigate the role of spin fluctuations in the system.

Other researchers involved in the work include Tim Kidd (BNL and the University of Northern Iowa), Weiguo Yin, Genda Gu, and Peter Johnson (BNL), and Zhihui Pan and Alexei Fedorov (Lawrence Berkeley National Laboratory). Their work was supported by the Office of Basic Energy Sciences within the U.S. Department of Energy's Office of Science.

For more information, see: T. Valla, T.E. Kidd, W.-G. Yin, G.D. Gu, P.D. Johnson, Z.-H. Pan, and A.V. Fedorov, "High-Energy Kink Observed in the Electron Dispersion of High-Temperature Cuprate Superconductors," Phys. Rev. Lett., ***98****, 167003 (2007).*

— Kendra Snyder

Studying Magnetic Interface Ferromagnetism

The development of various magnetic-based devices, such as read-heads found inside your computer, depends on the discovery and improvement of new materials and magnetic effects. In particular, researchers are interested in the magnetic behavior at the interfaces between different materials, especially in devices presenting so-called "exchange bias"– an effect produced by combining ferromagnetic and antiferromagnetic materials. Because these materials sometimes have very small magnetizations, characterizing them at atomic- and nanometer-length scales isn't easy. However, using soft x-ray resonant magnetic scattering at the NSLS, a group of researchers has found a way to investigate how magnetism varies with the depth of a thin layer of material, specifically at the interface.

Cecilia Sánchez-Hanke

Sujoy Roy

Many new state-of-the-art materials and devices for magnetic reading and writing rely on the interplay between different magnetic properties. This is especially true for quantum mechanical spins, the origin of the atoms' magnetic behavior. In a ferromagnet, the atoms' magnetic moments are aligned in parallel, whereas in an antiferromagnet, the moments are antiparallel. The coupling between an antiferromagnetic and a ferromagnetic material may give rise to exchange bias, which locks the ferromagnet spins (a major contributor to the magnetic moment). This effect is of fundamental importance to modern magnetic devices since it forms a reference layer with a fixed direction of magnetization.

This is not a new concept," said lead researcher Sujoy Roy, from the University of California, San Diego. "It's very important for technology and extensively used in spintronic-based devices."

However, there are still ongoing controversies about the microscopic origin of exchange bias. Previous studies have revealed the existence of "unpinned spins" (spins in one direction not matched by an opposite spin and responding to applied field) at the antiferromagnetic interface. To examine how these spins are distributed and how they interact with the ferromagnetic spins across the interface, the researchers determined the depth dependence of the net magnetization in an exchange-biased sample consisting of permalloy, a nickel iron magnetic alloy (the ferromagnet) and cobalt oxide (the antiferomagnet). This was done at room temperature, where no "pinned" spins exist in the antiferromagnet and the exchange bias does not occur.

"Not many instruments can do this," Roy said. "You can use microscopes to look at the surface of a material, but we wanted to scan the films from top to bottom, especially the interface."

To do this, the researchers used x-ray reflectometry at NSLS beamline X13A and magnetometry at University of California, San Diego. These techniques allowed them to determine the distributions of free spins and of spin orientation, providing an atomic-level picture of the exchange bias mechanism.

"This was a very unique method," Roy said. "We have been able to pinpoint exactly how the magnetism is varying as a function of depth in absolute units."

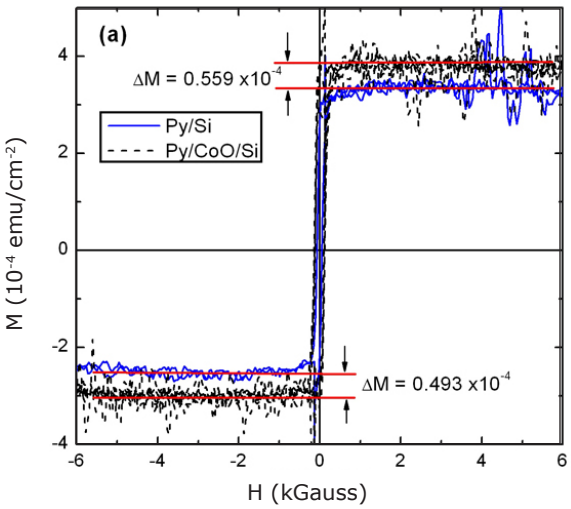

Room temperature hysteresis measurements for same thickness of Py deposited on Si (blue) and CoO/Si (black dashed). Red lines indicate the magnetization value at the positive and negative saturation for Py/Si and Py/CoO/Si, respectively.

The team found that a region at the permalloy/cobalt oxide interface is modified both chemically and magnetically. This modification is due to the formation of an oxide layer containing both cobalt and permalloy in between the bilayer. While there is no significant magnetization in the cobalt oxide, the temperature dependence of the interfacial layer's net magnetization is different than the permalloy. Their results were published in the January 31, 2007 edition of *Physical Review B*.

The magnetization in this interfacial region, and how it interacts with the antiferromagnetic spins in the cobalt oxide at low temperatures, is expected to play a key role in determining the exchange bias properties of this bilayer. Future work will repeat the experiment at lower temperatures, where exchange bias develops in the sample, in order to determine how the interface properties change.

Other researchers include Cecilia Sánchez-Hanke and Chi-Chang Kao (NSLS); Sungkyun Park (Los Alamos National Laboratory and Korea Basic Science Institute); Mike Fitzsimmons (Los Alamos National Laboratory); Sunil Sinha (University of California, San Diego, and Los Alamos National Laboratory); Y. Tang, Jung-Il Hong, Xuerong Liu, M. Brian Maple, and Ami Berkowitz (University of California, San Diego); and David Smith (Arizona State University).

This research was supported by the Office of Basic Energy Sciences within the U.S. Department of Energy's Office of Science.

For more information, see: S. Roy, C. Sanchez-Hanke, S. Park, M.R. Fitzsimmons, Y.J. Tang, J.I. Hong, David J. Smith, B.J. Taylor, X. Liu, M.B. Maple, A.E. Berkowitz, C.-C. Kao, and S.K. Sinha, "Evidence of Modified Ferromagnetism at a Buried Permalloy/CoO Interface at Room Temperature," Phys. Rev. B, ***75****, 014442 (2007).*

— Kendra Snyder

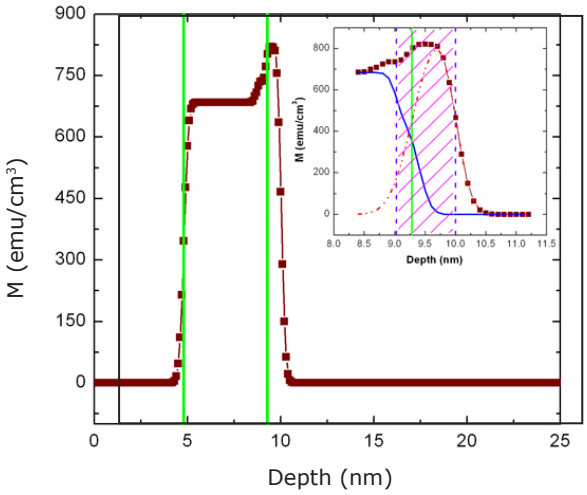

Depth-dependent magnetic density profile in absolute units in a Py/CoO bilayer system. Green solid lines represent structural/chemical interfaces. The inset shows the Py/CoO interface region where the structural and magnetic features are modified. Solid blue and dashed-dot red curves represent the individual Py and CoO contribution to the net magnetization. The hatched area within violet dashed lines represents the magnetic interface between Py and CoO.

BEAMLINE
X17C

PUBLICATION
A.B. Papandrew, M.S. Lucas, R. Stevens, B. Fultz, I. Halevy, M.Y. Hu, P. Chow, R.E. Cohen, and M. Somayazulu, "Absence of Magnetism in Hcp Iron-Nickel at 11 K," *Phys. Rev. Lett.*, **97**, 087202 (2006).

FUNDING
U.S. Department of Energy

FOR MORE INFORMATION
Alexander B. Papandrew, Division of Engineering and Applied Science, California Institute of Technology
ap@caltech.edu

Absence of Magnetism in HCP Iron-Nickel at 11 K

A.B. Papandrew[1], M.S. Lucas[1], R. Stevens[1], B. Fultz[1], I. Halevy[2], M.Y. Hu[3], P. Chow[3], R.E. Cohen[4], and M. Somayazulu[5]

[1]Division of Engineering and Applied Science, California Institute of Technology; [2]Physics Department, Nuclear Research Center, Israel; [3]HP-CAT, Carnegie Institution of Washington, Advanced Photon Source, Argonne National Laboratory; [4]Carnegie Institution of Washington; [5]Geophysical Laboratory, Carnegie Institute of Washington

Density functional theoretical (DFT) calculations predict an antiferromagnetic ground state for the high-pressure hcp phase of Fe and for hcp Fe-Ni. We performed synchrotron Mossbauer spectroscopy (SMS) on an hcp-phase $Fe_{92}Ni_8$ alloy at 28 GPa and 11 K. The SMS spectrum showed no hyperfine magnetic field, in disagreement with the DFT calculations. Our results are consistent with significant errors in the GGA density functional, leading to an erroneous prediction of a large HMF. Alternately, these results indicate the presence of quantum fluctuations with periods shorter than the lifetime of the nuclear excited state, prohibiting the detection of magnetism by the SMS technique.

Elemental iron, which has the body-centered cubic (bcc) crystal structure at ambient temperature and pressure, transforms to the hexagonal-close packed (hcp) phase at a pressure of approximately 13 GPa. An antiferromagnetic (AFM) ground state has been predicted repeatedly for the hcp phase, but experiments have never detected the presence of a hyperfine magnetic field (HMF), related to the net spin density at the nucleus, implying the absence of static magnetic moments or magnetic order. Recent density functional theory (DFT) calculations have suggested that the vanishing HMF in hcp iron can be explained by cancellation of a large core electron polarization by an equally large itinerant electron polarization in the antiferromagnetic state. DFT calculations for the AFM structure have shown markedly better agreement with equation of state and elasticity measurements than nonmagnetic calculations. We tested the idea that ε-iron is antiferromagnetic, yet exhibits no hyperfine field owing to the cancellation of up and down spin densities at its nuclei. If indeed such a balance between core and conduction electron polarization exists, a magnetic perturbation should disrupt it, producing measurable hyperfine magnetic fields.

An alloy of nominal composition $Fe_{92}Ni_8$ was made by arc-melting. High-pressure energy-dispersive x-ray diffraction (EDXRD) was performed at NSLS beamline X17C to identify the pressure of the bcc to hcp phase transition, which occurred between 9 and 10 GPa. Full-potential DFT Linearized Augmented Plane Wave (LAPW) calculations were performed in the generalized gradient approximation (GGA) with the Wien2k software package. A 16-atom supercell was constructed, for the composition Fe_7Ni, shown in schematic in **Figure 1**. The antiferromagnetic structure was found to be more stable than the nonmagnetic structure, and HMF as high as 6.6 Tesla were found. Synchrotron Mossbauer spectrometry (SMS) experiments were performed on the sample of $Fe_{92}Ni_8$ at beamline 16 ID-D of HPCAT at the Advanced Photon Source at a pressure of 21 GPa and a temperature of 11 K. SMS detects hyperfine magnetic fields by the evidence of quantum beats, interference patterns of emitted gamma rays in the time domain. No quantum beats were detected in the spectrum emitted from the sample, in clear disagreement with the calculated results. Using the fitting routines in the program CONUSS, theoretical curves based on the calculated HMF were generated, and overlaid

Authors (from left) Michael Hu, Rebecca Stevens, and Alexander Papandrew prepare to lift a dewar of liquid Helium at HP-CAT.

with the data. These curves are shown in **Figure 2**.

There are two probable explanations possible for the disparity between the experimental and the calculated results. An overestimation by 20% of the strength of exchange coupling by the GGA functional results in a large change in the calculated magnetic moment, from 1.077 μ_B/atom to 0.053 μ_B/atom. Alternatively, quantum spin fluctuations thought to be responsible for superconductivity in ε-iron below 2K may be faster than the Mossbauer lifetime, inhibiting detection of a hyperfine field. The hcp lattice is geometrically frustrated with respect to antiferromagnetism, and it is known that fluctuations play an important role in the physics of many frustrated antiferromagnets. Spin fluctuation rates in the GHz range have been identified in these materials and cannot be discounted for the afmII or any other AFM spin structure for ε-Fe.

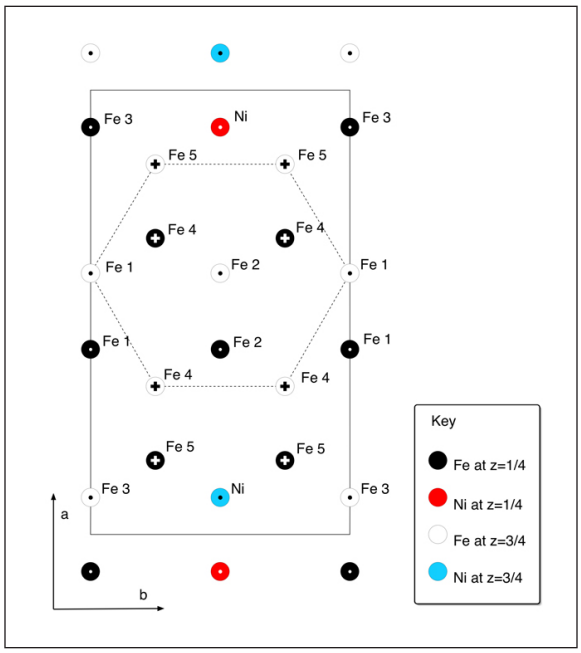

Figure 1. *The Fe_7Ni calculational supercell with the afmII spin structure. Crosses denote a spin orientation pointing into the page, while circles indicate spin pointing out of the page.*

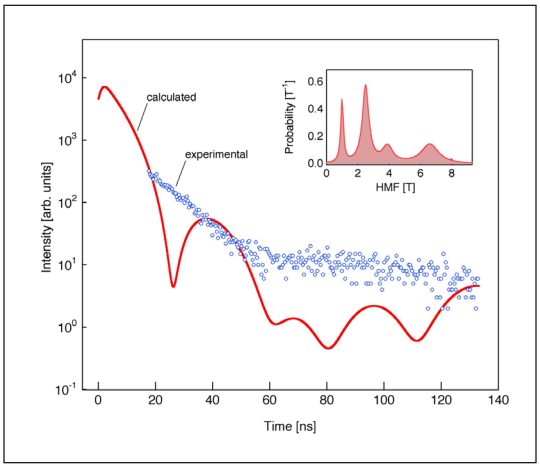

Figure 2. *Experimental data from hcp Fe92Ni8 at 11 K (blue) and a simulated SMS spectrum generated with CONUSS (red) based on DFT calculations of HMF in Fe_7Ni. Inset: The HMF distribution for the simulated spectrum.*

BEAMLINE
X23A2

PUBLICATION
J. Woicik, E. Shirley, C. Hellberg, K. Anderson, S. Sambasivan, D. Fischer, B. Chapman, E. Stern, P. Ryan, et al., "Ferroelectric Distortation in $SrTiO_3$ Thin Films on Si(100) by X-ray Absorption Fine Structure Spectroscopy: Experiment and First-Principles Calculations," *Phys. Rev. B: Condens. Matter*, **75**, 140103, (2007).

FUNDING
U.S. Department of Energy

FOR MORE INFORMATION
Joe Woicik, National Institute of Standards and Technology
woicik@bnl.gov

Ferroelectric Distortion in $SrTiO_3$ Thin Films on Si(001) by X-Ray Absorption Near-Edge Spectra: Experiment and First-Principles Calculations

J.C. Woicik,[1] E.L. Shirley,[1] C.S. Hellberg,[2] K.E. Anderson,[2] S. Sambasivan,[1] D.A. Fischer,[1] B.D. Chapman,[3] E.A. Stern,[4] P. Ryan,[5] D.L. Ederer,[6] and H. Li[7]

[1]National Institute of Standards and Technology; [2]Center for Computational Materials Science, Naval Research Laboratory; [3]National Synchrotron Light Source, Brookhaven National Laboratory; [4]Department of Physics, University of Washington; [5]Ames Laboratory; [6]Department of Physics, Tulane University; [7]Embedded Systems Research, Motorola Labs

Ti K and Ti $L_{2,3}$ x-ray absorption fine-structure near-edge spectra of $SrTiO_3$ thin films grown coherently on Si(001) reveal the presence of a ferroelectric (FE) distortion at room temperature. This unique phase is a direct consequence of the compressive biaxial strain achieved by coherent epitaxial growth.

The cubic perovskite $SrTiO_3$ is a classic example of a system with two coupled instabilities. At room temperature it is cubic, but at 105K it undergoes an antiferrodistortive (AFD) transition involving staggered rotation of the TiO_6 octahedra and a sub-percent *c/a* distortion. The system also verges on but does not become ferroelectric (FE) at low temperature. Early literature suggested that the FE transition is suppressed by zero-point motion, but more recent work has found that the FE distortion is suppressed by the interaction between the FE polarization and the AFD order parameter. The biaxial strain imposed on $SrTiO_3$ thin films by hetero-epitaxial growth has also been shown to have dramatic affect on its structural phase diagram.

Here we report a spectroscopic structural study of strained $SrTiO_3$ grown coherently on Si(001). We report on the splitting, geometric dependence, and chemical hybridization of the Ti 3*d* states by Ti K x-ray absorption near-edge spectra. It is found that strain allows the FE distortion at room temperature, and the local atomic geometry of this distortion is well modeled by first-principles calculations. The evidence presented here for a *c*-axis oriented FE distortion in compressively strained $SrTiO_3$ thin films grown coherently on Si(001) opens the possibility of producing FE devices on Si using appropriate growth conditions and strain engineering.

We studied a 5 monolayer (ML) $SrTiO_3$ thin film, which has an in-plane lattice constant equal to the lattice constant of the Si(001) 1x1 surface-unit cell (3.840 Å) and an out-of-plane lattice constant equal to 4.031±0.01 Å, giving *c/a* =1.050±0.003 as determined by x-ray diffraction. As the lattice constant of cubic $SrTiO_3$ is 3.9051 Å, this film has the largest in-plane compressive strain (1.66 %) reported to date for epitaxial perovskite thin-film growth.

Joe Woicik

Figure 1a shows the ideal cubic perovskite structure of $SrTiO_3$. To understand the observed *c*-axis expansion and possible consequences of strain on the local atomic geometry in the thin film, we performed density-functional theory (DFT) calculations of tetragonally distorted $SrTiO_3$ on Si(001) using the generalized-gradient approximation and projector-augmented wave functions as implemented in VASP.

Figure 1b shows the theoretically optimized structure within the 5 ML $SrTiO_3$ film. Elongation along the *c* axis is evident, as are the FE distortion (displacement of the Ti atoms along *c*) and the AFD rotation of the TiO_6 octahedra. The actual atomic positions are shown. The resulting increase of *c* in the optimized structure gives *c/a* =1.058, in agreement with experiment. This anomalous increase in *c* results from the macroscopic polarization and its coupling to strain that simultaneously allows the coexistence of both the FE and AFD distortions.

Figure 2a shows the Ti K x-ray absorption near-edge spectra for the $SrTiO_3$ thin film. The data are plotted for different sample geometries relative to the incident synchrotron-beam wave-vector **q** and synchrotron-beam polarization-vector **e** and have been normalized to equal edge jump. We also show results for single-crystal cubic $SrTiO_3$. All data were collected at room temperature.

In cubic materials, the intensity of dipole transitions is invariant with respect to **q** and **e**. As shown by their sensitivity to sample geometry, the first two peaks of the bulk $SrTiO_3$ spectra are dipole-forbidden transitions of the Ti 1*s* electrons to the Ti 3*d*-derived t_{2g} (d_{xy}, d_{yz}, and d_{xz}) and e_g ($d_{3z^2-r^2}$ and $d_{x^2-y^2}$) unoccupied molecular orbitals. The energy difference between the two peaks in the bulk $SrTiO_3$ spectra is 2.2 eV, which represents the crystal-field splitting. This splitting results from the different orbital overlap between the Ti *3d* orbitals and the ligand 2*p* orbitals that are strong functions of symmetry. These transitions appear sharp, rather than band-like, because of excitonic interaction between the Ti 1*s* core hole and electron in the Ti 3*d* levels.

The situation is very different for the tetragonally distorted $SrTiO_3$ thin film with c/a=1.050±0.003. The simplest reduction in symmetry of the TiO_6 molecular point group is O_h to D_{4h}, which lifts the triple degeneracy of the t_{2g} levels and the double degeneracy of the e_g levels.

Not only is this reduction to D_{4h} symmetry apparent in the data that show significant shifts and splitting of the $1s \rightarrow t_{2g}$ and $1s \rightarrow e_g$ transitions relative to cubic $SrTiO_3$, but a large increase in the intensity of the $1s \rightarrow 3d_{3z^2-r^2}$ transition is also observed. This enhancement in absorption indicates the further reduction to C_{4v} symmetry that results from the relative displacement of Ti along *z*, making the transition dipole-allowed via $3d_{3z^2-r^2}$-$4p_z$ hybridization. This hybridization is parity-forbidden in both the O_h and D_{4h} point groups that have inversion symmetry, but it is energetically favored in C_{4v} symmetry that breaks inversion; it allows the strong distortion of the Ti atom found in **Figure 1b** and the resulting shorter apical Ti-O bond demonstrated essential for ferroelectricity.

To associate the spectral changes with the local structural distortions found by DFT of **Figure 1**, we calculated Ti K near-edge spectra for cubic $SrTiO_3$ and the 5 ML film. For bulk $SrTiO_3$, we assumed the cubic perovskite structure with a = 3.9051 Å. For the film, we considered a bulk crystal with the theoretically predicted local atomic geometry found in **Figure 1b**.

Figure 2b shows the theoretical Ti 1*s* spectra using a Bethe-Salpeter treatment. All features of the electronic structure and their differences in cubic $SrTiO_3$ vs. the thin film are reproduced in the theoretical calculations: shifting and splitting of the Ti 3*d* levels, the decrease of t_{2g} and e_g in-plane angle-dependence, and enhancement of the $1s \rightarrow 3d_{3z^2-r^2}$ transition. C_{4v} symmetry allows Ti $3d_{yz}$-$4p_y$, $3d_{xz}$-$4p_x$, $3d_{3z^2-r^2}$-$4p_z$, and 4*s*-$4p_z$ hybridization.

Such close agreement between the theoretical spectra and experiment confirm the accuracy of DFT in predicting the local atomic coordinates of this strain-induced FE distortion. This is an important result that substantiates the use of DFT calculations in the strain engineering of FE and other devices, and it should have increasing impact as devices based on thin films of these materials find there way into industrial applications.

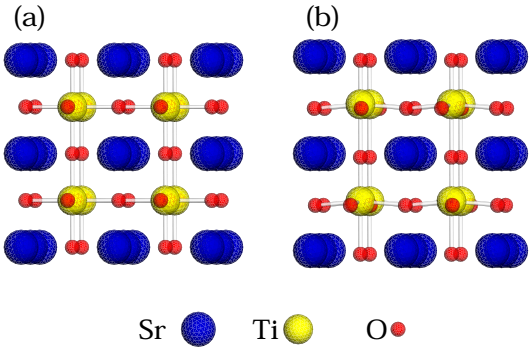

Figure 1: *(a) Structure of cubic $SrTiO_3$. (b) Structure of tetragonally distorted $SrTiO_3$ on Si(001) as calculated by DFT. The structure in (b) reveals both the AFD and FE distortions.*

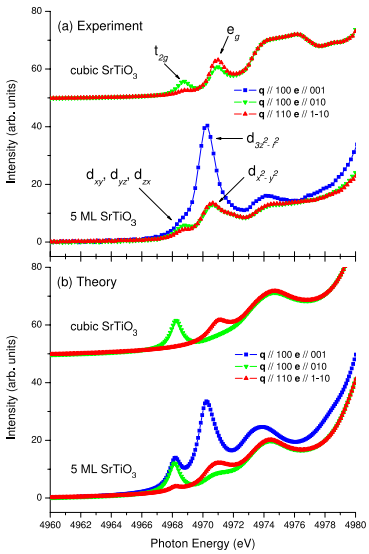

Figure 2: *(a) Ti K spectra for cubic $SrTiO_3$ and a 5 monolayer (ML) $SrTiO_3$ thin film grown coherently on Si(001). (b) Theoretical spectra using the structures from Figure 1 (see text).*

BEAMLINE
U5UA

PUBLICATION
L. Colakerol, T.D. Veal, H.-K. Jeong, L. Plukinski, A. DeMasi, S. Wang, Y. Zhang, L.F.J. Piper, P.H. Jefferson, A. Fedorov, T.C. Chen, T. D. Moustakas, C.F. McConville, and K.E. Smith, "Quantized Electron Accumulation States in Indium Nitride," *Phys. Rev. Lett.,* **97**, 237601 (2006).

FUNDING
National Science Foundation; Army Research Office; Air Force Office of Scientific Research

FOR MORE INFORMATION
Kevin E. Smith, Department of Physics, Boston University
ksmith@bu.edu

Discovery of New Quantum Properties for Electrons Near the Surface of a Semiconductor

L. Colakerol[1], T.D. Veal[2], H.-K. Jeong[1], L. Plucinski[1], A. DeMasi[1], T. Learmonth[1], P.-A. Glans[1], S. Wang[1], Y. Zhang[1], L.F.J. Piper[2], P.H. Jefferson[2], A. Fedorov[3], T.-C. Chen[4], T. D. Moustakas[4], C.F. McConville[2], and K.E. Smith[1]

[1]Department of Physics, Boston University; [2]Department of Physics, University of Warwick, Coventry, UK; [3]Advanced Light Source, Lawrence Berkeley National Laboratory; [4]Department of Electrical and Computer Engineering, Boston University

Electrons near the surface of semiconducting indium nitride have been discovered to exist in "quantum well" states, which are remarkably simple fundamental energy states. It is highly unusual to observe such states in ordinary materials; usually they are observed only in engineered materials or electronic devices. We discovered the quantum well states by irradiation of indium nitride with intense x-rays, which caused the electrons in these states to be ejected from the material into vacuum, where their energy and momentum was measured. This technique, known as photoemission spectroscopy, allowed us to make the first definitive determination of these properties.

We have directly observed a quantized electron accumulation layer near the surface of the narrow gap semiconductor indium nitride (InN) using high-resolution Angle Resolved Photoemission Spectroscopy (ARPES). Electron accumulation is a phenomenon observed in certain semiconductors whereby a higher density of electrons is observed in a layer near the surface of the solid. It is postulated that the surface region in InN has a higher charge density than the bulk due to N vacancies or donor-type surface states. This causes the surface Fermi level to lie in the conduction band. We have discovered that not only are electrons observed far above the conduction band minimum, but these electrons are found to be quantized perpendicular to the surface, i.e. the electrons in the accumulation layer have been determined to reside in quantum well states.

Figure 1 presents an ARPES photocurrent intensity map of emission from the states within 1.5 eV of E_F, recorded with an incident photon energy of 69 eV, from a sample annealed in UHV to 300 °C for 30 minutes. The sample was held at 177 K during measurement. The horizontal axis is the angle of emission, converted to momentum at each point, while the vertical axis is the binding energy; the intensity reflects the photocurrent for any particular binding energy and momentum. The momentum direction is along ΓΣM, in the surface plane. Two well-resolved, nested bands are clearly observed, and these correspond to the quantum well states. ARPES was also used to measure the Fermi surface of the quantum well states, as well as their constant binding energy contours below the Fermi level, E_F. As is clear in **Figure 2**, the Fermi surface was found to consist of concentric, perfectly circular structures associated with each of two quantum well states, but the corresponding energy contours assume a hexagonal symmetry away from E_F. The Fermi level, and the size of the Fermi surface for these quantum well states could be controlled by varying the method of surface preparation.

Authors (from left to right) Yufeng Zhang, Leyla Colakerol, Shancai Wang, Lukasz Plucinski, Tim Learmonth, Sarah Bernardis, and Kevin Smith.

This is the first unambiguous observation that electrons in the InN accumulation layer are quantized, and the first time the Fermi surface associated with such states has been measured. The thin film samples were grown using molecular beam epitaxy at Boston University, with the experiments undertaken on beamline U5UA at the National Synchrotron Light Source and on beamline 12.0.1 at the Advanced Light Source, Lawrence Berkeley National Laboratory.

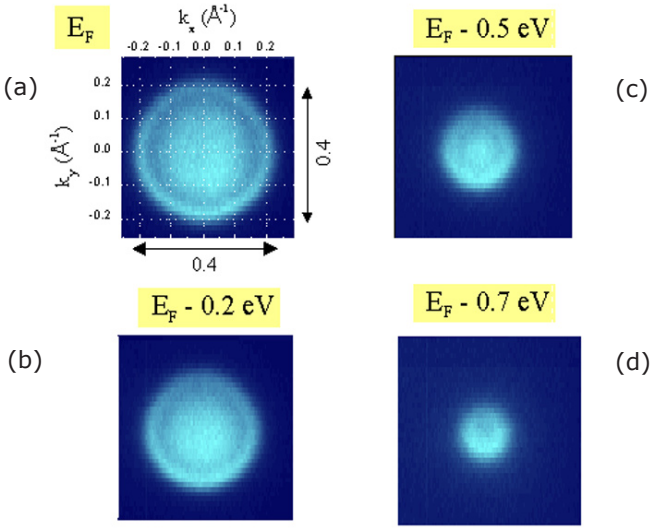

***Figure 1**. ARPES photocurrent intensity map of states within 1.5 eV of E_F. hν = 69 eV, and the sample temperature was 177 K. The sample was annealed to 300 °C in UHV for 30 minutes. The false color intensity reflects the photocurrent, with lighter intensity indicating higher current. The momentum direction is along ΓΣM, in the surface plane.*

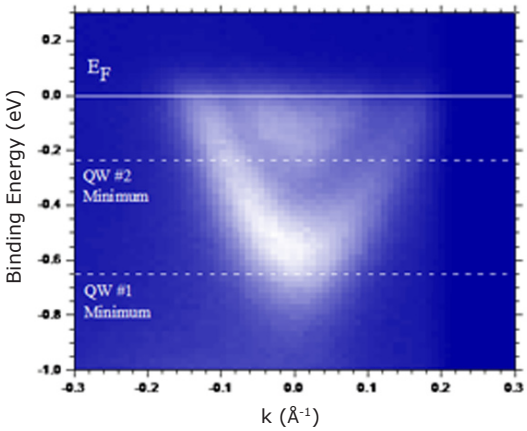

***Figure 2**. Fermi surface and constant binding energy contours. The photocurrent is plotted as k_x and k_y are varied, while the binding energy relative to E_F is kept constant at 0 eV (Fermi surface), 0.2 eV, 0.5 eV and 0.7 eV. hν = 70 eV, and sample temperature was 60 K. The diameter of the outer Fermi surface is 0.4 Å^{-1}.*

BEAMLINE
X21A1

PUBLICATIONS
H. Zhou, Y.P. Wang, L. Zhou, R.L. Headrick, A.S. Özcan, Y.Y. Wang, G. Özaydin, K.F. Ludwig Jr., and D.P. Siddons, "Wavelength Tunability of Ion-Bombardment-Induced Ripples on Sapphire," *Phys. Rev. B*, **75**, 155416 (2007).

FUNDING
National Science Foundation
U.S. Department of Energy

FOR MORE INFORMATION
Hua Zhou or Randall Headrick, Department of Physics, University of Vermont
hzhou@uvm.edu; rheadrick@uvm.edu

Wavelength Tunability of Ion-Bombardment-Induced Ripples on Sapphire

H. Zhou[1], Y. Wang[1], L. Zhou[1], R.L. Headrick[1], A.S. Özcan[2], Y. Wang[2], G. Özaydin[2], K.F. Ludwig, Jr.[2], and D.P. Siddons[3]

[1]Department of Physics, University of Vermont; [2]Department of Physics, Boston University; [3]National Synchrotron Light Source, Brookhaven National Laboratory

A study of ripple formation on sapphire surfaces by low-energy ion bombardment is presented. Surface characterization by in-situ synchrotron grazing incidence small angle x-ray scattering and ex-situ atomic force microscopy is performed. We find that the wavelength can be varied over a remarkably wide range by changing the ion incidence angle. The ion induced viscous flow smoothing mechanism follows the general trends of the ripple wavelength at low temperature and incidence angles larger than 30 . In this model, relaxation is confined to a few-nm thick damaged surface layer. However, strong smoothing is inferred from the observed ripple wavelength near normal incidence.

Energetic particle bombardment on surfaces is known to produce highly correlated arrays of one-dimensional (ripples or wires) and zero-dimensional (dot) structures at the submicron or nanometer-length scale by a self-organization process. This phenomenon has demonstrated the potential to tailor not only surface morphology but also related surface properties, such as optical blue shift due to quantum confinement of dots and magnetic anisotropy induced by rippled structures. We have recently investigated the kinetics of ion-bombardment-induced ripple formation on sapphire surfaces, in particular, smoothing mechanisms in the self-organization process.

Real-time monitoring of sapphire surface evolution upon ion bombardment are carried out in a versatile in-situ surface x-ray facility installed at NSLS beamline X21 end station. A schematic diagram of the experiment is shown in **Figure 1**. A grazing incidence geometry is employed for small angle x-ray scattering (so-called GISAXS), allowing for an enhancement of the near surface scattered intensity with respect to the bulk one. In this work, a detector scan of α_f with a fixed α_i near the critical angle for total external reflection is performed to obtain 2D-GISAXS. The constraint of $\alpha_f \geq 0.3°$ avoids the specular reflected x-rays and maximizes the sensitivity to off-specular diffuse scattering patterns. The 2D scans can be approximately assumed to be Q_z vs. Q_x reciprocal map since Q_y is very small in this case.

Figure 2 shows real-time GISAXS intensities plotted versus parallel component of scattering momentum transfer Q_x at a constant vertical component $Q_z = 0.92$ nm^{-1}. Scans are shown at 10-minute intervals during 45° off-normal incidence 500 eV Ar^+ bombardment. At time t = 0, the initial roughness of the sapphire surface only produces a single peak in the diffuse scattering (circles). Two satellite peaks, resulting from lateral correlated roughness become visible after 10 minutes. The ripple wavelength, $\ell = 2\pi/\Delta Q$, remains almost constant during ion irradiation, but the peak intensity continues to increase as a result of an increase in ripple amplitude. It is also clear that the two satellite peaks develop in an unequal way as irradiation proceeds, which can be attributed to the onset of nonlinear effects of ion beam erosion.

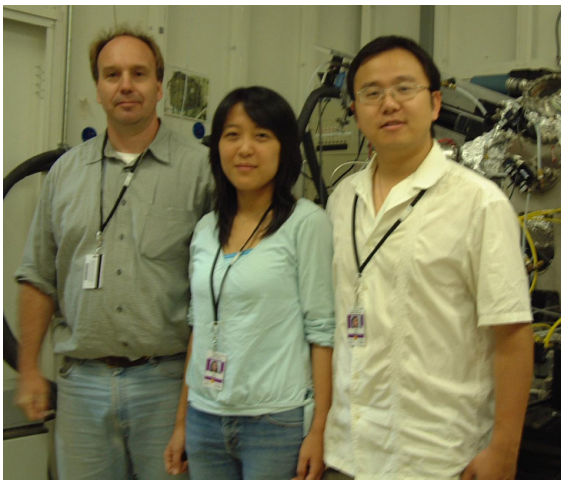

Authors (from left): Randall Headrick, Lan Zhou, and Hua Zhou

Ex-situ AFM images in **Figure 3** display surface morphologies obtained at different angles of incidence for ion sputtered sapphire. Off-normal incidence at 25° produces only micron-scale ripples, which are readily visible in the large-scale image [**Figure 3(b)**]. An ultra-smooth surface is obtained surprisingly at small length scale [**Figure 3(a)**]. In con-

trast, 55° and 65° incidence, shown in **Figure 3(c) and 3(e)**, produce a well-ordered nanorippled surface with the wave vector parallel to the projection of the incoming ion beams along the surface. Grazing ion incidence at 75° switches the orientation of the ripple wave vector perpendicularly. Fully developed ripples are observed, with an unusual rod-like structure, as shown in **Figures 3(g) and 3(h)**.

The ion-induced viscous flow smoothing mechanism can explain the behaviors of observed ripple wavelength at low temperature and middle-range angles of incidence. Strong smoothing near normal incidence is suggested to be the result of ion-bombardment-induced effective downhill currents along the surface.

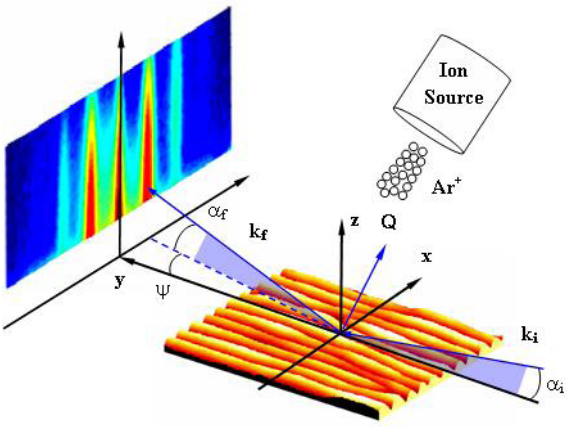

Figure 1. *Schematic diagram of the experiment. z-axis: sample normal. y-axis: the incident x-ray beam. k_i and k_f : the incident and scattered wave vectors, respectively. Glancing angle: $\alpha_i = 0.2°$, $\alpha_f \geq 0.3°$; in-plane (x-y plane) angle: $-1° \leq \psi \leq 1°$. The incoming Ar^+ ions bombard at an incident angle with respect to the surface normal.*

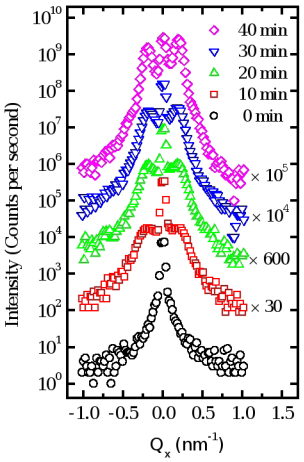

Figure 2. *Time-resolved GISAXS measurements indicate the increase of the lateral correlations on a sapphire surface during ion exposure. The ion exposure was paused during the scans. The curves are shifted for clarity.*

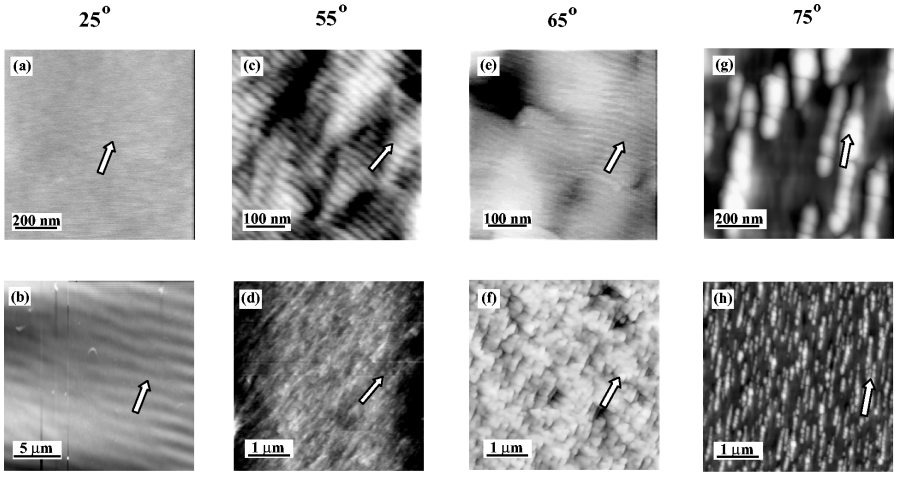

Figure 3. *AFM images of surface morphology at different angles of incidence. Two different image sizes are shown for each angle of incidence. The white arrow indicates the projection of the ion beam direction along the surface. The progression of ripple orientation and wavelength can be seen in this sequence of images.*

BEAMLINE
U5UA

PUBLICATION
H. Lee, I.-G. Baek, and E. Vescovo, "Spin Reorientation Transition in Fe-rich Alloy Films on W(110): The Role of Magnetoelastic Anisotropy and Structural Transition," *Appl. Phys. Lett.*, **89,** 112516 (2006).

FUNDING
Korea Science & Engineering Foundation

FOR MORE INFORMATION
Hangil Lee, Beamline Research Division, Pohang Accelerator Laboratory, Korea
easyscan@postech.ac.kr

Spin Reorientation Transition in Fe-Rich Alloy Films on W(110): The Role of Magnetoelastic Anisotropy and Structural Transition

H. Lee[1], I.-G. Baek[2], and E. Vescovo[2]

[1]Beamline Research Division, Pohang Accelerator Laboratory, Republic of Korea
[2]National Synchrotron Light Source, Brookhaven National Laboratory

Epitaxial Fe-rich alloy films of formula $Fe_{1-x}Ni_x$, $Fe_{1-x}Co_x$, and $Fe_{1-x}V_x$ were grown on a W(110) substrate with a bcc structure without any structural transition at $x < 0.3$. Using chemical pressure (inserting small amounts of Ni, Co, or V into Fe), we controlled the lattice constant of these alloy films and then measured the variation of spin reorientation thickness (t_r) according to the alloy composition. We focused on the roles of lattice constant of the film and the spin reorientation thickness that is closely related to the strain associated with the lattice mismatch between the thin film and the substrate.

The magnetic anisotropy of a film is a key parameter determining its easy and hard magnetization axes, and hence is a very important determinant of the film's magnetic properties such as the spin reorientation transition (SRT), which is decided by competition between volume anisotropy term (K^V) and interface anisotropy contribution term (K^{int}). The simple equation for SRT can be expressed as $K^{eff} = K^V + K^{int}/t$ (when $K^{eff} = 0$, we can determine t_r.)

In magnetic systems with a large lattice mismatch (e.g., Fe on W(110), mismatch ~10.1 %), however, it is necessary to also consider the magnetoelastic anisotropy (K_{me}). If, the K_{me} strongly influences the SRT, we can control the transition by modifying the lattice constant using chemical pressure as we make alloy film with different lattice constants. Also, one of the most interesting issues in thin alloy films is the correlation between the magnetic properties and structural transitions as a function of alloy composition. Here, we investigate that the lattice constant of the film and the spin reorientation thickness (t_r) play key roles in determining the location of the SRT as the alloy composition is varied using SRPES and LEED.

Figure 1 displays LEED images for three alloy systems ($Fe_{1-x}Ni_x$, $Fe_{1-x}Co_x$, and $Fe_{1-x}V_x$) as a function of alloy composition. In the case of the $Fe_{1-x}Ni_x$ alloy film, the distance between the spots in the W(110) and Fe-rich alloy is being decreased with increasing Ni concentration. It indicates that the lattice mismatch diminishes as Ni is added to the Fe; specifically, the mismatch decreases from 7.4 % to 5.5 % when x is increased from 0.1 to 0.2. In terms of the real spacing, the data show that increasing the Ni concentration expands the Fe lattice, thereby increasing the lattice constant. We also used a similar approach to measure the variation of lattice mismatch for $Fe_{1-x}Co_x$, and $Fe_{1-x}V_x$ alloy films. We found that Co and V also expand the Fe lattice, although to a lesser extent than Ni: for the $Fe_{1-x}Co_x$ alloy film, the mismatch decreased from 9.1 % to 6.5 % when x was increased from 0.1 to 0.3; and for the $Fe_{1-x}V_x$ alloy film, the mismatch decreased from 9.6 % to 9.2 % when x was increased from 0.1 to 0.3. Thus, we can precisely control the lattice constant of these alloy films by modifying the alloy composition in the Fe-rich region (bcc structure). Using this *chemical pressure* approach, we monitored the change of t_r as a function of alloy composition using SRPES.

Author Hangil Lee

Figure 2 shows typical results of spin resolved photoemission spectra and their asymmetry value between spin up and spin down spectra, for the change of t_r as monitored with SRPES for three alloy systems at $x = 0.1$. On a W(110) substrate, we grew Fe-rich alloy wedge films with thicknesses spanning a range (in increments of 4 Å) that encompassed the SRT from [1$\bar{1}$0] to [001]. SRP spectra were then recorded as a function of the film thickness along this wedge (z-axis). The SRP spectra and asymmetry results show that the thinner films (bottom spectra) are magnetized along the [$\bar{1}$10] direction, whereas the thicker films (top spectra) are magnetized along the [001] direction.[15] As shown in

these spectra, we can clearly see that t_r varies widely depending on the alloy used, exhibiting values of 326 Å for $Fe_{0.9}Ni_{0.1}$, 102 Å for $Fe_{0.9}Co_{0.1}$, and 76 Å for $Fe_{0.9}V_{0.1}$. These results indicate that insertion of Ni or Co dramatically increases t_r relative to that of the pure Fe film (85 Å),[15] whereas insertion of V decreases it slightly.

In summary, we found that alloys of formula $Fe_{1-x}M_x$ (M = Ni or Co) exhibit a pronounced increase in t_r with increasing x, with the effect being larger in Fe-based alloys. We found that the change of lattice mismatch (strain effect) and structural transition (from *bcc* to *fcc* or *fct*) in these systems play key roles in the observed increase in t_r. Contrary to the behavior of Ni and Co, insertion of increasing amounts of V into the Fe lattice causes t_r to decrease, which we speculate is due to an order-to-disorder transition.

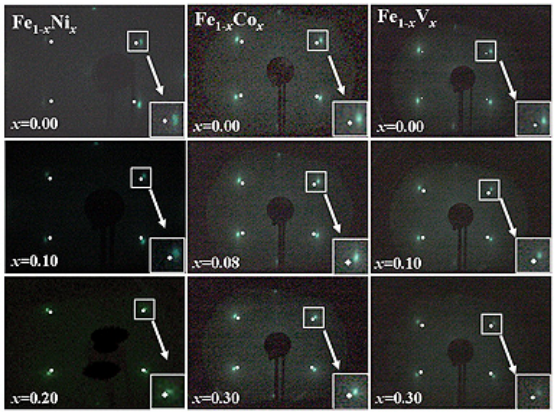

Figure 1. LEED images for three different alloy systems (left panels are $Fe_{1-x}Ni_x$, middle panels are $Fe_{1-x}Co_x$, and right panels are $Fe_{1-x}V_x$) as a function of alloy composition. All LEED images show a bcc structure. The inset image of each LEED data indicates magnified spots between alloy film and W(110) substrate to show clearly the variation of distance between two spots.

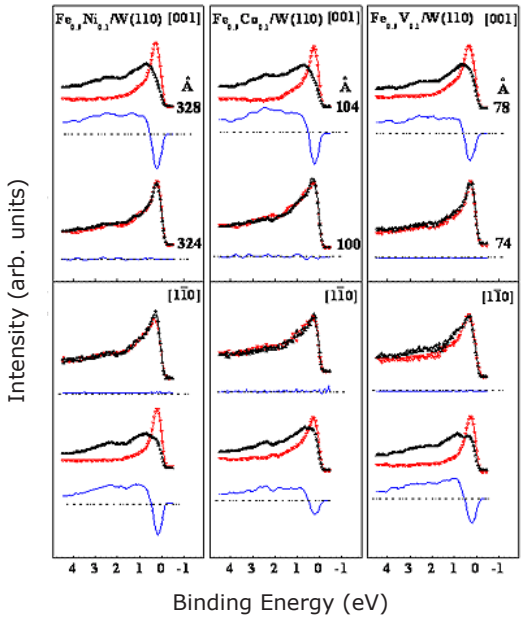

Figure 2. Typical result for magnetic reorientation transition as monitored with spin-resolved photoemission spectra of (a : $Fe_{1-x}Ni_x$), (b: $Fe_{1-x}Co_x$), and (c: $Fe_{1-x}V_x$) at x = 0.1 concentration. The spectra were measured at 40 eV in normal emission. Each filled up-triangles and empty down-triangles represent majority- and minority- spin components, respectively. Below each spin resolved photoemission spectra, asymmetry values $(I_{spin\ up} - I_{spin\ down})/(I_{spin\ up} - I_{spin\ down})$ also are displayed to show a clear change for spin reorientation for three alloy films. $I_{spin\ up}$ and $I_{spin\ down}$ indicate the intensity of majority spin and minority spin, respectively.

BEAMLINE
U4B

PUBLICATION
E. Negusse, A. Lussier, J. Dvorak, Y.U. Idzerda, S.R. Shinde, Y. Nagamine, S. Furukawa, K. Tsunekawa, and D.D. Djayaprawira, "Magnetic Characterization of CoFeB/MgO and CoFe/MgO Interfaces," *Appl. Phys. Letts.*, **90**, 092502 (2007).

FUNDING
Office of Naval Research

FOR MORE INFORMATION
Yves Idzerda, Physics Department, Montana State University
Idzerda@physics.montana.edu

Magnetic Characterization of CoFeB/MgO and CoFe/MgO Interfaces

E. Negusse[1], A. Lussier[1], J. Dvorak[1], Y. U. Idzerda[1], S. R. Shinde[2], Y. Nagamine[2, 3], S. Furukawa[2], K. Tsunekawa[2, 3], and D. D. Djayaprawira[2, 3]

[1]Department of Physics, Montana State University; [2]Canon ANELVA Corporation; [3]Canon ANELVA Corporation, Japan

The use of CoFeB ferromagnetic electrodes in place of CoFe has been shown to significantly increase the tunneling magnetoresistance (TMR) of tunnel junctions (MTJs) where the ferromagnetic electrodes are separated by an MgO tunneling layer. By using soft x-ray scattering techniques, we have shown that the behavior of the interfacial moments in CoFe electrodes is drastically different from the rest of the CoFe film, whereas the magnetic response of CoFeB interfacial moments is coherent with the film's bulk. Our results support the view that the high TMR values observed in MgO-based MTJs with CoFeB electrodes are due to the uniform magnetic response of the entire CoFeB electrode including the MgO interfacial moments.

Considerable efforts have been devoted to improving the fabrication and performance of magnetic tunneling junctions (MTJs) because of their potential applications in next-generation devices such as read-heads for ultra-high density hard disk drives and magnetoresistive random access memories (MRAMs). The extraordinarily high, room-temperature tunneling magnetoresistance (TMR) in MTJs that use an MgO tunneling barrier is due to coherent electron tunneling through this barrier. CoFe alloy, one of the most often used ferromagnetic electrodes in MTJ structures, typically grows in the body-centered cubic (BCC) polycrystalline structure, with little or no structural coherence across the MgO insulating barrier. However, when boron is added to CoFe, the resulting CoFeB is more pliant and the subsequent deposition of MgO results in a more crystalline structure, improving the coherent tunneling and significantly increasing the TMR value from below 100 to well over 200 percent.

To determine precisely how the improved crystalline quality enhances the spin-dependant tunneling across the electrode-MgO interface, we used x-ray absorption spectroscopy (XAS), x-ray magnetic circular dichroism (XMCD), as well as diffuse and specular x-ray resonant magnetic scattering (XRMS) to chemically and magnetically characterize each interface. The measurements were done at the Montana State University X-ray Material Characterization Facility located at NSLS beamline U4B. These nondestructive techniques provide element-specific and interface-sensitive information with magnetic contrast. XRMS is the angle-dependent reflectance of circular polarized soft x-rays, whose energy is tuned to the absorption edge of a magnetic element. It combines the chemical selectivity of x-ray resonant scattering with the magnetic contrast of magnetic circular dichroism.

The samples were prepared using Canon ANELVA C-7100 with the following structure: Si substrate/ Ru(100Å)/electrode/MgO(18Å)/ Ta(40Å), where the electrode is 30Å of either $Co_{70}Fe_{30}$ or $Co_{60}Fe_{20}B_{20}$. All layers were grown using DC magnetron sputtering except the MgO layer, which was grown using RF magnetron sputtering. The samples were cut in half and one half was annealed at 360°C for 2 hours in an 8 kOe magnetic field.

Authors (from left) Alexandre Lussier and Yves Idzerda

The XAS and XMCD spectra showed that both CoFe and CoFeB electrodes were metallic with no significant changes upon annealing. The x-ray scatter-

ing data, done in the configuration shown in **Figure 1** (inset), revealed high-quality interfaces for both electrodes but a distinct difference in the interfacial moments' hysteretic behavior.

As observed from the specular hysteresis loops in **Figure 1**, where the specular scattered intensity of circular polarized x-rays tuned to the Co (or Fe) L-edge is measured as a function of applied field, the improved switching behavior of the CoFe films with the incorporation of boron and subsequent annealing explains the improvement in the TMR behavior but does not fully explain the magnitude of the increase in TMR values. Better insight can be obtained by comparing the hysteretic behavior of the magnetic moments at the electrode-MgO interface by examining the diffuse (nonzero qX) hysteresis behavior of x-ray scattering at the Co L3-edge. The off-specular hysteresis loops in **Figure 2** were normalized so that the intensity at saturation is equal to ±1. They reveal a striking difference in the magnetic behavior of the interfaces. As can be seen in the left panels of **Figure 2**, the specular and off-specular loops for the CoFeB sample are nearly identical, indicating that the interfacial moments reverse in unison with bulk spins.

On the other hand, for the CoFe sample, the off-specular hysteresis loop's shape is highly unusual. The nature of the measurement tells us that during magnetization reversal, the spins responsible for the off-specular scattering in the CoFe film adopt a state of high in-plane magnetic disorder, momentarily giving rise to an increase in diffuse scattering intensity. This behavior is observed in both the as-grown and annealed CoFe films with the annealed films showing nearly an order of magnitude increase in magnetic contribution to the off-specular scattering intensity. Clearly, these moments behave dramatically different from the bulk moments, and degrade coherent tunneling through the MgO barrier leading to lower TMR. Improving the behavior of these moments is vital to the further increase in the TMR values.

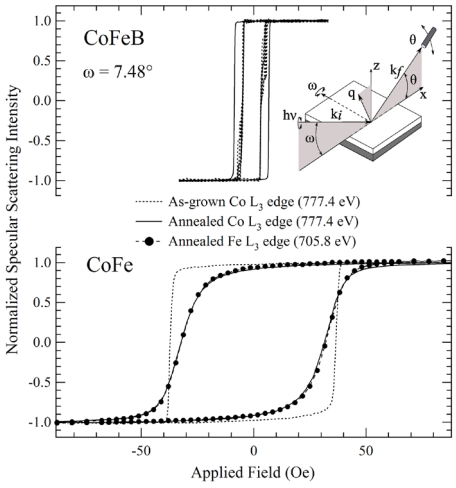

Figure 1. *Specular scattering intensity for circular polarized x-rays at energies resonant with the Co L3-edge as a function of applied field for CoFeB (top panel) and CoFe (bottom panel) films as grown (dashed lines) and annealed (solid lines). Inset: configuration of the scattering setup.*

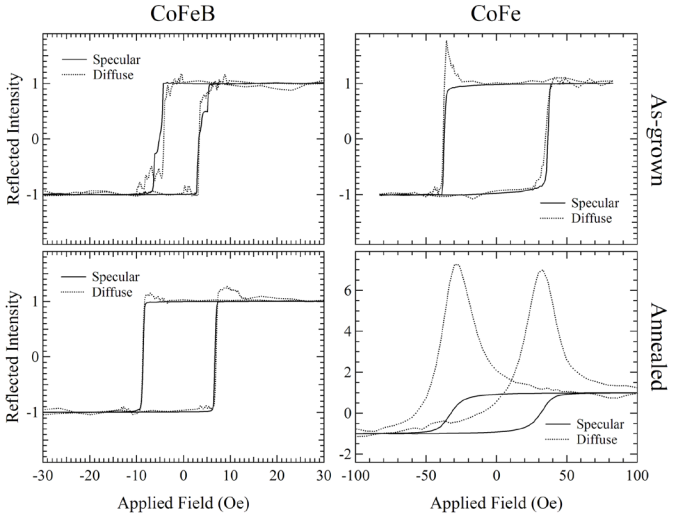

Figure 2. *Specular (solid lines) and off-specular (dashed lines) scattering intensity for circular polarized x-rays at energies resonant with the Co L3-edge as a function of applied field for CoFeB (left panels) and CoFe (right panels) films that are as-grown (top panels) and annealed (bottom panels). Note the different field scales in the right and left panels.*

BEAMLINE
X11A

PUBLICATION
A.I. Frenkel, D.M. Pease, J. Budnick, P. Metcalf, E.A. Stern, P. Shanthakumar, and T. Huang, "Strain-Induced Bond Buckling and its Role in Insulating Properties of Cr-Doped V_2O_3," *Phys. Rev. Letts.*, **97**, 195502 (2006).

FUNDING
U.S. Department of Energy

FOR MORE INFORMATION
Anatoly I. Frenkel, Physics Department, Yeshiva University
Anatoly.Frenkel@yu.edu

Strain Defects and Their Role in Metal-Insulator Transition in Cr-Doped V_2O_3

A.I. Frenkel[1], D.M. Pease[2], J.I. Budnick[2], P. Metcalf[3], E.A. Stern[4], and P. Shanthakumar[2], and T. Huang[2]

[1]Yeshiva University; [2]University of Connecticut; [3]Purdue University; [4]University of Washington

Investigating the origin of the metal-insulating transition (MIT) in $(V_{1-x}Cr_x)_2O_3$ at x ~ 0.01 at room temperature is a challenging task mostly because of too dilute Cr concentration within a concentrated V matrix. Lacking experimental information about Cr and V local environments, the MIT theories, including the most popular Mott-Hubbard model, rely on the average structure of this system ascertained by neutron and x-ray diffraction. We applied a novel x-ray analyzer to discriminate between local environments of V and Cr in the $(V_{1-x}Cr_x)_2O_3$ single crystals by Cr K-edge and V K-edge XAFS at the range of concentrations across the MIT. We observed that a small number of Cr atoms serve as strain defects, generating long-range strain in the lattice and form large regions with long V-V bonds. Our finding supports the hypothesis of Rice and Brinkman, proposed in 1972, that large insulating regions should exist in this system.

The metal-insulator transition (MIT) in Cr-doped V_2O_3, from paramagnetic metal (PM) to paramagnetic insulator (PI) at room temperature (**Figure 1**), has attracted much attention since it was discovered in 1969. Among many puzzles this system offers is the lack of electronic instability at x(Cr) ~0.01 in theoretical calculations of the density of states. Another peculiarity is the structural transformation at the same concentration, ascertained by diffraction, leading to the elongation of the V-V distances both in the ab plane and along the c-axis of the trigonal lattice. The latter observation led many to believe that the MIT in this system is the classical example of Mott-Hubbard type, with V-V distance increase causing delocalization of 3d-electrons and, hence, the MIT. The natures of both the structural and electronic instabilities have long remained unknown.

XAFS analysis of Cr environments in $(V_{1-x}Cr_x)_2O_3$ around the MIT concentration could not been done prior to this work due to the dominating V fluorescence XAFS background. We have recently fabricated a novel fluorescence log-spiral of revolution analyzer where a highly oriented pyrolytic graphite (HOPG) layer was deposited on a Plexiglas support. The LSR parameters were optimised for reflecting Cr K_α photons whose wavelengths satisfied the Bragg condition at the LSR surface. Since the V K_α fluorescence was effectively suppressed, this method allowed us to obtain XAFS measurements at the Cr edge. The use of single crystals prepared by Patti Metcalf at Purdue allowed us to take advantage of linearly polarized (in the plane of synchrotron orbit) x-ray photons to separately probe metal-metal (V-V and V-Cr) bonds in the directions parallel and perpendicular to the trigonal c-axis. Cr K-edge measurements were done at the PNC-CAT (undulator beamline) at the Advanced Photon Source. V K-edge measurements were done at beamline X11A at the NSLS.

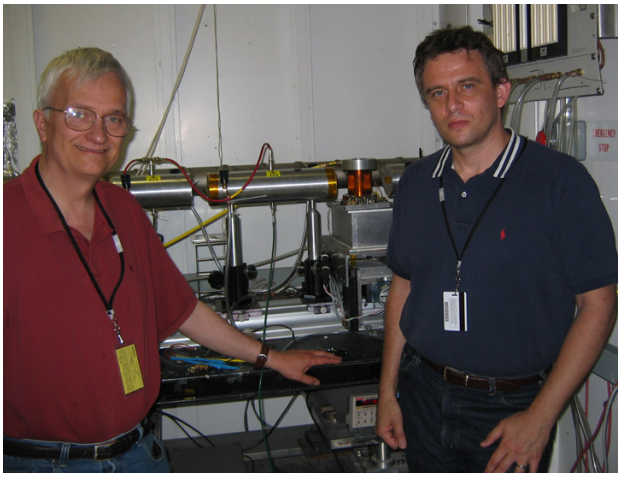

Authors (from left) Douglas Pease and Anatoly Frenkel

Fit results are summarized in **Figure 2**, which demonstrates that the local structure around V and Cr deviates from the average structure measured by XRD. The behavior of the V-V and Cr-V distances in the insulating phase is completely unexpected: V-V distances are found to be longer than Cr-V distances both in the axial and basal plane directions. This difference, in turn,

requires the V-V bond to be longer and V-Cr bond to be shorter than the average metal-metal distance, ascertained by XRD. This trend can be also observed in **Figure 2**.

We explain these new structural details (shortening of Cr-V and elongation of V-V bonds relative to the "average" structure) in terms of local buckling of the crystal structure of $(V_{1-x}Cr_x)_2O_3$ due to the Cr and V size mismatch. Cr atoms play the role of "strain defects" first studied by Eshelby in the 1950s, when he studied inhomogeneities in elastic media. Being the smaller atoms, Cr impurities locally contract the V_2O_3 host lattice. As a result, adjacent V atoms relax toward Cr, and V-V distances involved in such relaxation expand relative to pure V_2O_3 (**Figure 3**). For the low concentration of strain defects (i.e., in our case of $x < 0.1$) the strain fields produce an average volume change with distortions from the average centered at the Cr site and decaying slowly in three dimensions (as $1/r^3$). Our findings allow us to conclude that, due to the long range nature of the strain field, even a small concentration of Cr (ca. 1%) may be sufficient to form large insulating regions (with longer V-V distances and, therefore, lower electron densities than in the PM V_2O_3 host) analogous to those hypothesized by Rice and Brinkman in their Phys. Rev. B article in 1972. As concentration of Cr increases, strain defect begin to interact, triggering structural instability that causes the drastic changes in c/a ratio at x=0.01. Furthermore, such insulating regions, whose size is amplified by long range strain fields, may effectively block conductivity, which suggests a percolative nature of the MIT in $(V_{1-x}Cr_x)_2O_3$.

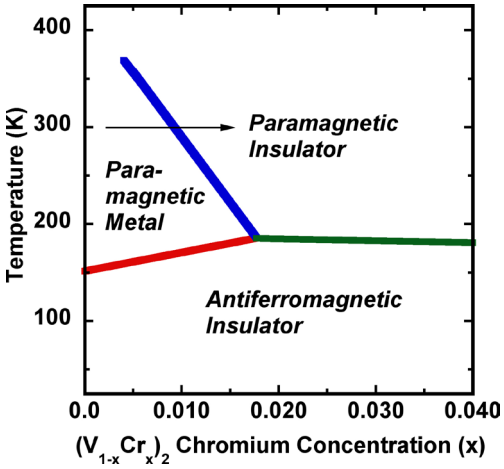

***Figure 1**. The generalized phase diagram for $(V_{1-x}Cr_x)_2O_3$, as a function of temperature and chromium dopant concentration at 1 atm pressure. The samples' compositions (x = 0, 0.00365, 0.0116, 0.0285 and 0.0523) span the diagram across the MIT as shown by the arrow.*

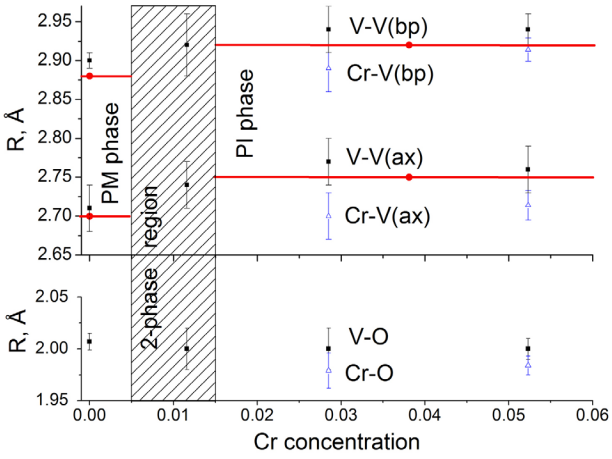

***Figure 2.** First nearest neighbor distances in $(V_{1-x}Cr_x)_2O_3$ measured by EXAFS (symbols) and inferred from x-ray diffraction results for an "average" structure (lines).*

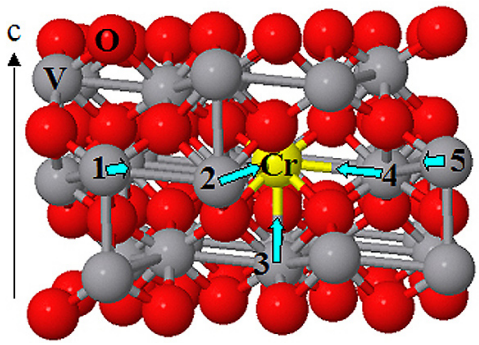

***Figure 3.** Model of local structural distortions around Cr in $(V_{1-x}Cr_x)_2O_3$. Some V atoms that are displaced toward Cr dopants (in the direction of arrows) are denoted by numbers. This model illustrates the dopant-induced strain causing Cr-V (e.g., Cr-V2 and Cr-V3) bonds to contract, and V-V (e.g., V1-V2 and V4-V5) bonds to expand relative to the average M-V distances measured by x-ray diffraction.*

BEAMLINE
U5UA

PUBLICATION
L Plucinski, Y Zhao, and B Sinkovic, "MgO/Fe(100) Interface: A Study of the Electronic Structure," *Phys. Rev. B*, **75,** 214411 (2007).

FUNDING
National Science Foundation
U.S. Department of Energy

FOR MORE INFORMATION
Lukasz Plucinski, Institute of Solid State Research, Jülich Research Center, Germany
l.plucinski@fz-juelich.de

MgO/Fe(100) Interface: A Study of the Electronic Structure

L. Plucinski[1]*, Y. Zhao[1], and B. Sinkovic[1], and E. Vescovo[2]

[1]*Department of Physics, University of Connecticut;* [2]*National Synchrotron Light Source, Brookhaven National Laboratory;* **Current address: Institute of Solid State Research, Jülich Research Center, Germany*

Single crystalline magnetic tunnel junctions based on the Fe/MgO interface have shown significant advantages over earlier structures using Al_2O_3 barrier. However, according to recent theoretical results, their performance might be compromised by the interfacial FeO layer, the existence of which has been reported in experimental x-ray diffraction studies. We have prepared epitaxial MgO/Fe(001) interfaces and performed in-situ spin-polarized angle-resolved photoemission studies on them. The electronic signature of the FeO layer at the interface has not been found, thus existence of such a layer is not an intrinsic property of MgO/Fe interfaces.

In recent years, there have been significant advances in the preparation of single crystalline magnetic tunnel junctions (MTJs) based on MgO(100)-insulating barriers. For example, the theoretically predicted tunneling magnetoresistance (TMR) of several hundred percent in Fe/MgO/Fe(100) has been experimentally verified with values of 180 - 220% for room temperature and even higher values are being reported for various other electrode compositions. However, several theoretical studies have predicted that the oxidation of the MgO/Fe contacts is detrimental to the performance of these MTJs.

Figure 1 shows how annealing of the MgO/Fe(001) interface influences the valence band spectra. In these spectra, Fe 3d-related features appear between 0-4 eV binding energy, while MgO-related features appear for binding energies above 4 eV. Annealing up to 400°C begins to sharpen Fe 3d spectral features in the region close to the Fermi edge and this process is even more visible in the 500°C spectrum, where the sharp spectral feature of the clean Fe surface is nearly fully recovered (right panel in **Figure 1**). This is a clear indication of the absence of the FeO interlayer.

Further poof is obtained by studying core level spectra. The Fe 3p levels exhibit a large magnetic linear dichroism (MLD) in photoemission that can be used to monitor the magnetic state of the Fe layer. Binding energies of Fe 3p and Mg 2p are similar and dichroic spectra in this region are present in **Figure 2**. Comparing spectra from the clean Fe(100) surface (**Figure 2(a)**) to the ones exposed intentionally to 1 Langmuir (L) of molecular oxygen (**Figure 2(b)**), the appearance of a shoulder on the high binding energy side of the spectrum is evident. This shoulder feature, best seen in the right panel of **Figure 2**, is typical of a reaction of oxygen with Fe and indicates the formation of Fe oxide. This shoulder does not display any dichroism, indicating the formation of an unpolarized surface oxide upon even 1 L of oxygen exposure to the clean Fe surface. Most importantly, when MgO is deposited on clean Fe(001) instead (**Figure 2(c)**), there is no indication of this feature in the spectra. On the contrary, the curvature of the relevant part of the core level spectrum remains clearly positive for 1 ML MgO coverage, which is further evidence that no FeO layer is present at the MgO(100)/Fe(100) interface. At higher MgO deposition, the Fe 3p emission becomes rapidly obscured by the much more intense Mg 2p levels (**Figures 2(c)-(d)**) but the Fe dichroism remains strong, which indicates a highly polarized Fe substrate in contact with the MgO overlayer. It is also useful to note that while the Fe dichroism is very strong, no sign of any dichroism is detected under the Mg peak (the full dichroic spectra are shown in the left panel for the case 0.5 ML MgO, as an example). This again

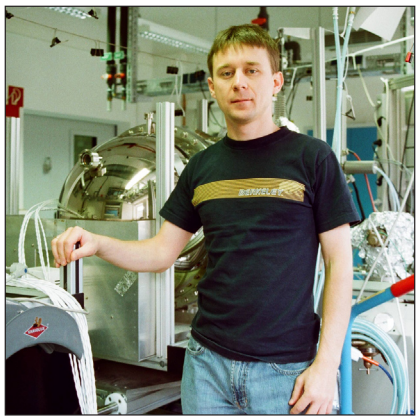

Lukasz Plucinski

tends to confirm the low interaction between Fe and MgO at the interface. For thicker films, where no Fe signal remains, there is no additional Mg 2p line related to metallic Mg. Such a metallic feature would be expected to appear at 2 eV lower binding energy than the main 2p line of MgO, and its complete absence is a confirmation of the good stoichiometry of these films.

In conclusion, by measuring angle- and spin-resolved photoemission spectra we have observed no signs of FeO in our films. Thus, electronically, our samples represent a sharp interface between Fe and MgO, where Fe does not get oxidized during the MgO deposition, i.e. we did not find electronic signature of interfacial FeO layer.

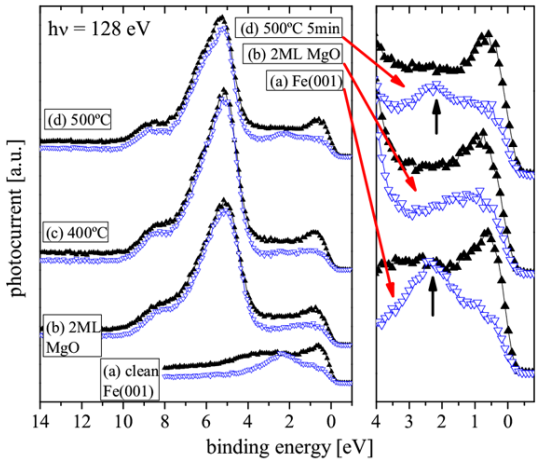

Figure 1. *Spin-polarized photoemission spectra at hv = 128 eV. Left panel: (a) clean Fe(100) (b) 2 ML of MgO/Fe(100) (c) annealed to 400°C for 5 min (d) subsequently annealed to 500°C for 5 min. In right panel, selected spectra are magnified in the region close to the Fermi edge. Spectra are normalized to the majority spin Fe-related part near the Fermi edge. All spectra were taken at room temperature.*

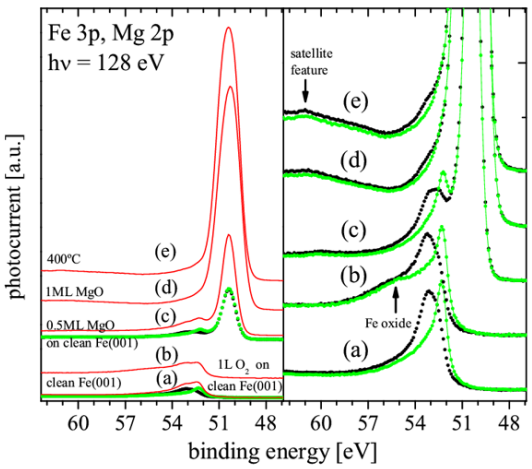

Figure 2. *Fe 3p and Mg 2p core level spin-integrated normal emission energy distribution curves at hv = 128 eV; (a) clean Fe(001), (b) Fe(001)exposed to 1L of molecular oxygen, (c) 0.5ML MgO/Fe(001) deposited on clean Fe(001), (d) 1ML MgO/Fe(001), (e) previous films annealed to 400°C for 5 min. In the left panel, the sum of spectra from the sample magnetized in opposite directions are plotted. The right panel shows the same spectra as on the left but renormalized to magnify the Fe 3p contribution. Opened and closed circles represent spectra from the sample magnetized in opposite directions. All spectra were measured at room temperature.*

BEAMLINE
X13A

PUBLICATION
B.J. Kirby, J.A. Borchers, J.J. Rhyne, K.V. O'Donovan, S.G.E. te Velthuis, S. Roy, C. Sanchez-Hanke, T. Wojtowicz, X. Liu, W.L. Lim, M. Dobrowolska, and J.K. Furdyna, "Magnetic and Chemical Nonuniformity in $Ga_{1-x}Mn_xAs$ Films as Probed by Polarized Neutron and X-Ray Reflectometry," *Phys. Rev. B,* **74**, 245304 (2006).

FUNDING
National Science Foundation; Missouri University Research Reactor Graduate Fellowship; U.S. Department of Energy

FOR MORE INFORMATION
Brian Kirby, Center for Neutron Research, National Institute of Standards and Technology
bkirky@nist.gov

Magnetic and Chemical Non-Uniformity in $Ga_{1-x}Mn_xAs$ as Probed with Neutron and X-Ray Reflectivity

B.J. Kirby[1,2,3], J.A. Borchers[3], J.J. Rhyne[2], K.V. O'Donovan[3,4], S.G.E. te Velthuis[5], S. Roy[6], C. Sanchez-Hanke[7], T. Wojtowicz[8,9], X. Liu[9], W.L. Lim[9], M. Dobrowolska[9], and J.K. Furdyna[9]

[1]Department of Physics and Astronomy, University of Missouri-Columbia; [2]Manuel Lujan Jr. Neutron Scattering Center, Los Alamos National Laboratory; [3]Center for Neutron Research, National Institute of Standards and Technology; [4]Department of Physiology and Biophysics, University of California-Irvine; [5]Materials Science Division, Argonne National Laboratory; [6]Stanford Synchrotron Radiation Laboratory, Stanford Linear Accelerator Center; [7]National Synchrotron Light Source, Brookhaven National Laboratory; [8]Institute of Physics of the Polish Academy of Sciences; [9]Department of Physics, University of Notre Dame

Artificial magnetic semiconductor materials could play a key role in future spin-electronics, or "spintronic" devices. We have used x-ray and polarized neutron reflectometry to study the mechanisms through which post-growth annealing increases the ferromagnetic transition temperature (T_C) of manganese-doped gallium arsenide. Our combined studies suggest that annealing liberates Mn from interstitial sites throughout the $Ga_{1-x}Mn_xAs$ film, and allows them to migrate to the film surface and oxidize – a process that drastically increases T_C, and alters the distribution of the magnetic moment.

Magnetic semiconductors are of great importance to the development of spin-electronics (spintronics) technology, as they can be used to exert magnetic control of electrical current in devices. While suitable ferromagnetic semiconductors cannot be found in nature, non-magnetic semiconductor materials can be made ferromagnetic by replacing a fraction of the atoms in the crystal lattice with magnetic atoms. For example, low-temperature molecular beam epitaxy is used to produce manganese-doped gallium arsenide ($Ga_{1-x}Mn_xAs$, x>10%), in which long-range order among Mn at Ga sites give rise to ferromagnetism. This material is attractive because GaAs is commonly found in modern electronics. However, room temperature ferromagnetism is necessary for practical device applications, but the ferro transition temperature (T_C) of $Ga_{1-x}Mn_xAs$ is only around 70 K. The unstable growth conditions that allow for Mn to enter Ga sites also lead to small concentrations of Mn at interstitial sites in the lattice. These unwanted interstitial Mn impurities are known to oppose ferromagnetic ordering, and are partially responsible for the low T_C of as-grown $Ga_{1-x}Mn_xAs$. However, T_C can be more than doubled by a careful post-growth annealing.

Fully understanding how this annealing process works could lead to room temperature ferromagnetism in $Ga_{1-x}Mn_xAs$. To that aim, we used x-ray and polarized neutron reflectometry (PNR) to study how annealing altered a series of $Ga_{1-x}Mn_xAs$ thin films. Following growth, pieces were cleaved off and annealed – resulting in sets of as-grown/annealed pairs. **Figure 1** shows magnetic and chemical depth profiles for one such set, deduced from PNR measurements taken on the NG-1 Polarized Beam Reflectometer at the NIST Center for Neutron Research. For this set, annealing was found to increase T_C from 60-120 K. The as-grown models are in blue, the annealed are in red. The chemical profiles are shown above the break in the vertical axis, and the magnetic profiles are shown below. Annealing is observed to increase the net magnetization, change the depth distribution of magnetic moment, and add a layer of foreign material to the film surface. Since the chemical profile is flat, the as-

Brian Kirby

grown magnetization gradient cannot be explained by changes in the concentration of Mn at Ga sites, but can be explained by small changes in the depth-dependent concentration of interstitial Mn impurities.

Energy-dependent x-ray reflectometry measurements of these samples were taken on beamline X13A of the National Synchrotron Light Source at Brookhaven National Laboratory, and are shown in **Figure 2**. For the annealed piece, there are pronounced peaks at the oxygen and manganese edges that are absent for the as-grown piece. Since this technique is most sensitive to material near the film surface, these results indicate that the layer of foreign material added by annealing is rich in Mn and O. Non-scattering work by other researchers has shown evidence that the positive effects of annealing are due to removal of interstitial Mn. Combined, our neutron and x-ray results corroborate that idea, suggesting that annealing liberates Mn from interstitial sites throughout the $Ga_{1-x}Mn_xAs$ film, and allows them to migrate to the film surface and oxidize – a process that drastically increases T_C, and alters the distribution of magnetic moment.

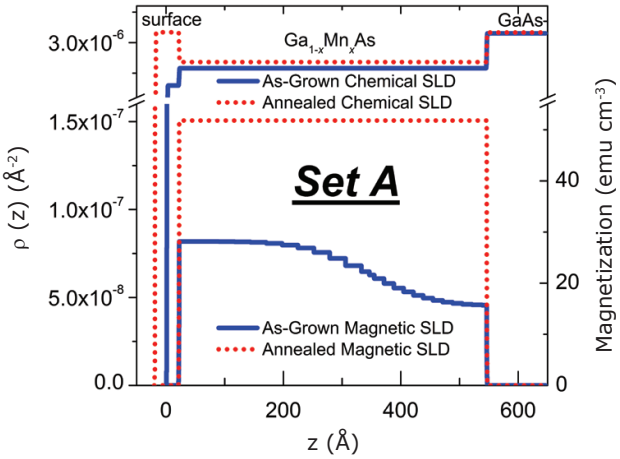

***Figure 1**. Scattering length density models of the as-grown (blue) and annealed (red) films, as deduced from polarized neutron reflectometry. The chemical depth profiles are shown above the break in the vertical axis, the magnetic depth profiles are shown below.*

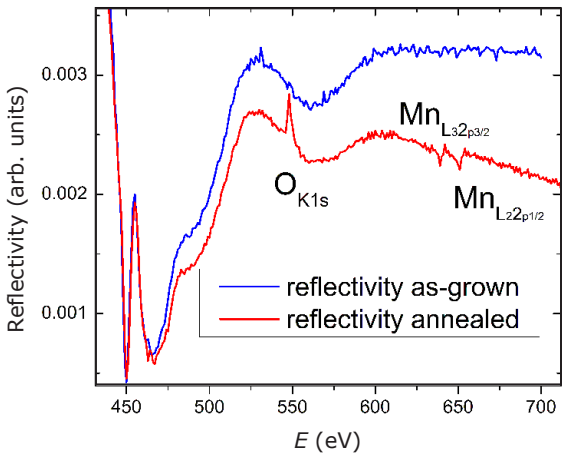

***Figure 2**. X-ray reflectivity for the as-grown (blue) and annealed (red) films taken at NSLS beamline X13A. The annealed film features pronounced oxygen and manganese peaks, while the as-grown film does not.*

BEAMLINE
X22C

PUBLICATION
S. Grenier, V. Kiryukhin, S-W. Cheong, B.G. Kim, J.P. Hill, K.J. Thomas, J.M. Tonnerre, Y. Joly, U. Staub, and V. Scagnoli, "Observation of Orbital Ordering and Jahn-Teller Distortions Supporting the Wigner-Crystal Model in Highly Doped $Bi_{1-x}Ca_xMnO_3$," *Phys. Rev. B*, **75**, 085101 (2007).

FUNDING
U.S. Department of Energy; National Center for Scientific Research (CNRS), France; European Union

FOR MORE INFORMATION
Stephane Grenier, Institut Néel, CNRS Grenoble, France
stephane.grenier@grenoble.cnrs.fr

Revealing Electronic Crystals

S. Grenier[1,2], V. Kiryukhin[3], S-W. Cheong[3], B.G. Kim[3], J.P. Hill[1], K.J. Thomas[1], J.M. Tonnerre[2], Y. Joly[2], U. Staub[4], and V. Scagnoli[4]

[1]Condensed Matter Physics and Materials Science Department, Brookhaven National Laboratory; [2]Institut Néel, Département Matière Condensée, Matériaux et Fonctions, CNRS, France; [3]Department of Physics and Astronomy, Rutgers University; [4]Swiss Light Source, Paul Sherrer Institute, Switzerland

The interactions among valence electrons lie at the heart of much of today's condensed-matter experimental and theoretical research. Most of the key types of interactions can be found in one class of materials – manganites. Moreover, in manganites, these interactions cause the charges and orbitals to " crystallize" – that is to form regular patterns in the solid, allowing crystallographic studies of the electronic structure that results from the interactions. The determination of an electronic crystal is an experimental challenge, however, specifically in cases with a very low density of valence electrons. Using a technique called resonant x-ray diffraction, it was possible, first, to reveal the ordering of the orbitals and, second, to propose a crystallographic structure in which the ordered electrons are "dressed" with a distortion of the surrounding atomic structure.

Determining precisely which electronic orderings take place in 3*d* oxide crystals may help refine some concepts for many interacting electrons. To that aim, manganites provide an ideal test-bed for these ideas. The manganese atom has all of the electronic degrees of freedom: its charge changes with the amount of hole doping and it has a large magnetic moment that can give rise to ferro- or antiferromagnetic ordering. The Mn 3d valence orbital is also a degree of freedom; It is very anisotropic (**Figure 1**), and can align in different directions from site to site, a phenomenon known as orbital ordering. As is the case for magnetic ordering, one may observe ferro or antiferro orbital ordering. Further, because the magnetic structure depends on the relative orientations of the orbitals, manganites show many interrelated charge, orbital, and magnetic orderings. However, typically, orbital ordering concerns one electron out of a hundred in the unit cell, and even lower densities, within larger unit cells, are of great interest in order to study the theoretical models in low-density conditions. Observing such orderings with traditional techniques is extremely challenging.

To study such orbital ordering, the main challenge to overcome is the low sensitivity of conventional x-ray or electron techniques. In fact, the standard crystallographic methods are hard-pressed to refine the positions of all the atoms in the superstructure, much less the direction of the electronic orbitals. However, one may gain a huge increase in sensitivity if x-rays of a very particular energy are used in diffraction experiments – a phenomenon known as "resonant scattering." In resonant scattering, the energy of the incident x-ray is tuned to the energy of the photoelectric transition, so that the photoelectron doesn't leave the crystal but rather "visits" the valence orbitals of the excited Mn atom. If this valence electron has a different orientation from site to site, then one can observe a superstructure reflection, which corresponds to the orbital ordering. This is the "orbital order reflection."

Stephane Grenier

John Hill

Using this technique at NSLS beamline X22C and at the Swiss Light Source SIM beamline, we have determined the orbital ordering in manganites with large unit cells. We measured the orbital order reflections at

the Mn K(L)-edges at X22C (SIM) and retrieved all the information on the electronic structure that is embedded in the dependence of the reflections with the energy of the photoelectric transition, the "spectrum" of the reflection. After numerical and tensorial analyses of the resonant scattering, we found a pattern in which the valence orbitals are antiferro-ordered and as far from each other as possible. Two conflicting models were evaluated, and we could unambiguously determine that one of them, the so-called "Wigner-crystal model" was correct. We also showed that some valence orbitals are accompanied by a typical local distortion of the ligands (the oxygens). This distortion helps to trap the electron, increasing the resistivity. In fact, we also have found that the resonant spectra are extremely sensitive to the displacements of the atoms. This is because the *atomic* structure determines the *electronic* structures, as is well known by users of the EXAFS technique. Finally, we proposed a crystallographic structure that could be used as an initial guess for a conventional crystallographic refinement, with the x-ray resonant spectra providing *non-arbitrary* constraints, in particular, on the space group.

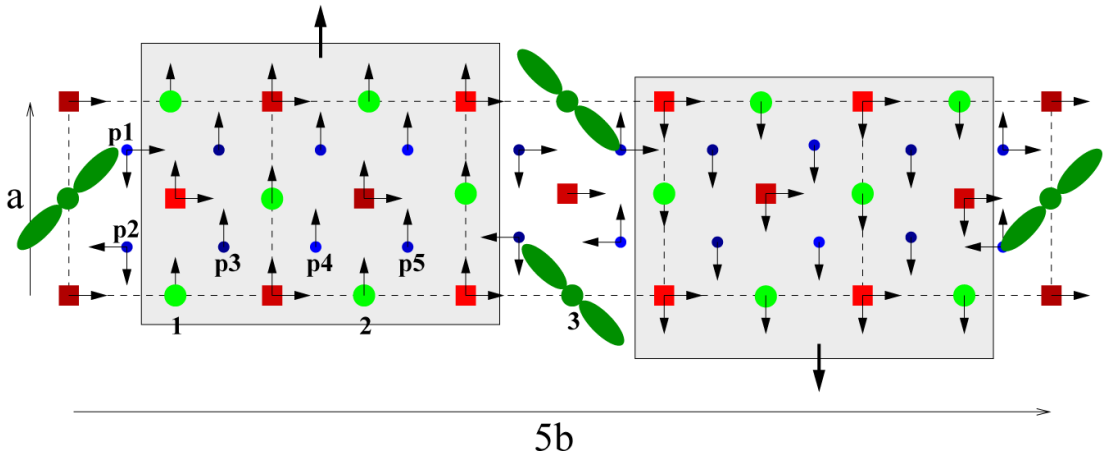

***Figure 1**. Orbital and atomic structures proposed from the study of the resonant x-ray diffraction data. In green, the Mn atoms. For a few of them, an extra valence electron gives an anisotropy, and these exhibit orbital ordering. Other atoms are oxygens and cations (Bi, Ca). Arrows are displacements from a non-ordered structure.*

Investigating Arsenic and Selenium in Fly Ash From Coal Plants

Arsenic and selenium – two of the most volatile and potentially hazardous elements to be released from commercial coal-burning plants – are also found in large quantities in the byproduct of the electricity-producing process. This fine residue, known as fly ash, is produced in large quantities as coal is burned and can either be used in "green" applications such as concrete, or disposed of in landfills and tailings ponds. To learn more about how these potentially toxic elements are released when submerged in water, a team of researchers used the NSLS to determine the basic characteristics of selenium and arsenic in fly ash samples collected from several plants in the United States and Canada.

"A huge amount of electricity is generated from coal, which means huge amounts of coal combustion and waste materials," said University of Kentucky researcher Frank Huggins. "About 10-20 percent of the mass of the coal comes out as fly ash, and there are some uses for the material, but most of it ends up in ponds. Ultimately, we want to find out how much of these trace elements leach out and how far they go."

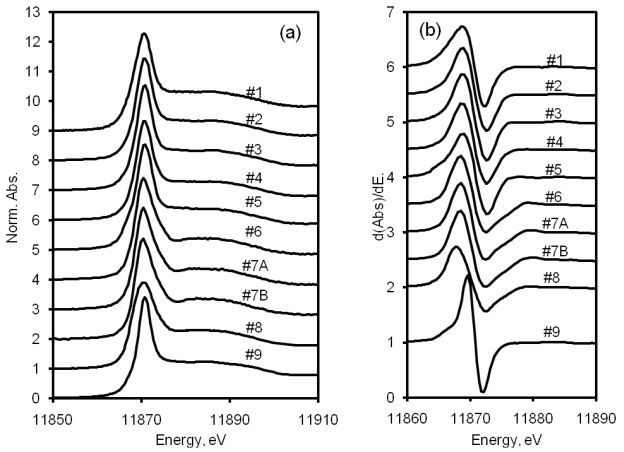

Arsenic XANES (a) and derivative XANES (b) spectra for 10 fly-ash samples from full-scale pulverized coal combustion plants in North America. Samples 1 - 5 and 9 were derived from plants burning eastern U.S. bituminous coals that are rich in sulfur and iron. In contrast, samples 6 – 8 were derived from plants burning western subbituminous coals that are low in sulfur and rich in calcium. The spectra show that the arsenic is present in the fly-ash principally as arsenate species. Also, the XANES spectra for arsenic, as well as for selenium (not shown), exhibit systematic differences that reflect the type of coal. The spectrum for sample #9 was collected using a Si(220) monochromator crystal set and exhibits noticeably better resolution than the other nine spectra, which were collected using a Si(111) monochromator crystal set.

Authors (from left, top) Paul Chu, Gerald Huffman, (center) Frank Huggins, Ken Ladwig, and (bottom) Constance Senior

Using x-ray adsorption fine structure spectroscopy (XAFS) at NSLS beamline X18B and at the Stanford Synchrotron Radiation Laboratory, Huggins and his team of researchers determined the oxidation states and speciation of selenium and arsenic in samples from coal-fired utility plants burning a range of coals. These factors primarily determine the elements' toxicity and how easily they escape from the material, Huggins said.

"Generally, the higher the oxidation state of the element, the more soluble it is, and the easier it gets into the water supplies," he said.

After examining 10 samples of two types of coal – eastern United States bituminous (Fe-rich) and western North American sub-bituminous (Ca-rich) – the researchers discovered that selenium is found predominantly as Se(IV) and arsenic is found as As(V). Similar spectral details were observed for both arsenic and selenium in the two different types of fly ash, suggesting that a major

component (possibly Fe in bituminous coal or Ca in sub-bituminous coal) controls the capture of these elements by fly ash during combustion. The results were published in the May 1, 2007 issue of *Environmental Science & Technology*.

The XAFS work performed by the research team, which also includes Constance Senior (Reaction Engineering International, Salt Lake City, Utah), Gerald Huffman (University of Kentucky), and Paul Chu and Ken Ladwig (Electric Power Research Institute, Palo Alta, CA), is meant to complement another study on arsenic and selenium fly ash leachability.

This work was funded by Electric Power Research Institute.

For more information, see: F. Huggins, C. Senior, P. Chu, K. Ladwig, and G. Huffman, "Selenium and Arsenic Speciation in Fly Ash from Full-Scale Coal-Burning Utility Plants," Environ. Sci. Tech., ***41****, 3284-3289 (2007).*

— Kendra Snyder

Featured Highlight

NSLS Scientists Reach for the Stars(dust)

A research project at the NSLS has turned to dust – star dust, that is. After months of studying particles collected from a comet passing inside Jupiter's orbit, a group of NSLS users and scientists has finished its preliminary examination on the dust, revealing details that might help explain the beginning of the solar system.

As part of an international team of more than 175 members, NSLS users and scientists used x-ray, infrared, and ultraviolet light to study the chemical composition and properties of the extremely small dust particles, most less than 15 micrometers in diameter. The diameter of a human hair, in comparison, is about 50 micrometers. Locked within the particles, which were collected from the comet Wild 2 by the NASA Stardust spacecraft, is unique chemical and physical information that provides a record of the formation of the planets and the materials from which they were made.

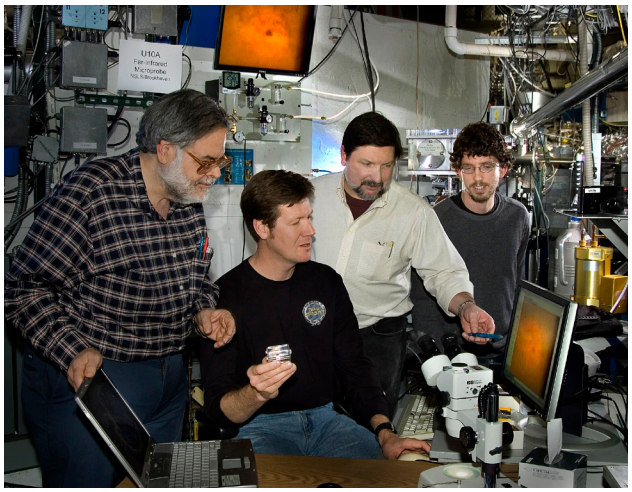

(From left) George Flynn (SUNY Plattsburgh), Lindsay Keller (NASA), Larry Carr (NSLS), and Randy Smith (NSLS) examine samples from the Stardust mission at beamline U10A.

Working with about a picogram of dust, one trillionth of a gram, the scientists studied the elemental composition, organic materials, and mineralogy and petrology of the particles at four NSLS beamlines – X26A, X1A1, U10A, and U10B. Their findings, combined with those from other synchrotrons and institutions, were published in three of the seven Stardust papers published in the December 15, 2006 issue of the journal *Science*.

The first samples from Stardust arrived at the NSLS in February 2006, suspended within "aerogel," a silicon-based, sponge-like material used to capture the particles in space. Once the particles were extracted from the gel, a powerful x-ray imaging device was used to collect detailed images of some of the smallest particles as well as to determine their elemental makeup. In particular, the scientists looked for the element carbon, which can indicate that the particles contain organic compounds — compounds that may have formed at the birth of our solar system.

Infrared light was used to identify specific minerals within the particles, as well as identify any organic compounds that were detected. Unlike x-ray methods, the information collected using these infrared techniques can be compared with the astronomical observations of distant interstellar dust clouds, including those involved with the formation of planetary systems like ours.

One of the main findings of the study is that the materials from which our solar system formed must have undergone a considerable amount of mixing while the sun and planets were forming.

"The common perception is that comets come from these really cold regions of the solar system with lots of ice," said University of Chicago geochemist Tony Lanzirotti, who worked on multiple aspects of the analysis. "But we found minerals like olivine, high-temperature minerals that on Earth are formed in magma. It really says a lot about the violent early history of the solar system, where you have high-temperature phases being mixed with cold regions of outer space in a very rapid manner."

The comet dust was found to contain a wide variety of minerals, as well as organic materials. Some of these minerals and organics look similar to those seen in primitive types of meteorites, but both the minerals and the organics show the presence of some new materials not previously seen in meteorites.

One of the biggest challenges was accounting for the deterioration of the dust particles as they crash-landed into the aerogel at 14,000 miles per hour.

"They're looking at all the little components that were left behind after the particle hit the aerogel, and in the end, they want to get the composition of the original particle," said NSLS physicist Larry Carr.

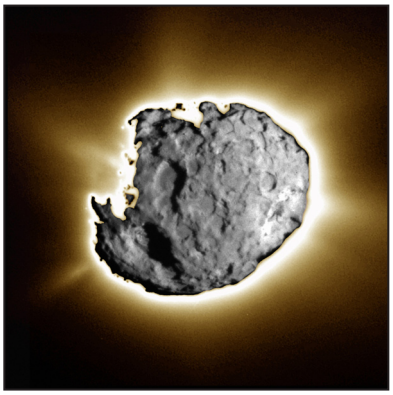

Composite Stardust image of Comet Wild 2 (Photo courtesy of NASA)

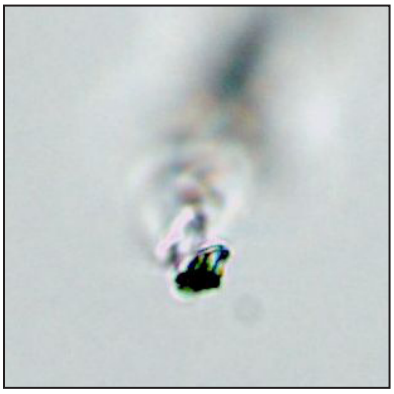

Stardust particle (crystalline object with dark borders), embedded in the aerogel collector. (Photo courtesy of NASA)

"The particles are a composite with parts getting ripped off and left behind in the form of a debris trail. It would be like finding a dead body in the woods, along with footprints, pieces of cloth, and hair, and trying to figure out who the victim was."

Now that the preliminary examination is completed, the samples will be made available to the general scientific community for more detailed study, possibly at the NSLS, where this small amount of dust has caused a great deal of attention.

*For more information see: L.P. Keller, S. Bajt, G.A. Baratta, J. Borg, J.P. Bradley, D.E. Brownlee, H. Busemann, J.R. Brucato, M. Burchell, and L. Colangeli, et al., "Infrared Spectroscopy of Comet 81P/Wild 2 Samples Returned by Stardust," Science, **314**, 1728 - 1731 (2006).*

Featured Highlight

Diamonds from Outer Space: Geologists Discover Origin of Earth's Mysterious Black Diamonds

The research in this news release, which was distributed by the National Science Foundation, was performed at Brookhaven's National Synchrotron Light Source. At beamline U2B, which is operated by the Case Center for Synchrotron Biosciences, of Case Western Reserve University, scientists used infrared light to analyze the diamonds' elemental makeup.

If indeed "a diamond is forever," the most primitive origins of Earth's so-called black diamonds were in deep, universal time, geologists have discovered. Black diamonds came from none other than interstellar space.

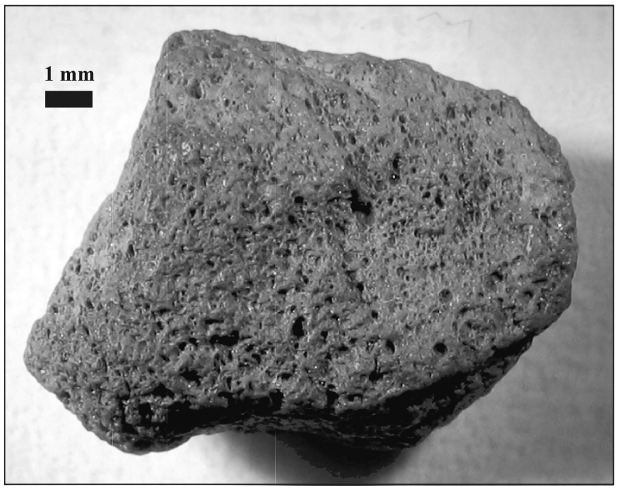

Black, or carbonado, diamonds, came from outer space, geologists have discovered. (Courtesy Steve Haggerty)

In a paper published on December 20, 2006, in the journal *Astrophysical Journal Letters*, scientists Jozsef Garai and Stephen Haggerty of Florida International University, along with Case Western Reserve University researchers Sandeep Rekhi and Mark Chance, claim an extraterrestrial origin for the unique black diamonds, also called carbonado diamonds.

Infrared synchrotron radiation at Beamline U2B was used to discover the diamonds' source.

"Trace elements critical to an 'ET' origin are nitrogen and hydrogen," said Haggerty. The presence of hydrogen in the carbonado diamonds indicates an origin in a hydrogen-rich interstellar space, he and colleagues believe.

The term carbonado was coined by the Portuguese in Brazil in the mid-18th century; it's derived from its visual similarity to porous charcoal. Black diamonds are found only in Brazil and the Central African Republic.

"Conventional diamonds are mined from explosive volcanic rocks [kimberlites] that transport them from depths in excess of 100 kilometers to the Earth's surface in a very short amount of time," said Sonia Esperanca, program director in the National Science Foundation's Division of Earth Sciences, which funded the research. "This process preserves the unique crystal structure that makes diamonds the hardest natural material known."

From Australia to Siberia, from China to India, the geological settings of conventional diamonds are virtually identical, said Haggerty. None of them are compatible with the formation of black diamonds.

Approximately 600 tons of conventional diamonds have been mined, traded, polished and adorned since 1900. "But not a single black/carbonado diamond has been discovered in the world's mining fields," Haggerty said.

The new data support earlier research by Haggerty showing that carbonado diamonds formed in stellar supernovae explosions. Black diamonds were once the size of asteroids, a kilometer or more in diameter when they first landed on Earth.

*For more information, see: J. Garai, S.E. Haggerty, S. Rekhi, and M. Chance, "Infrared Absorption Investigations Confirm the Extraterrestrial Origin of Carbonado Diamonds," Astrophys. J., **653**, L153-L156, (2006).*

—Cheryl Dybas, NSF

BEAMLINE
X17C

PUBLICATION
B. Chen, L. Gao, K.-i. Funakoshi, and J. Li, "Thermal Expansion of Iron-rich Alloys and Implications for the Earth's Core," *PNAS,* **104**, 9162-9167 (2007).

FUNDING
National Science Foundation

FOR MORE INFORMATION
Bin Chen, Department of Geology, University of Illinois at Urbana-Champaign
binchen2@uiuc.edu

Thermal Expansion of Iron-Rich Alloys and Implications for the Earth's Core

B. Chen[1], L. Gao[1], K.-i. Funakoshi[2], and J. Li[1]

[1]Department of Geology, University of Illinois at Urbana-Champaign; [2]Japan Synchrotron Radiation Research Institute, SPring-8, Japan

Understanding the thermal–chemical state of the Earth's core requires knowledge of the thermal expansion of iron-rich alloys at megabar pressures and high temperatures. We have determined the unit-cell parameters and thermal expansivity of the iron–sulfur compound Fe_3S by using synchrotron x-ray diffraction techniques and externally heated diamond–anvil cells at pressures up to 42.5 GPa and temperatures up to 900 K. Our data at 42.5 GPa and 900 K suggest that 2.1 atom % sulfur produces 1% density deficit in iron. We have also carried out energy-dispersive x-ray diffraction measurements on pure iron and Fe-Si alloy samples that were placed symmetrically in the same multi-anvil cell assemblies, using the SPring-8 synchrotron facility in Japan. Based on direct comparison of unit cell volumes under presumably identical pressures and temperatures, our data suggest that at most 3.2 atom % silicon is needed to produce 1% density deficit with respect to pure iron.

The Earth's core makes up nearly one-third of the planet's mass. Its composition, properties, and dynamics are fundamental issues in the study of the Earth's interior. Deeply buried in the center of the planet, the core has kept its chemical composition a long-standing mystery. Cosmochemical studies of meteorites and geochemical analysis of samples from shallower portions of the Earth suggest that the core is made of iron(Fe)-rich alloys containing Ni and one or more lighter elements such as S, Si, C, O, or H. A critical test for any candidate core composition model is that it must be able to reproduce the physical properties of the core. On the basis of observing seismic rays penetrating the deep interior of the Earth and the orbital dynamics of the Earth as a planet in the solar system, models have been constructed to describe the physical state, density profile, and velocity profiles of the Earth's interior. One of the most widely used models is the Preliminary Reference Earth Model (PREM).

To perform the test of consistency between a composition model and the PREM model, we must know the thermal state of the core and the equation-of-state (EOS) of various Fe-rich alloys at the pressure and temperature conditions of the core. A survey of literature revealed a significant lack of thermal expansion data on Fe-rich alloys under static high pressure. In this study, we have determined thermal expansion of Fe_3S, Fe, and Fe–Si alloys using in-situ synchrotron techniques.

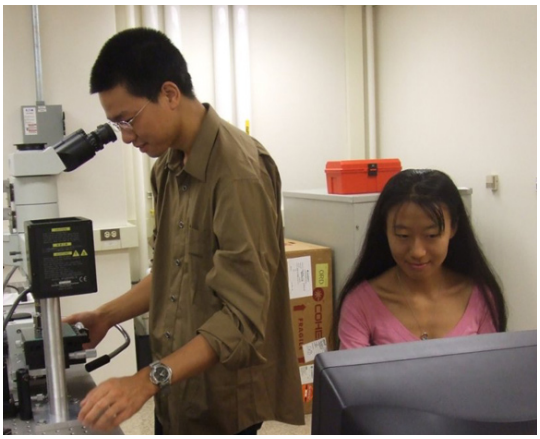

Authors (from left) Bin Chen and Lili Gao

Figure 1, left shows an externally heated diamond–anvil cell used to generate high pressures and temperatures. X-ray diffraction data were collected in several compression-heating-quench cycles covering pressures up to 42.5 GPa at 300, 600, and 900 K (**Figure 1b**). The experimental data are fitted by a modified Birch-Murnaghan equation of state for diverse temperatures such that thermoelastic parameters of can be completely derived (**Figure 1, right**). Given 6-10% deficit between the outer core and solid Fe, and 1-3% deficit between the inner core and solid Fe, we estimated 12.5-20.7 atom % S in the outer core and 2.2-6.2 atom % S in the inner core based on our data at the highest experiment pressure and temperature.

We have carried out energy-dispersive x-ray diffraction measurements on pure iron and Fe-Si alloy samples, using the SPring-8 synchrotron facility in Japan. **Figure 2** shows the scanning electron microscope images of the

quenched samples that were placed symmetrically in the same multi-anvil cell assemblies. Our pressure-temperature range covers 21–27 GPa and 300 to 2000 K. Within this pressure range and between 300 and 1,273 K, Fe adopts the hexagonal close-packed (hcp) structure. The starting Fe-Si alloy breaks down to a mixture of a Si-enriched body-centered cubic phase and a Si-depleted hcp phase, which have been proposed to be the stable forms of Fe–Si alloys in the Earth's inner core. We have derived lattice parameters of pure iron and the Fe-Si alloys. Given 6–10% deficit between the outer core and solid Fe, and 1–3% deficit between the inner core and solid Fe, based on a direct comparison of unit cell volumes under presumably identical pressures and temperatures, our experimental data suggest an upper limit of 19–32 atom % Si in the outer core, and an upper limit of 3.2–9.6 atom % Si in the inner core.

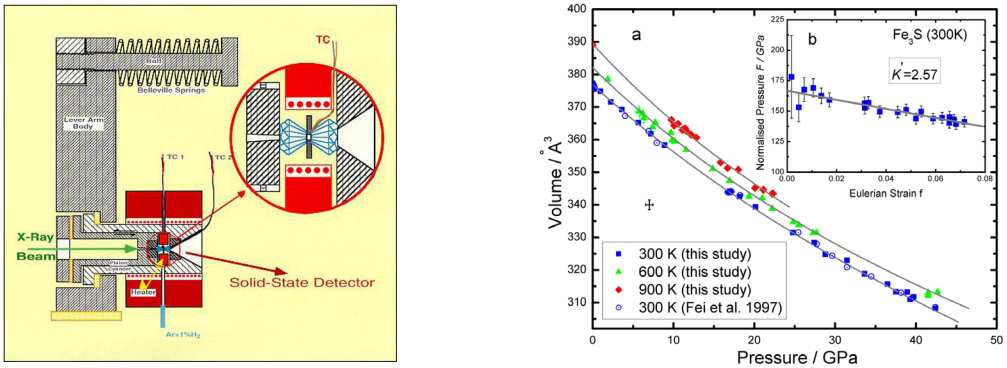

***Figure 1**. Left: Experimental setups of an externally heated diamond–anvil cell using in-situ x-ray techniques. Right: Isothermal compression data of Fe_3S at 300, 600, and 900 K. (a) The three lines are the third-order Birch-Murnaghan EOS fits to the compression data. (b) f-F plot of the compression data at 300 K. The data can be fitted by an inclined straight line, suggesting that the compression of Fe_3S can be adequately described by a third-order Birch-Murnaghan EOS.*

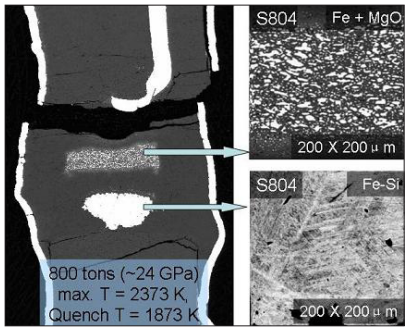

***Figure 2**. Scanning Electron Microscopy (SEM) image of the cross-section of the quenched sample from the experimental run S804*

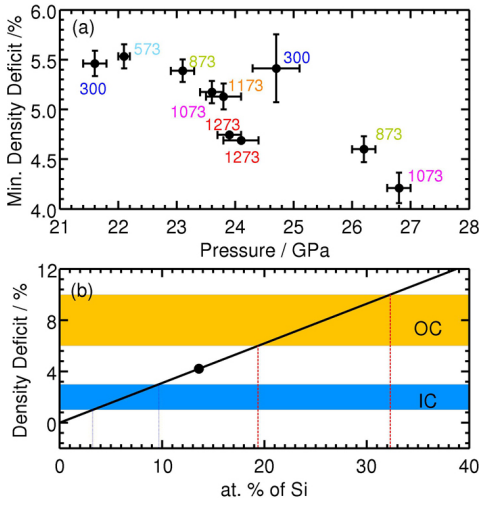

***Figure 3**. (a) Minimum density deficit between hcp–$Fe_{0.864}Si_{0.136}$ and hcp–Fe under different experimental conditions. Density deficit is defined as the absolute density difference divided by the density of pure iron. Numbers next to symbols denote temperatures in Kelvin. (b) Density deficit versus maximum Si content in Fe–Si alloy with hcp structure. Yellow and blue regions labeled "OC" and "IC" indicate density deficit of the outer and inner core compared with pure Fe, respectively. The filled circle represents the minimum density deficit produced by 13.6 atom % Si, based on data in (a). The solid line represents a linear relationship between density deficit and Si content; dotted and dashed lines enclose the ranges of maximum Si content in the IC and OC, respectively.*

BEAMLINES
X26A, X11A

PUBLICATION
V.G. Alexandratos, E.J. Elzinga, and R.J. Reeder, "Arsenate Uptake by Calcite: Macroscopic and Spectroscopic Characterization of Adsorption and Incorporation Mechanisms," *Geochim. Cosmochim. Acta,* **71** (17), 4172-4187 (2007).

FUNDING
National Science Foundation

FOR MORE INFORMATION
Vasso G. Alexandratos
Department of Earth Sciences - Geochemistry, Utrecht University, The Netherlands
vasso@geo.uu.nl

A Macroscopic and Spectroscopic Study on Arsenate Uptake by Calcite

V.G. Alexandratos[1,3], E.J. Elzinga[2,3] and R.J. Reeder[3]

[1]Faculty of Geosciences – Geochemistry, Utrecht University, Utrecht, The Netherlands; [2] Department of Environmental Sciences, ETH Zurich, Switzerland; [3] Department of Geosciences, Center for Environmental Molecular Science, Stony Brook University

Combined use of EXAFS and μ-XRF provide insight to surface-site selective uptake of arsenate (AsO_4^{3-}) by calcite. Results show strong sorption interactions between As(V) and the calcite surface. For calcite single crystals grown in the presence of As(V), μ-XRF-documented preferential incorporation of arsenate at one set of growth steps relative to the other during growth. As K-edge EXAFS results on As(V) sorbed to calcite confirm formation of a tetrahedral inner-sphere complex with two Ca shells, consistent with a strongly bound species and providing constraints to modes of surface coordination.

Uptake mechanisms on mineral surfaces, including adsorption, coprecipitation and precipitation, influence the mobility and bioavailability of chemical species in natural systems. Arsenic (As) is a toxic metalloid that can be introduced into the environment through natural sources (e.g. mineral weathering, geothermal processes) and/or through anthropogenic activities (e.g. industry, mining, agriculture). In oxidized environments As is mainly present in the 5+ oxidation state as arsenate (AsO_4^{3-}). Much research has focused on the uptake of As species by various common minerals, and specifically for As(V) it has been shown that formation of a strongly bound surface adsorption complex is a dominant mechanism over a range of environmentally relevant conditions (e.g. pH, ionic strength, reaction time). Calcite, an abundant and reactive mineral component of soil and aquifer systems, has been shown to be an effective sorbent of metals and oxyanions. Prior studies have shown that metal uptake is subject to strong surface site preferences that may control the partitioning of dissolved species between the aqueous and solid phase.

In combination with batch uptake experiments on calcite we investigated AsO_4^{3-} uptake mechanisms, including adsorption and coprecipitation, using As K-edge x-ray absorption spectroscopy and micro-x-ray fluorescence mapping (μ-XRF). Specifically, we used μ-XRF to determine selective partitioning of As(V) to different sites that were spatially segregated on the $(10\bar{1}4)$ surface of calcite single crystals grown from an As(V)-containing solution. Extended x-ray absorption fine structure (EXAFS) spectroscopy was then used to gain insight to the local coordination of As(V) sorbed on the calcite surface.

The critical factor that makes it possible to identify surface site preferences for As(V) uptake is that spiral growth on the calcite $(10\bar{1}4)$ surface results in the formation of two characteristic non-equivalent pairs of vicinal surfaces, denoted as "+" and "–," that differ in the structure of surface sites in their growth steps (**Figure 1c**). The μ-XRF elemental mapping of these surfaces from crystals grown in As(V)-containing solutions shows significant enrichment of As in the "–" vicinal surfaces relative to "+" vicinals (**Figure 1a**), indicating that incorporation of



Authors (from left) Vasso Alexandratos, Evert Elzinga, and Richard J. Reeder

As(V) is influenced by the structural characteristics of advancing growth steps. We hypothesize that the site-selective incorporation results from differences in As(V) binding at the surface steps. This is supported by differential interference contrast microscopy (**Figure 1b**), which reveals microtopographic differences as a result of differential incorporation.

To gain insight to As(V) sorption mechanisms at the calcite surface, we collected As K-edge EXAFS data on As(V)-sorbed calcite in wet paste samples. Fitting results confirm formation of a tetrahedral inner-sphere surface complex with two separate Ca shells at distances of 3.4 and 3.6 Å. Although it is not possible to distinguish differences in sorption geometry between different sites in the batch sorption samples used for EXAFS, we can constrain aspects of the dominant binding mode. The presence of the two Ca shells indicates either the co-existence of more than one As(V) surface complex or a dominant coordination as a bidentate complex in steps or a tridentate complex in kink sites (**Figure 2 a-d**). These conclusions are consistent with the strong binding that has been observed in batch studies, and provides information for further modeling of surface interactions of As species with calcite surfaces.

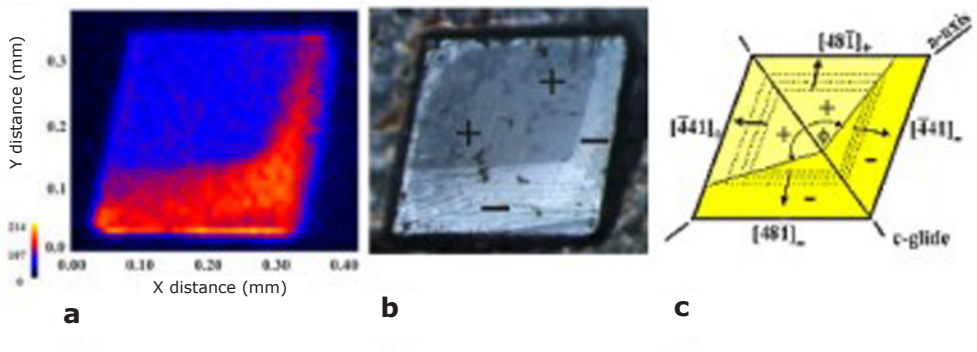

Figure 1. *(a) Micro-XRF element map showing As Kα counts on the (10$\bar{1}$4) growth surface of a calcite single crystal. Highest As Kα counts are shown in yellow and red; lowest counts in blue and black. (b) Corresponding DIC image of the growth surface showing the two pairs of vicinal surfaces denoted as + and –. (c) Schematic illustration showing the orientation of growth steps.*

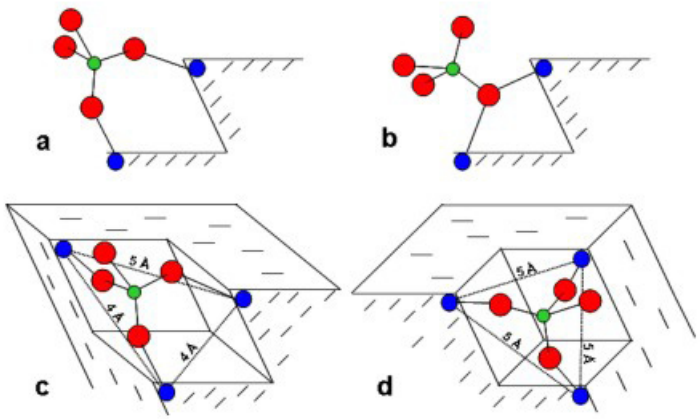

Figure 2. *Schematic illustrations showing possible surface complexes for As(V) adsorption at step and kink sites on the calcite (10$\bar{1}$4) surface: (a) bidentate corner-sharing, (b) monodentate (bridging) corner-sharing, (c) tridentate corner-sharing at kink site in "–" step, (d) tridentate corner-sharing at kink site within "+" step.*

Featured Highlight

Setting the Stage to Find Drugs Against SARS

UPTON, NY - Scientists at the U.S. Department of Energy's Brookhaven National Laboratory have set the stage for the rapid identification of compounds to fight against severe acquired respiratory syndrome (SARS), the atypical pneumonia responsible for about 800 deaths worldwide since first recognized in late 2002. Researchers from Brookhaven's biology department and the National Synchrotron Light Source (NSLS) characterized a component of the virus that will be the target of new anti-SARS virus drugs. The results were published online by *Biochemistry* on November 17, 2006.

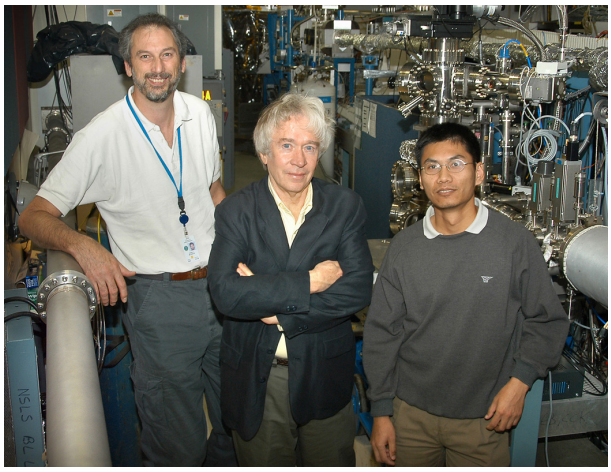

(From left) William McGrath, Wally Mangel, and Lin Yang

"Although vaccines against viruses are very effective, vaccines for viruses that mutate rapidly – such as the viruses that cause SARS, AIDS, and bird flu – are much more difficult to obtain," said Brookhaven biologist Walter Mangel, the lead author of the paper. "Even if a vaccine is available, antiviral agents are important in stopping the spread of highly infectious viruses. If antiviral agents for SARS had been available, they could have been used to contain the outbreak to the initial site of the infection."

The researchers studied the SARS main proteinase, an enzyme used by the virus during infection to cut newly made viral proteins into gene-sized, functioning pieces. If the proteinase is prevented from working, the virus infection is aborted. Previous studies have revealed that the proteinase is inactive when in the form of single molecules. But once two of those molecules bind together to make what is called a dimer, the enzyme becomes active and is able to play its role in SARS virus reproduction. The challenge for researchers, and the focus of the Brookhaven study, was to determine the concentration at which individual proteinase molecules form active dimers. Knowing this concentration, for which estimates at other laboratories have varied greatly, would allow researchers to search for anti-SARS drugs more efficiently by ensuring that the proteinase used in tests is initially in its active form.

Using three different scientific techniques, including x-ray scattering at the NSLS, the Brookhaven researchers obtained almost identical values for this concentration. Now that this crucial value has been narrowed down to a precise range, researchers can focus on finding compounds that bind to the active form of the enzyme.

"Targets for antiviral drugs must be carefully chosen such that binding to it prevents the virus from reproducing," Mangel said. "Viral proteinases are excellent targets for antiviral drugs. One reason so many people are surviving the AIDS epidemic is the effectiveness of drugs targeted to the proteinase of human immunodeficiency virus (HIV)."

One way to obtain compounds that bind to a proteinase is via high-throughput screening. Chemical libraries containing tens of thousands of small compounds are available that can be searched for effective drugs against various diseases. Small amounts of a target, e.g., an active viral proteinase, are placed in tiny wells in a plate, and a different compound from the library is added to each well.

To determine whether a compound binds to and inhibits the proteinase, an additional molecule is added that changes color in the presence of an active proteinase. Wells that don't show a color change therefore contain compounds that inhibit the proteinase, and could be effective antiviral agents. Earlier this year, Mangel's research group published a procedure on the synthesis of a new compound that changes color in the presence of the active form of the SARS main proteinase.

However, for this screening process to work, the SARS proteinase inserted into the wells has to be active to begin with. Knowing the concentration range for dimer formation will therefore help researchers in their search for a compound to stop the virus. "Now that the stage is set, high-throughput screening can begin," Mangel said. "Hopefully, it will yield an antiviral agent that can be stockpiled before a virulent strain of the virus reappears."

This research was supported by the Office of Basic Energy Sciences within the U.S. Department of Energy and the National Institutes of Health.

For more information, see: V. Graziano, W.J. McGrath, and L. Yang, "SARS CoV Main Proteinase: The Monomer-Dimer Equilibrium Dissociation Constant," Biochemistry, ***45****, 14632-14641 (2006).*

— Kendra Snyder

Potent Peptides Inhibit HIV Entry Into Cells

Protein analysis at Brookhaven's light source helps researchers in design of new AIDS drugs

Based in part on protein structures determined at the NSLS, scientists at the University of Utah have developed new peptides that appear to be significantly more effective at blocking HIV's entry into cells than other drugs in their class. In a paper published online by the *Proceedings of the National Academy of Sciences* the week of October 8, 2007, the researchers say these peptides are sufficiently potent to begin pre-clinical studies as a new class of agents for the prevention and treatment of HIV/AIDS.

Annie Heroux

"Our 'D-peptides' offer several potential therapeutic advantages over existing peptide entry inhibitors, which are costly, require high dose injections, and suffer from the emergence of drug-resistance," said University of Utah biochemist Michael S. Kay, lead author on the paper. "In contrast, our D-peptides resist degradation, so they have the potential to be administered by mouth and last longer in the bloodstream. Since these inhibitors have a unique inhibitory mechanism, they should work well in combination with existing HIV inhibitors."

The researchers were particularly interested in developing drugs to bind to an essential "pocket" structure found in all HIV strains that was previously identified as a promising drug target using structures determined at Brookhaven's NSLS. Numerous previous attempts to target this pocket failed to produce potent and non-toxic pocket-specific entry inhibitors. In the current work, the researchers used a high-throughput technique to screen a "library" containing hundreds of millions of peptides to identify the rare peptides that would bind to the pocket structure and inhibit HIV entry.

After identifying the most promising candidate peptides, the researchers analyzed the structure of these peptides bound to the target protein using x-ray crystallography at NSLS beamline X29. In this technique, researchers analyze how an extremely bright beam of x-rays, available only at synchrotron sources, bounces off and is refracted by the sample to determine the positions of individual atoms.

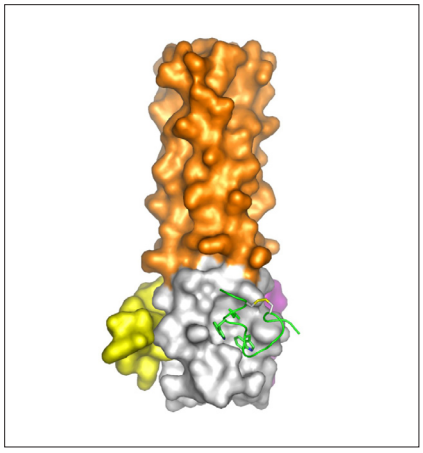

Structure of D-peptide inhibitors (green, yellow, and purple) bound to an HIV protein mimic in three "pockets" that are essential to the virus ability to enter cells. Blocking the pockets thwarts entry and reduces infectivity.

"These structures reveal details of how the peptides bind and guide the development of future inhibitors," said paper co-author Annie Heroux, a biologist and crystallography specialist at Brookhaven Lab.

This structure-assisted design led to the discovery of D-peptides with up to a 40,000-fold improved antiviral potency over previously reported D-peptides. The structures also suggest ways to engineer the peptides to reduce the chance of drug resistance.

This research was funded by the National Institutes of Health, the University of Utah Technology Commercialization Project, and by the American Cancer Society. Operational funding for the NSLS is provided by the Office of Basic Energy Sciences within the U.S. Department of Energy's Office of Science and by the National Institutes of Health.

For more information, see: B.D. Welch, A.P. VanDemark, A. Heroux, C.P. Hill, and M.S. Kay, "Potent D-Peptide Inhibitors of HIV-1 Entry," PNAS, ***104****, 16828-16833 (2007).*

—Karen McNulty Walsh

NSLS Research Links Zinc to Age-Related Macular Degeneration

At the NSLS, a team of researchers has discovered that the mineral zinc may play a role in the development of age-related macular degeneration (AMD), the leading cause of blindness among elderly people in the developed world.

One of the hallmarks of AMD is the accumulation of protein and lipid rich deposits in a part of the eye called Bruch's membrane. The underlying mechanisms of this deposit formation are not clear, but because zinc is known to contribute to deposit formation in neurodegenerative diseases such as Alzheimer's disease, the researchers decided to explore the role zinc might play in AMD. Using x-ray fluorescence mapping at beamlines X26A and X27A, the group measured the concentration of zinc in nine post-mortem human eyes with AMD. The results, published in the April 2007 edition of Experimental Eye Research, show unexpectedly high levels of zinc in the deposits, indicating that the mineral might indeed contribute to the development and progression of AMD.

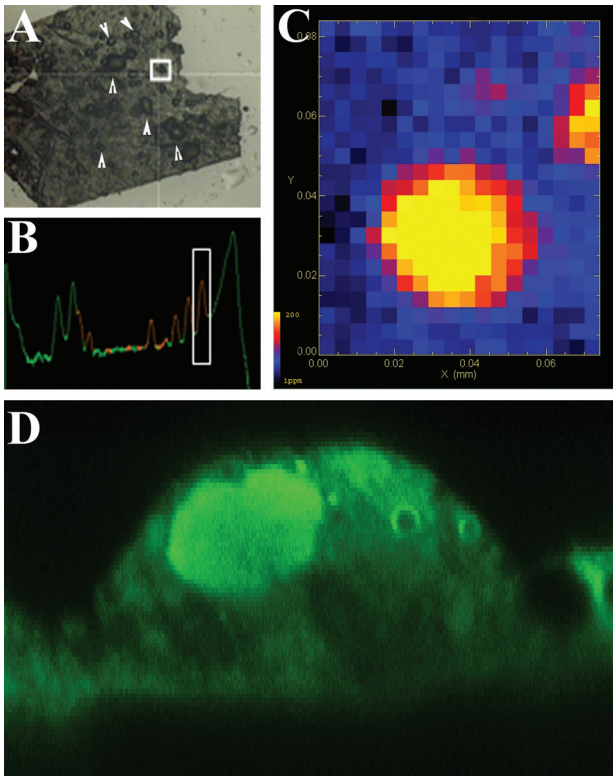

Zinc depositions in age-related macular degeneration. A) Sub-RPE deposits, which are early hallmarks of AMD, can be visualized on bright field images of whole mounted donor tissues. This image depicts the appearance of deposits under a laboratory microscope. While small deposits are invisible during an eye examination, large (>125 um) drusen are indicative of AMD. B) Following calibration using external standards, the zinc concentration of individual deposits (one highlighted by the white box on Fig. A) were determined from the μSXRF spectrum. C) Results from μSXRF are shown on a 2-dimensional false color image. Each pixel on this image represents a 4 X 4 μm area of the tissue. D) Optical cross section of a druse labeled by the zinc-specific fluorescent sensor ZP1 showed heterogeneous zinc distribution, suggesting the presence of "hotspots" for zinc deposition that could represent the seeding points for drusen formation and might be relevant in the development and progression of AMD.

Led by Imre Lengyel, of University College of London, the research team included Jane Flinn, David Linkous, and Katherine Cano, all of George Mason University; Tunde Peto from Moorfields Eye Hospital, London; Alan Bird, University College of London; Antonio Lanzirotti, University of Chicago; Christopher Frederickson, NeuroBioTex, Inc.; and Frederik van Kuijk, University of Texas Medical Branch.

This research was supported by the U.S. Department of Energy, the Hungarian National Science Fund (OTKA), Moorfields Eye Hospital Special Trustees, Fight for Sight, and Wilkins AMD fund.

To read the BBC News article about the research, go to: *http://news.bbc.co.uk/2/hi/health/6457427.stm*

For more information, see: I. Lengyel, J.M. Flinn, T. Peto, D.H. Linkous, K. Cano, A.C. Bird, A. Lanzirotti, C.J. Frederickson and F.J.G.M. van Kuijk "High Concentration of Zinc in Sub-Retinal Pigment Epithelial Deposits," Experimental Eye Research, ***84****, 772-780 (2007).*

— Kendra Snyder

BEAMLINE
U10B

PUBLICATION
L.M. Miller, W. Little, A. Schirmer, B. Busa, S. Judex. "Accretion of Bone Quantity and Quality in the Developing Mouse Skeleton," *J Bone Miner Res.* **22(7)**: 1037-45 (2007).

FUNDING
NASA
Whitaker Foundation
SUNY-BNL Seed Grant
U.S. Department of Energy

FOR MORE INFORMATION
Lisa M. Miller, National Synchrotron Light Source, Brookhaven National Laboratory
lmiller@bnl.gov

Accretion of Bone Quantity and Quality in the Developing Mouse Skeleton

L.M. Miller,[1] W. Little,[2] A. Schirmer,[1] F. Sheik,[2] B. Busa,[2] and S. Judex[2]

[1]National Synchrotron Light Source, Brookhaven National Laboratory; [2]Department of Biomedical Engineering, Stony Brook University

In this work, synchrotron infrared microspectroscopy was used to image the chemical composition of young mouse bone and these results were directly correlated with nanomechanical testing and x-ray micro-computed tomography (micro-CT) of the same sample. We found that bone mineral formation proceeded very rapidly in mice by one day of age, where the degree of mineralization, the tissue mineral density, and the mineral crystallinity reached 36%, 51%, and 87% of the adult values, respectively. However, even though significant mineralization had occurred, the elastic modulus of one-day-old bone was only 14% of its adult value, indicating that the intrinsic stiffening of the bone lags considerably behind the initial mineral formation.

Bone mineral density (BMD) measurements are the most common way to assess osteoporosis fracture susceptibility in the clinical setting. However, it has become increasingly clear that there is a substantial overlap in the BMD of normal individuals and patients who sustain fractures. These findings suggest that the quality of bone, in addition to bone quantity, is important for defining fracture risk. An important contributor to bone quality is the chemical makeup of bone. It is well established that the chemical composition and mechanical properties of bone change with age. However, the interdependence between bone's specific chemical makeup (e.g. mineral content, composition, and crystallinity; collagen content, structure, and cross-linking) and its corresponding mechanical properties (e.g. strength, toughness, stiffness) is still poorly understood. In this work, we evaluated the chemical, structural, and mechanical properties of the mouse tibia during the first 40 days of life using synchrotron IR microspectroscopy, microCT, and nanoindentation, respectively. All techniques were performed on identical samples so that direct correlations could be made. The focus of this investigation was at the microscopic level, where we tested the hypothesis that specific compositional properties of bone determine the stiffness of the tissue.

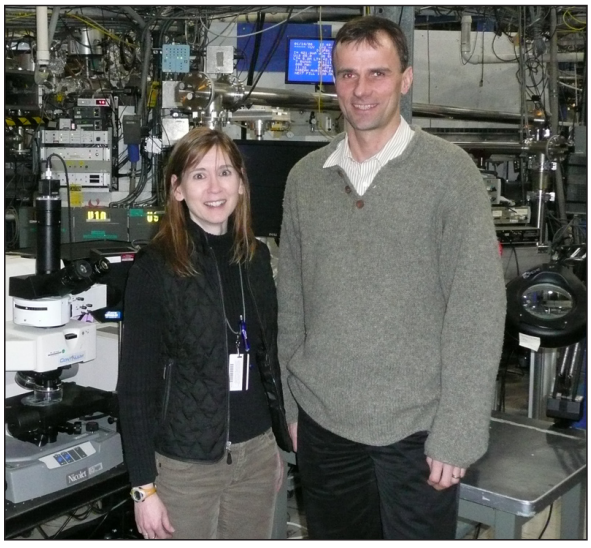

Authors (from left) Lisa Miller and Stefan Judex

Results showed that there was considerable bone quantity and density present in the mouse tibia at birth. At 1 day of age, the degree of mineralization (phosphate/protein ratio), the density of mineralized bone (TMD), and mineral crystallinity had reached 36%, 51%, and 87% of the adult values, respectively (**Figure 1**). Spatially, the variability in mineralization across the mid-tibia was very high for the early time points and declined over time (**Figure 2**). In contrast to the notable changes in mineralization, carbonate substitution into the mineral lattice (carbonate/phosphate ratio) and collagen cross-linking did not show any significant changes over this time period.

Despite the fast accretion of bone quantity during early development, the process of bone stiffening lagged behind. The elastic modulus of 1-day-old bone was only 14% of the adult value and increased to

89% after 40d. Between samples of different time points, significant positive correlations were observed between the elastic modulus and TMD (R^2=0.84), phosphate/protein ratio (R^2=0.59), and crystallinity (R^2=0.23), whereas collagen cross-linking showed a small but significant negative correlation (R^2=0.15).

This initial lag in elastic modulus may be associated with the specific locations of the mineral crystals within the collagen fibrils. Electron micrographs have shown that, in early mineralization, the overall accumulation of mineral mass is predominant in the collagen "hole zones" compared to "overlap zones," where 64% of the crystals were located in the collagen hole zones. Since the elastic modulus of the mouse bone remained low until the tissue mineral density reached ~65% of its adult value, it is possible that mineral accumulation in the hole zones has little effect on bone's intrinsic stiffness. However, once the mineral content increased to where the overlap zones become mineralized, the elastic modulus increased rapidly as well.

In summary, these results indicate that specific chemical and structural properties modulate bone's stiffness during early growth and suggest that changes in bone may be co-regulated by similar genes during this development period. The intrinsic stiffening of the bone, however, lags considerably behind the initial mineral formation, emphasizing the importance of bone mineral quality for optimizing matrix integrity. With clear evidence that bone's chemical properties and micro-structure play an important role in defining the micro-mechanical properties of the skeleton during growth, a better mechanistic understanding of the underlying processes may enable the diagnosis, prevention, and treatment of poor bone quality.

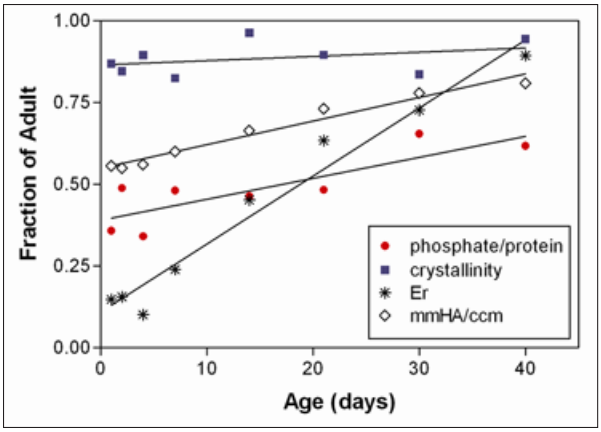

Figure 1. *In this study, tibiae of female BALB mice were harvested at 8 time points (n=4 each) distributed between 1d and 40d of age. Tibiae of 450d old mice served as fully mineralized control specimens.* ***(A)*** *Micro-CT and* ***(B)*** *FTIRM phosphate/protein images of the mouse mid-diaphysis at 1d, 4d, 14d, and 40d of age. All images for each technique are plotted on the same intensity scale for direct comparison. Results showed that the spatial variability in mineralization across the mid-tibia was very high for the early time points and declined over time.*

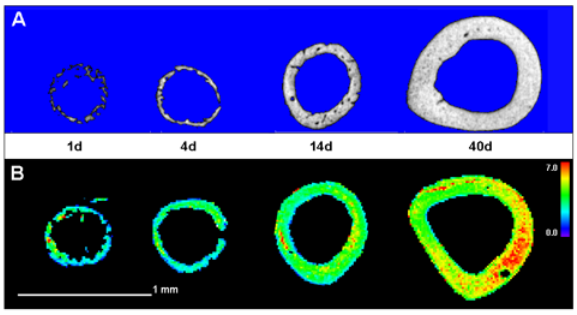

Figure 2. *Phosphate/protein, crystallinity, elastic modulus, and TMD as a function of age. In order to compare all parameters on a common scale, the y-axis values represent the fraction of the adult (15mos) value. Results showed that bone mineralization (phosphate/protein ratio, crystallinity, and TMD) proceeded quickly at an early age, whereas bone stiffness (elastic modulus) lagged behind. This initial lag in elastic modulus may be associated with the specific locations of the mineral crystals within the collagen fibrils.*

BEAMLINE
X29

PUBLICATION
Z. Zhou, J. Zhen, N. Karpowich, R. Goetz, C. Law, M. Reith, and D. Wang, "LeuT-Desipramine Structure Reveals How Antidepressants Block Neurotransmitter Reuptake," *Science*, **317,** 1390 (2007).

FUNDING
National Institutes of Health
National Institute on Drug Abuse

FOR MORE INFORMATION
Maarten E.A. Reith, Department of Psychiatry, New York University School of Medicine
maarten.reith@med.nyu.edu

Da-Neng Wang, Skirball Institute of Biomolecular Medicine, New York University School of Medicine
wang@saturn.med.nyu.edu

LeuT-Desipramine Structure Suggests How Antidepressants Inhibit Human Neurotransmitter Transporters

Z. Zhou[1], J. Zhen[2], N.K. Karpowich[1], R.M. Goetz[1], C.J. Law[1], M.E.A. Reith[2] and D-N Wang[1]

[1]Skirball Institute of Biomolecular Medicine, and [2]Department of Psychiatry, New York University School of Medicine

Tricyclic antidepressants exert their pharmacological effect – inhibiting the reuptake of serotonin, norepinephrine and dopamine – by directly blocking neurotransmitter transporters in the presynaptic membrane. We determined the crystal structure at 2.9 Å of the bacterial leucine transporter (LeuT), a homolog of the human transporters, in complex with leucine and the antidepressant desipramine. Desipramine binds at the inner end of the extracellular cavity of the transporter and this binding site is separated from the leucine-binding site. Mutagenesis experiments on human proteins indicate that both the desipramine-binding site and its inhibition mechanism are probably conserved in the human neurotransmitter transporters

Na^+/Cl^--dependent neurotransmitter transporters for serotonin (SERT), norepinephrine (NET), and dopamine (DAT) in the presynaptic plasma membrane terminate neuronal signal transmission in the central nervous system through a reuptake mechanism. These three systems have been shown to modulate mood, emotion, sleep, and appetite. Depression, the most prevalent psychiatric disorder, is directly associated with perturbation of serotonergic neurotransmission, and drugs have been used successfully for the treatment of depression. One class of drugs, tricyclic antidepressants (TCAs) such as desipramine, binds to serotonin and norepinephrine transporters and blocks their transport activity. However, their binding site in the transporter proteins had not been identified.

To investigate the molecular basis of TCA binding to LeuT, we co-crystallized LeuT with desipramine and solved the complex structure to 2.9 Å resolution. X-ray diffraction data were collected at NSLS beamline X29. The diffraction data was initially refined against the TCA-free LeuT structure. The final LeuT-desipramine complex model had an R_{free} 21.9% and an R_{work} of 20%. The bound desipramine molecule sits at the inner end of the extracellular cavity in LeuT (Figure 1). Importantly, the desipramine molecule is separated from the substrate leucine by the extracellular gate of the transporter, which consists of residues R30, Y108, F253, and D404. Thus, the desipramine-binding site and the leucine-binding site are non-overlapping. On the extracellular side, desipramine is held in place by the turn of the EL4 helix hairpin, and nitrogen N2 atom the tail of desipramine forms a salt bridge with D401. This crystal structure of LeuT-desipramine complex immediately suggests a mechanism for inhibition of substrate transport by the TCA molecule. Desipramine directly binds to the extracellular gate of the transporter and locks the gate by inducing formation of a salt bridge between R30 of TM1 and D404 of TM10. The formation of this salt bridge prevents tilting of TM1, which is believed to be required for substrate release to the cytosol. Thus, no substrate transport can occur.

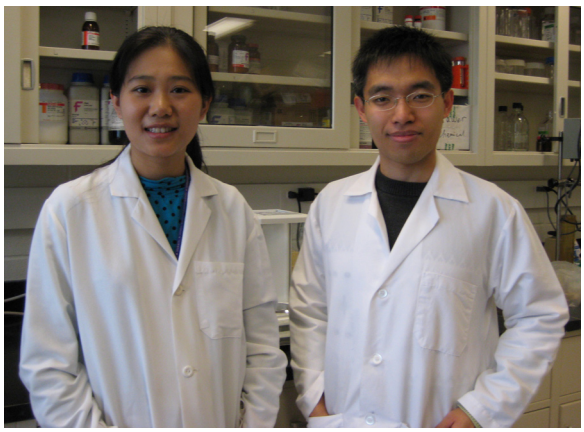

Authors (from left) Juan Zhen and Zheng Zhou

We tested the relevance of this desipramine-binding site identified in the bacterial protein to neurotransmit-

ter reuptake inhibition by mutating key residues at the presumed TCA-binding site in the human neurotransmitter transporters SERT and DAT, followed by measuring their transport inhibition by desipramine in human embryonic kidney cells. We succeeded in generating gain-of-function mutants in terms of desipramine binding for both DAT and SERT proteins by mutating their key residues to those found in the sequence of NET. Such gain-of-function mutagenesis data clearly demonstrate that desipramine binds to the same site in both DAT and SERT as it does in LeuT and inhibits transport activity in the same manner.

Thus, in the human Na^+/Cl^--dependent neurotransmitter transporters SERT, NET, and DAT it is likely that tricyclic antidepressants also bind between the extracellular gate and EL4 hairpin, thereby inhibiting neurotransmitter reuptake at the synapse. In combination with homology modeling and molecular docking, the identification of this drug-binding site will allow studies on the interactions of SERT- and NET-specific inhibitors with these transporters and may aid in the structure-based design of more effective neurotransmitter reuptake inhibitors as antidepressants.

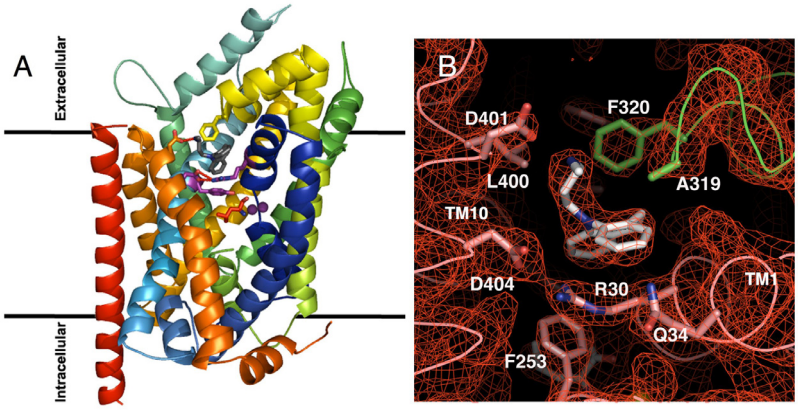

Figure 1. *Structure of the LeuT-desipramine complex. (A). Over structure of the LeuT-desipramine complex showing the position of the bound desipramine, viewed from within the membrane plane. (B). $2F_o$-F_c map contoured at 2 σ showing the desipramine binding site in LeuT, viewed from within the membrane plane. Residues R30, Y108, F253 and D404 form the extracellular gate, which separates the leucine substrate from the bound desipramine.*

BEAMLINE
X9A

PUBLICATIONS
I. Melčák, A. Hoelz and G. Blobel, "Structure of Nup58/45 Suggests Flexible Nuclear Pore Diameter by Intermolecular Sliding," *Science*, **315** 1729-1732 (2007).

FUNDING
Howard Hughes Medical Institute
Leukemia and Lymphoma Society

FOR MORE INFORMATION
Günter Blobel or André Hoelz, Laboratory, Cell Biology, Howard Hughes Medical Institute, The Rockefeller University
blobel@rockefeller.edu
hoelza@rockefeller.edu

Nucleoporin Crystal Structure Suggests Flexible Pore Diameter by Intermolecular Sliding

I. Melčák, A. Hoelz, and G. Blobel

Laboratory of Cell Biology, Howard Hughes Medical Institute, The Rockefeller University

The exchange of macromolecules across the nuclear envelope is mediated through the nuclear pore complex (NPC). During the cargo translocation, the central channel of the NPC is thought to alter its diameter. We present the atomic structure of nucleoporin Nup58/45, a component of a central channel. In the crystal structure of an α-helical region of Nup58/45, we identified distinct tetramers of different conformations. These conformations reveal that dimer subunits of Nup58/45 tetramers may slide against one another over a distance of ~11 Å. The lateral displacement of α-helices is accompanied by formation of an alternative hydrogen-bond network. We suggest that these data may provide an explanation for the adjustable transport channel.

The nuclear pore complex (NPC) embedded in the nuclear envelope gates macromolecular traffic between the nucleus and cytoplasm. The central conduit channel is formed by an eight-fold symmetrical assembly composed of a set of proteins called nucleoporins. To accommodate the passage of cargo, large-scale structural rearrangements might occur to adjust the central channel diameter. However, the molecular details of such structural changes are unknown.

The central channel of the NPC is lined by the Nup62 complex, which consists of Nup62, Nup54, Nup58, and Nup45. The minimal core domains of Nup58 and Nup45 are identical α-helical regions (referred to as Nup58/45) and are sufficient for Nup62 complex assembly.

We identified two similar, structurally distinct Nup58/45 tetramers in two independent crystal forms that result from the dimerization of identical dimers (**Figure 1A**). Each protomer folds into an antiparallel hairpin structure and the protomers dimerize to form a four-helix bundle. The dimers interact with each other in a "head-to-head" orientation with their N helices. The tetramerization interface is formed by an extensive side-chain hydrogen bond network that ties the N-helices of the four protomers together. Most of the interactions occur within each pair of aligned, anti-parallel N-helices, involving polar and/or charged side-chains. The two conformers differ by an ~6 Å lateral displacement of their dimer subunits along the long axis of the tetramerization interface. By superposition of all four pairs of N-helices, four different configuration states can be discerned that exhibit a maximum lateral displacement of ~11 Å (**Figure 1B**). The rearrangement of the dimer-dimer interaction surface results in the formation of alternative hydrogen-bond networks. The identification of multiple interaction states in which rigid Nup58/45 dimers are sequentially shifted along the dimer-dimer suggests an intermolecular sliding mechanism. The residues of the sliding surface have two major features: (i) propensity of switching interaction partners by acting alternatively as either hydrogen-bond donors or acceptors, or as both, (ii) sampling capability of the flexible long side chains.

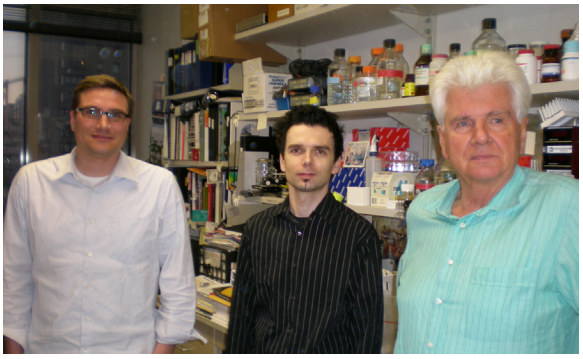

Authors (from left to right) André Hoelz, Ivo Melčák and Günter Blobel

The mutual arrangement of subunits within a single sliding module can be altered by a distance of at least ~11 Å (**Figure 1C**). We propose that circumferential sliding of Nup58/45 in the channel perimeter results in an adjustable diameter as cargo passes across.

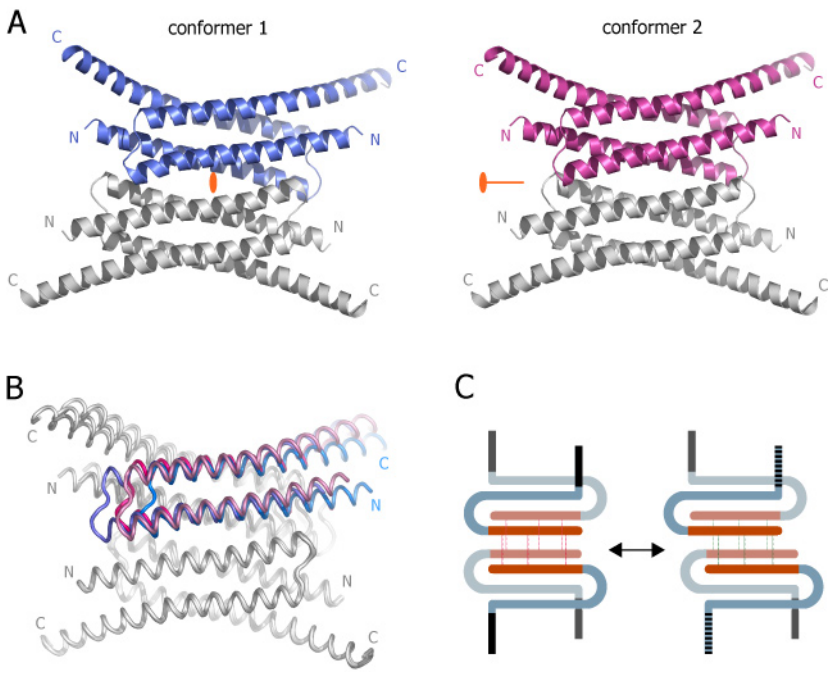

Figure 1. *Structures of tetrameric Nup58/45 assemblies. (A) Ribbon representations of the two tetrameric conformers. The different coloring of dimers (blue, conformer 1; purple, conformer 2) illustrates the alternative tetrameric configurations of the two conformers. The crystallographic two-fold axes (orange) are indicated. (B) Superposition of the two tetrameric Nup58/45 conformers. The unique protomers of the two tetrameric assemblies are superimposed to highlight the lateral shift between the different conformers. For clarity, only one protomer of each superposition is colored. (C) Schematic representation of the Nup58/45 sliding module. The four N helices that generate the tetramerization interface (orange) and the C helices (light blue) are indicated. The sliding of the Nup58/45 dimer surfaces formed by the N helices is facilitated by an alternative hydrogen bond network (red and green thin lines).*

BEAMLINES
X6A, X29

PUBLICATION
Y. Wang, Y. Zhang, and Y. Ha, "Crystal Structure of a Rhomboid Family Intramembrane Protease," *Nature*, **444**, 179-183 (2006).

FUNDING
Ellison Medical Foundation
Neuroscience Education and Research Foundation

FOR MORE INFORMATION
Ya Ha, Department of Pharmacology, Yale University School of Medicine
ya.ha@yale.edu

Crystal Structure of Intramembrane Protease GlpG

Y. Wang, Y. Zhang, and Y. Ha

Department of Pharmacology, Yale School of Medicine, New Haven, CT

Intramembrane proteolysis was initially a controversial concept because proteolytic reactions, which involve water, usually take place in aqueous solutions instead of within cell membranes. Now we know that intramembrane proteolysis is common in biology, and is responsible for generating amyloid β-peptide that causes Alzheimer's disease. The crystal structure of GlpG describes for the first time with atomic resolution the architecture of one membrane protein that specializes in catalyzing this reaction, and illustrates the physical principles that underlie its unique mechanism.

Escherichia coli GlpG is an integral membrane protein that belongs to the rhomboid protease family. The crystal structure of GlpG core catalytic domain has been solved at 2.1 Å resolution based on x-ray diffraction data collected at the NSLS.

The structure of GlpG contains six transmembrane helices (**Figure 1**). Inside the bundle of transmembrane helices is a cavity (above the yellow helix S4). The cavity opens toward the outside of the cell, and is tightly capped by the L5 loop. The L1 loop appears to be embedded in the outer leaflet of the membrane as judged by its position relative to the transmembrane helices.

The crystal structure correlates well with published sequence and functional data on related rhomboid proteases (**Figure 2**). The internal cavity harbors all the polar residues from the transmembrane segments (His-150, Asn-154, Ser-201, His-254). A fully extended L3 loop, as well as the exposed N-terminus of helix S4, also contributes polar groups to the cavity. These features suggest that the cavity represents the active site of the protease. Substituting each of the conserved Gly-199, Ser-201, and His-254 invariably abolishes activity (colored red in the figure). Mutations of His-150 and Asn-154 also affect the activity for some rhomboid proteases, but not all (orange).

The active site is surrounded by five transmembrane helices. Between helices S1 and S3 sits the interesting L1 loop. The function of the loop in enzyme mechanism is not yet clear. Mutating Trp-136 or Arg-137, two preferred residues on L1 and 15 Å away from the active site, either abolishes or reduces protease activity (yellow in the figure).

The electron density map reveals several water molecules present in the cavity (**Figure 3**). When the L5 loop "opens," water can diffuse easily into the active site and react with substrate. These observations solve the long-time puzzle of a water-requiring reaction in the middle of cell membranes.

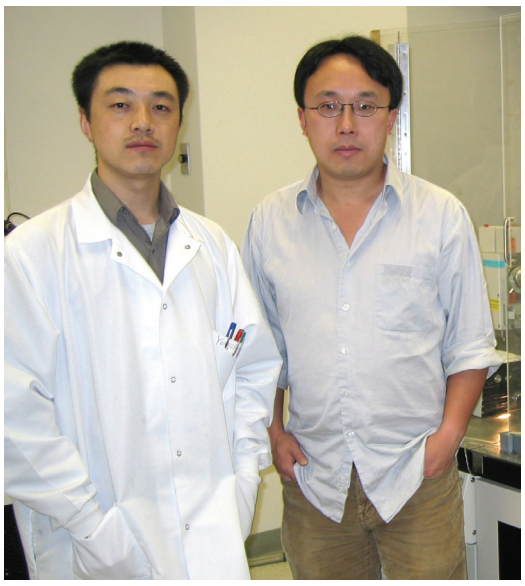

Yongcheng Wang (left) and Ya Ha

The crystal structure of GlpG illustrates the following physical principles underlying the mechanism of intramembrane proteolysis: the active site of the protease is positioned into the membrane at a distance roughly matching the cleavage site of the substrate; the hydrophilic active site is separated from the lipid by protein structures; substrate binding triggers conformational changes in the protease, which causes the L5 cap to open; substrate enters the protease laterally from its own transmembrane location and becomes hydrolyzed.

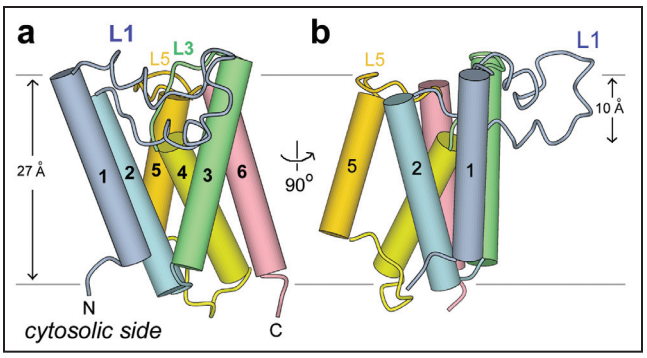

Figure 1. *The overall structure. (a) The front view. The transmembrane helices shown as cylinders are sequentially labeled 1-6. The two horizontal lines mark the boundaries of the membrane. (b) The side view related to (a) by a 90-degree rotation as shown.*

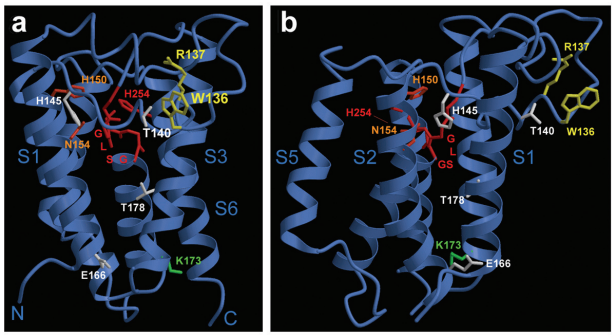

Figure 2. *Mutagenesis studies on related rhomboid proteases mapped onto GlpG structure. The GLSG (Gly-199, Ser-201) sequence motif and His-254 are shown in red; His-150 and Asn-154 in orange; Trp-136 and Arg-137 in yellow. (a) and (b) represent different views.*

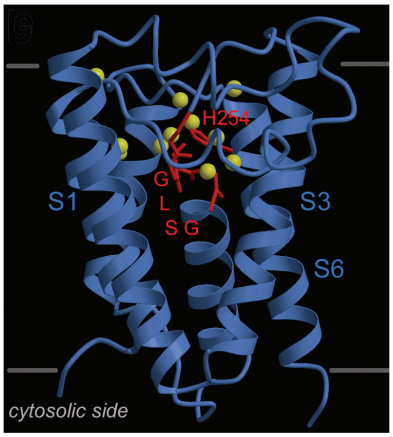

Figure 3. *The active site is filled with water (yellow spheres).*

BEAMLINE
X9B (now X3B)

PUBLICATION
D.C. Kennedy, R.W. Herbst, J. S. Iwig, P.T. Chivers, and M.J. Maroney, "A Dynamic Zn Site in Helicobacter pylori HypA: A Potential Mechanism for Metal-Specific Protein Activity," *J. Am. Chem. Soc.*, **129**(1); 16-17 (2007).

FUNDING
The National Institutes of Health
U.S. Department of Energy

FOR MORE INFORMATION
Michael J. Maroney, Department of Chemistry, University of Massachusetts
mmaroney@chemistry.umass.edu

A Dynamic Zn Site in *Helicobacter pylori* HypA – A Potential Mechanism for Metal Specific Protein Activity

D.C. Kennedy[1], R.W. Herbst[1], and M.J. Maroney[1]

[1]Department of Chemistry, University of Massachusetts, Amherst, MA

In order to import, transport, export, and maintain homeostatic levels of intracellular transition metal ions, organisms have evolved trafficking proteins that often exhibit a biological response to the binding of a particular metal. How proteins achieve this specificity is largely unknown. HypA is an accessory protein and a putative metallochaperone that is critical for supplying nickel to the active site of NiFe hydrogenases. In addition to binding Ni(II), HypA also contains a zinc site that has been suggested to play a structural role. X-ray absorption spectroscopy (XAS) was used to show that the zinc site changes structure from a S_3(O/N)-donor ligand environment to an S_4-donor ligand environment upon binding nickel. This provides a potential mechanism for discriminating Ni(II) from other divalent metal ions.

The use of reactive and potentially toxic transition metals in enzyme active sites depends on proteins that can acquire metals from the environment (*e.g.,* permeases), transport them inside cells and incorporate them into apoenzymes (*e.g.,* metallochaperones), and control their intracellular concentration (*e.g.* transcriptional regulators), often with great specificity for the cognate metal. How metal-specific responses are achieved is largely unknown, but appears to involve allosteric mechanisms that differ in the details of how the identity of the metal bound is communicated to the protein structure. HypA is one of three proteins (HypA, HypB, and SlyD) that have been identified in assisting in the incorporation of Ni(II) into NiFe hydrogenase in *Escherichia coli* (*Ec*). The proper functioning of HypA has also been implicated in the insertion of Ni(II) into urease in *Helicobacter pylori* (*Hp*). Our recent work at the NSLS focused on understanding the structural environments of both the Ni(II) ion and a structural Zn(II) ion present in *Hp*HypA with the goal of understanding how this protein discriminates Ni(II) from other divalent metal ions. Our study of the Zn(II) site has shown that changes in the ligand environment of this metal site that accompany the binding of Ni(II) may indicate to the protein that the correct metal [Ni(II)] has been bound.

Authors (from left, back) Jeff Martin, Robert Herbst, David Kennedy, Crisjoe Joseph, and Jonathan Leung; (front) Cecilia Doddi, Sharon Leitch, Michael Maroney, Khadine Higgins, Kelly Ryan, and Kerrie O'Brien

The amino acid sequence of *Hp*HypA (**Figure 1**) contains two conserved CXXC motifs that have been shown to be involved in binding the Zn(II) ion in *Ec*HypA. Our work is the first to show that in the absence of Ni, only three of these cysteines are coordinated to the Zn. The fourth ligand, identified only as a nitrogen- or oxygen-donor, is displaced upon the coordination of Ni(II) by the fourth cysteine residue. The Fourier-transformed EXAFS spectra (**Figure 2**) for the Zn(II) site clearly show this change in ligand environment upon Ni(II) coordination. The zinc site in the protein with no other metal bound is best described as involving an S_3(N/O) ligand donor-atom environment. Upon binding Ni(II), the zinc site structure changes to

one that is best described as an S_4 ligand donor-atom environment. These changes may represent either changes in the protein structure that constrain the zinc site structure, or a competition between the Zn(II) and Ni(II) ions for the N/O donor involved. Either case could lead to a mechanism for specific recognition of Ni(II) binding in HypA.

Analysis of XANES and EXAFS data show that the Ni(II) site contains six N/O-donor ligands that include 1-2 histidine imidazole groups. The coordination environment of Ni(II) in *Hp*HypA is very similar to the Ni(II) site in UreE, the only other characterized Ni-binding domain in a metallochaperone. The Ni(II) site in UreE is also six-coordinate and composed of N/O-donor atoms including two histidines. This binding motif may represent a general structure that nature has evolved for metallochaperones involved in the incorporation of Ni(II) ions in ureases, hydrogenases, and potentially other Ni metalloenzymes for which chaperones have yet to be identified.

Figure 1. *Sequence alignment of E. coli and H. pylori HypA (potential metal ligands including two conserved CXXC domains are highlighted).*

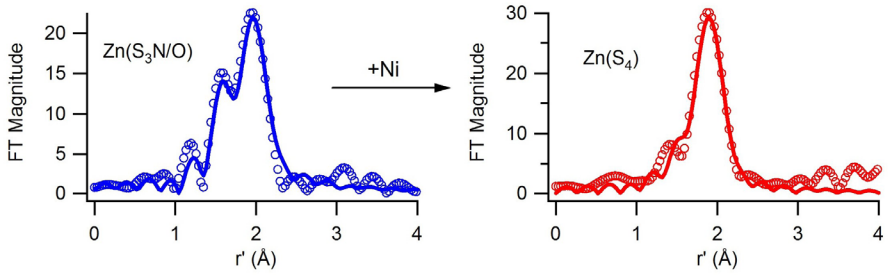

Figure 2. *The Fourier-transformed EXAFS spectra of the zinc site in the nickel-free (left) and nickel-bound (right) HypA proteins clearly showing the change in coordination environment at the zinc center.*

BEAMLINES
X4A, X26C

PUBLICATION
P.F. Widboom, E.N. Fielding, Y. Liu, and S.D. Bruner, "Structural Basis for Cofactor-Independent Dioxygenation in Vancomycin Biosynthesis," *Nature*, **447**, 342-345 (2007).

FUNDING
Damon Runyon Cancer Research Fund
National Science Foundation
Boston College

FOR MORE INFORMATION
Steven Bruner, Boston College, Merkert Chemistry Center
bruner@bc.edu

Structural Basis for Cofactor-Independent Dioxygenation in Vancomycin Biosynthesis

P.F. Widboom, E.N. Fielding, Y. Liu, and S.D. Bruner

Department of Chemistry, Merkert Chemistry Center, Boston College

The enzyme DpgC performs a key step in the biosynthesis of the important antibiotic vancomycin. The catalyst performs unique oxidation chemistry without the assistance of any metal or cofactor. Typically, a cofactor is needed to activate molecular oxygen for downstream reactions. We have solved the first structure of DpgC using atomic resolution x-ray diffraction crystallography. The structure provides an exceptional amount of detail regarding the novel DpgC reaction pathway and the general mechanism of enzymatic oxygen activation. In a rare example, molecular oxygen is observed bound to the enzyme in the reactive conformation.

All living organisms exploit the reactivity of molecular oxygen for critical processes such as energy production and the synthesis of cellular components. The direct reaction of molecular oxygen with organic molecules is formally a disallowed, spin-forbidden transformation. The vast majority of characterized oxygenases utilize bound transition metals or flavin cofactors to activate triplet molecular oxygen in order to carry out diverse oxidation chemistry. The vancomycin biosynthetic enzyme DpgC is a unique catalyst that performs a dioxygenation reaction independent of metals or cofactors. The enzyme DpgC catalyzes a key step in the biosynthesis of 3,5-dihydroxyphenylglycine (DPG), a nonproteinogenic amino acid found in the vancomycin family of antibiotics (**Figure 1A**). DpgC is a dioxygenase, incorporating two oxygen atoms from the same molecule of molecular oxygen into the substrate resulting in the four-electron oxidation and the cleavage of the thioester bond (**Figure 1B**). This combination of transformations has no precedent in characterized enzymes.

The x-ray structure of DpgC was solved through single-wavelength anomalous diffraction (SAD) phasing of a selenomethionine derivative to 2.75 Å resolution. The structure of the apo-enzyme contains numerous disordered regions, especially in proximity to the predicted active site. To resolve the problems of disorder in the crystal, a substrate analog was designed and synthesized for use in co-crystallization studies. The co-complex crystallized in the space group $P2_12_12$ to 2.40 Å resolution (**Figure 2A**). The substrate analog is clearly evident in the electron density maps (**Figure 2B**). The substrate analog is positioned properly in an "oxyanion hole" similar in architecture to that previously described for other homologous members of the crotonase superfamily.

The orientation of the substrate suggests molecular oxygen will react with the α-carbon of the substrate. At this predicted position, unassigned electron density consistent in size and shape with diatomic molecular oxygen is evident in the electron density maps. Oxygen is bound in a well-defined, solvent-accessible hydrophobic pocket. Soaking of our co-complex crystals under high pressures of xenon gas failed to displace the observed bound oxygen, suggesting the oxygen is bound with unique specificity. An ordered dioxygen molecule at the observed position is consistent with the unusual chemistry of DpgC. The proposed mechanism first involves formation of a thioester enolate. Molecular oxygen, bound in a hydrophobic pocket, is properly positioned to react with the substrate through a two-step process. The first step is the transfer of an electron from the substrate to triplet

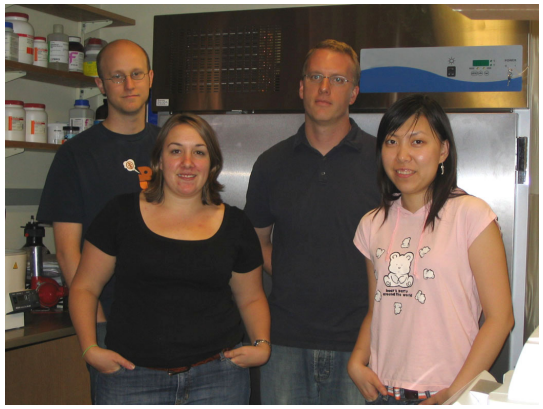

Authors (from left) Paul Widboom, Elisha Fielding, Steven Bruner and Ye Liu

oxygen, forming a conjugated radical cation/superoxide pair. The pair can then collapse in a spin-allowed, bond-forming process to give a peroxide intermediate. This peroxide can proceed to the observed product, DPGX, through a 1,2-dioxetanone.

In summary, the structure of DpgC provides detailed information regarding the specific interaction with an oxygenase and a bound, isolated oxygen molecule. In addition, the structure reveals novel insights that can be applied to the general mechanism of enzymatic oxygen activation.

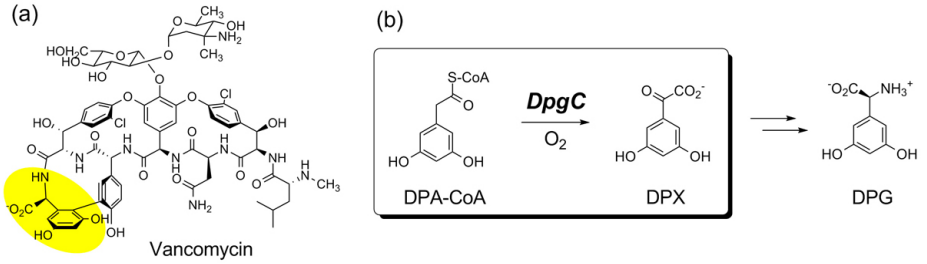

Figure 1. *(a) Chemical structure of the antibiotic vancomycin with the amino acid building block DPG (3,5-dihydroxyphenylglycine) highlighted in yellow. (b) The conversion of DPA-CoA to DPGX and coenzyme A (CoA) catalyzed by DpgC.*

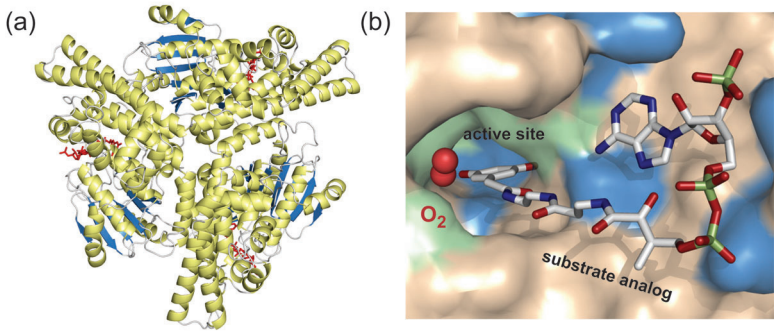

Figure 2. *(a) Ribbon diagram of DpgC looking down the 3-fold axis of the protein hexamer, α-helices are colored yellow and β-sheets blue. The bound substrate analog is shown in red. (b) Surface representation of the hydrophobic oxygen-binding pocket of DpgC. The hydrophobic surfaces are colored green and areas directly involved in substrate recognition blue. Molecular oxygen is shown in van der Waals representation (red).*

BEAMLINE
X25

PUBLICATION
Y. Wang and Y. Ha, "Open-Cap Conformation of Intramembrane Protease GlpG," *Proc. Natl. Acad. Sci.*, **104**, 2098-2102 (2007).

FUNDING
Ellison Medical Foundation
Neuroscience Education and Research Foundation

FOR MORE INFORMATION
Ya Ha, Department of Pharmacology, Yale University School of Medicine
ya.ha@yale.edu

Open Structure of Intramembrane Protease GlpG

Y. Wang and Y. Ha

Department of Pharmacology, Yale School of Medicine

The active sites of the intramembrane protease, E. coli. rhomboid GlpG, are buried in the lipid bilayer when it is in a closed conformation without a bound substrate. How transmembrane substrates enter the internal and closed active sites remains an open question. Here we describe the crystal structure where the capping L5 has been lifted. The changes following the loop movement surrounding the active sites contribute to a more open conformation. The unexpected experimental results reveal the conformational flexibility and plasticity of GlpG, which may function to accommodate substrate binding and catalysis.

The first crystallographic analysis of the E. coli rhomboid protease GlpG confirmed that the active sites of intramembrane proteases are positioned in the lipid bilayer. The structure of GlpG contains six transmembrane helices (S1-S6) and is apparently in a closed conformation, where the internal active site is covered tightly by the capping loop L5. A new open-cap conformation crystal structure, owing to the loop L5 movement, has been solved at 2.5Å based on the data collected at the NSLS.

The crystal structure (**Figure 1A**) confirmed that L5 (residues 245-249) was lifted away from the original internal and hydrophilic active sites, and the two side chains (Met-247 and Met-249) were sequentially pulled away from the immediate vicinity of Ser-201. The void left behind was occupied by new water molecules. A neighboring His-150 moved in and overlapped with the original path of L5 main chain. An open trough appears on the top of the membrane-embedded protease (**Figure 1B**), which could be where substrate binds.

The oxyanion-binding site in the closed state of GlpG was not obvious because of the two methionine side chains impending over the active sites. While in the open state of GlpG, water molecules immobilized in the active site slightly adjusted their positions. One water, previously bound between Ser-201, His-150, and Gly-198, had moved to a new location, where it broke off the hydrogen bond with the backbone carbonyl of Gly-198 and formed a new bond with the side chain amide of Asn-154 (**Figure 1C**). This new location corresponds roughly to where the oxyanion hole for a classic serine protease is.

The loop L5 movement creates a lateral opening (**Figure 2**). In the closed structure, the side chain of Phe-245 is inserted into a gap between transmembrane helices S2 and S5, roughly at the same level of the internal active site. Phe-245 physically separates the membrane-embedded active site from the lipid. In the open-cap structure, Phe-245 became disordered, the lightly inward adjustment from the side chain of Met-249 was not sufficient to bridge the gap. An opening was left in the wall of protein structures that surrounded the active site, exposing internal hydrophilic residues unfavorably to lipid.

This unexpected structure, combined with the previous closed structure, illustrates our thoughts on the role of L5 in the proteolysis process. In the closed structure, the active sites are completely buried inside the membrane protein. The protein structure must become open to

Yongcheng Wang

Ya Ha

accommodate a substrate. In the open-cap structure, the loop L5 is displaced from its original position. This movement of the L5 cap exposes the putative oxyanion hole and creates a side portal. The comparison of the two structures implies the following: the docking of substrate transmembrane domain near the S2/S5 gap could cause the L5 cap to open so that the top portion of the substrate could access the active site.

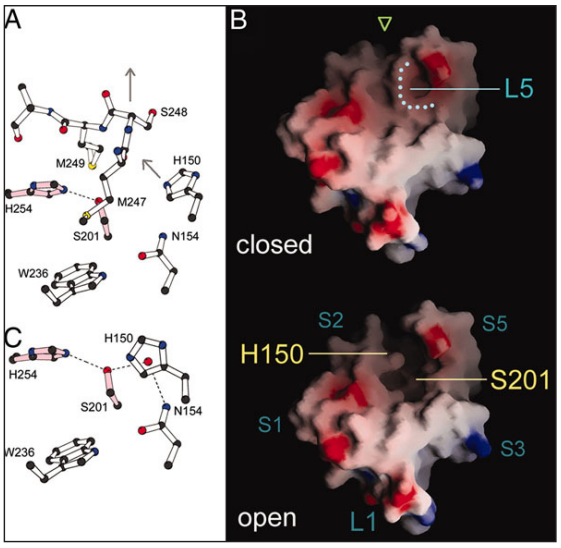

Figure 1. *The active site is exposed in the open-cap conformation. (A) Detailed picture of the closed cap and the catalytic dyad of GlpG (back view). (B) Comparison of the surface features of the closed- and open-cap GlpG structures (top view). Blue areas are positively charged, and red areas are negatively charged. The dotted line marks the path of L5 in the closed structure. (C) With the cap lifted, a water molecule (red dot) moves into the putative oxyanion hole.*

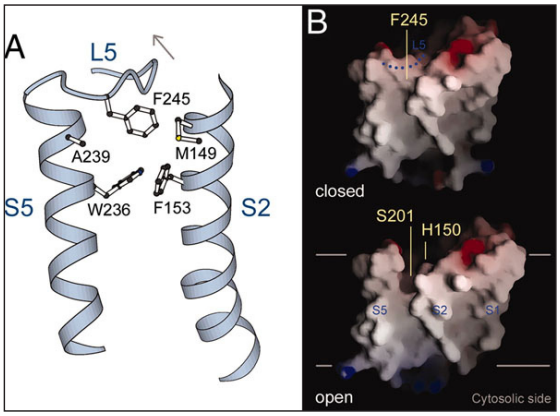

Figure 2. *Cap movement creates a lateral opening. (A) Phe-245 is normally inserted between S2 and S5, blocking an entrance to the active site (back view). (B) Molecular surface of GlpG (back view). Blue areas are positively charged, and red are negatively charged. The two horizontal lines mark the hydrophobic region of lipid bilayer. The dotted line depicts the path of L5 in the closed structure.*

BEAMLINES
X6A, X25

PUBLICATION
S.B. Gabelli, H.F. Azurmendi, M.A. Bianchet, L.M. Amzel, and A.S. Mildvan, "X-ray, NMR, and Mutational Studies of the Catalytic Cycle of the GDP-Mannose Mannosyl Hydrolase Reaction," *Biochemistry*, **45**(38), 11290-303 (2006).

FUNDING
The National Institutes of Health

FOR MORE INFORMATION
Sandra B. Gabelli, L. Mario Amzel and Albert S. Mildvan; Dept. of Biophysics and Biophysical Chemistry; The Johns Hopkins University
sandra@groucho.med.jhmi.edu

A Loop in Action: the Mechanism of the GDP-Mannose Mannosyl Hydrolase

S.B. Gabelli[1], H.F. Azurmendi[2], M.A. Bianchet[1], L.M. Amzel[1], and A.S. Mildvan[2]

[1]Department of Biophysics and Biophysical Chemistry; [2]Department of Biological Chemistry, The Johns Hopkins University School of Medicine

GDP-mannose hydrolase (GDPMH) catalyzes the hydrolysis with inversion of GDP-α-D-hexose to GDP and β-D-hexose by nucleophilic substitution at C1 of the hexose.

While the enzyme structure was known, little was understood about the dynamic processes that contribute to the reaction mechanism. This work identifies the motions in GDPMH involved in enzyme catalysis. We used crystal structures, and NMR studies, as well as site-directed mutagenesis and molecular modeling of the transition state to depict four stages in the catalytic cycle of this enzyme: free enzyme, substrate complex, transition state complex, and product complex.

The three structures of GDPMH – free enzyme, substrate complex, and product complex – suggest that major conformational changes take place during the hydrolysis of GDP-mannose. In the structure of the free enzyme, loop L6 spanning residues 119 to 125 is dynamically disordered (**Figure 1A**) as indicated by the lack of density in the x-ray structure and by the broadening of the imidazole ^{15}N resonance of His-124 in the HMQC spectrum (**Figure 1B**). The H124Q mutation decreases k_{cat} $10^{3.4}$-fold and largely abolishes its pH dependence. The structure of the GDPMH-Mg^{2+}-GDP-mannose complex (substrate complex), carried out using the Y103F mutant (k_{cat} two orders of magnitude lower than that of the wild type enzyme) shows that after binding Mg^{2+} and GDP-mannose, the loop becomes ordered but in an open conformation in which the catalytic base, His-124, is 12 Å away from the position required for catalysis (**Figure 1A, 2B**). This open conformation of the substrate complex appears incompatible with the catalytic requirements of the enzyme.

In the structure of the product complex, on the other hand, the loop closes onto the catalytic site, bringing His-124 into the position in which it can act as the catalytic base (closed conformation) (**Figure 1A, 2D**). The lack of the tyrosine-OH group could prevent the bound substrate from triggering the conformational change to that observed in the product complex. However, there is no direct involvement of the tyrosine-OH in stabilizing the closed conformation. A better explanation is that the partial positive charge developing on C1 of the mannose during hydrolysis causes loop L6 to close. A closer look at the structure of the product complex supports this hypothesis, since the product structure contains a cationic Tris molecule bound in the catalytic site in the position occupied by the substrate mannose in the substrate complex. The hydroxyl groups of the Tris molecule make hydrogen bonds with side chains of the same residues that bind the mannose in the substrate complex. Hence, it appears that closing of the negatively charged catalytic loop L6 (which contains Asp-121, Glu-122, and Asp-125) is driven by the positive charge that is developing on C1 of the mannose. In the Y103F mutant, the loop L6 does not close because the hydroxyl of Tyr-103, which makes a hydrogen bond to the leaving oxygen atom of the β-phosphate, is probably required for the charge separation that takes place in the partially dissociative mechanism.

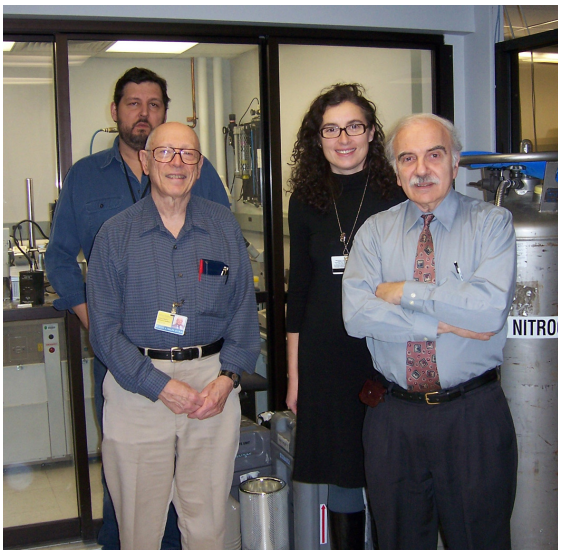

Authors (from left) Mario A. Bianchet, Albert S. Mildvan, Sandra B. Gabelli, and L. Mario Amzel

The group's research was showcased on the cover of the October 2, 2006 edition of Biochemistry.

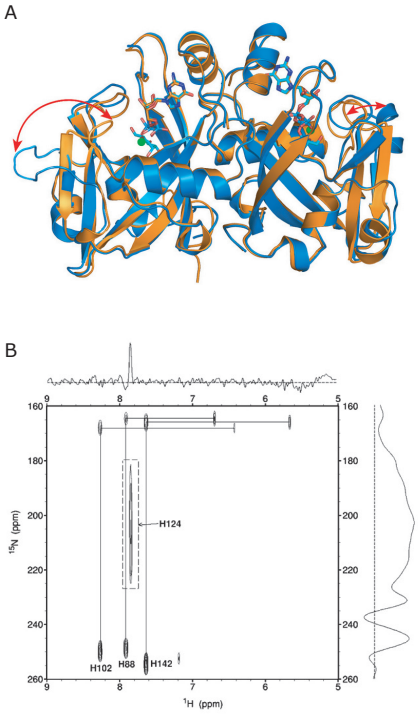

Figure 1. *Dynamics in the mechanism of GDPMH. (A) Structural Superposition of the crystal structures of the closed product complex of GDPMH (orange), and the open substrate complex of the Y103F mutant enzyme (blue). The catalytic metals are shown as green spheres. The structures show the amplitude of motion of the catalytic loop L6 between the closed (active) and open state (inactive). (B) 2D ^{1}H-^{15}N HMQC spectrum of the imidazole region of free, wild type GDPMH at 30°C and pH 8.3. Note the broadening of the imidazole ^{15}N resonance of His-124.*

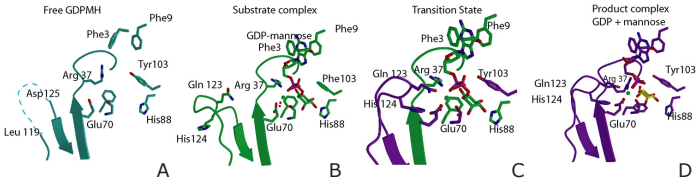

Figure 2. *Snapshots of the catalytic cycle of GDPMH. (A) Crystallographic structure of the free enzyme. In this structure, loop L6 (dotted line) is disordered at the beginning of the cycle (pdb id 2GT2). (B) X-ray structure of the substrate complex. In this structure, although loop L6 becomes ordered, it remains in an "open" conformation (PDB id 1GT4). (C) Model of the GDPMH-transition state complex. This model was obtained by combining the coordinates of the enzyme in the product structure with the position of the GDP-mannose in the substrate structure (PDB id 2GT4) distorting the mannose to a half chair and elongating the mannosyl C1-GDP bond. In this model, loop L6 is in the "closed" conformation, bringing residues Gln123 and His 124 into their active positions. This conformational change is probably triggered by the positive charge developing on C1 of the mannose in the partially dissociative transition state acting on the negative charges in loop L6 (Asp-121, Glu-122, and Asp-125). (D) Product complex. This structure corresponds to the stage in the catalytic cycle before the release of products (PDB id 1RYA).*

BEAMLINE
X29

PUBLICATIONS
Q. Ye, R.M. Krug, and Y.J. Tao, "The Mechanism by Which Influenza A Virus Nucleoprotein Forms Oligomers and Binds RNA," *Nature*, **444**, 1078-82 (2006).

FUNDING
National Institutes of Health
Welch Foundation
National Science Foundation

FOR MORE INFORMATION
Yizhi Jane Tao, Department of Biochemistry and Cell Biology, Rice University
ytao@rice.edu

Crystal Structure of the Influenza A Virus Nucleoprotein Reveals Architectural Details of the Viral Ribonucleoprotein Complex

Q. Ye and Y.J. Tao

Department of Biochemistry and Cell Biology, Rice University

The segmented, negative-sense RNA genome of the influenza virus is packaged in the form of ribonucleoprotein complexes (RNP), which contain not only the viral RNA, but also multiple copies of the viral nucleoprotein and a viral RNA polymerase. Besides forming the protein scaffold of the viral RNP, the nucleoprotein, one of the most abundant proteins in infected cells, has also been shown to interact with a large number of viral and host factors. The crystal structure of NP provides insights into the high-order structure of the RNP and into how NP may interact with cellular importin and the viral polymerase.

The genome of the influenza virus is organized into eight ribonucleoprotein (RNP) complexes, each of which contains one RNA segment bound to the viral nucleoprotein (NP) at a stoichiometry of one NP per 24 nucleotides, thus forming a rod-shaped, double-helical hairpin structure. The two RNA termini in each RNP are associated with a trimeric viral polymerase at one end of the RNP (**Figure 1**).

To elucidate the architectural details of the RNP, especially how NP interacts with both NP and viral RNA, our laboratory undertook crystallographic studies of the influenza A virus NP. Recombinant nucleoprotein, expressed in either insect cells or *E. coli*, were purified as oligomers of different sizes. Despite the size heterogeneity, NP from the influenza virus A/WSN/33 was crystallized in the space group of $C2_12_12_1$ with one NP trimer per asymmetric unit. Using multiple isomorphous replacement and anomalous scattering (MIRAS), the structure of NP was solved at 3.2 Å resolution.

The structure of NP has the shape of a PacMan with a head and a body domain (**Figure 2**). The polypeptide, which starts in the body domain, winds back and forth between the two domains three times, giving rise to a topology different from that of the rhabdovirus nucleoprotein. In the back of the molecule is a 28aa tail loop, which is inserted inside a neighboring NP and plays an important role in NP-NP interaction in an NCS trimer. Due to flexible linkers between the tail loop and the rest of the NP structure, the same tail loop interaction is observed among the three NCS-related NP, although the rotational angles relating the three subunits varies from 110º to 126º. Indeed, we have found that an inter-subunit salt bridge in the tail loop is essential for NP oligomerization.

The structure of NP, with its calculated electrostatic potential, shows that the large groove between the head and the body domain is likely to be the RNA binding site. Interestingly, this groove is facing the exterior, different from the situation in the rhabdoviruses, where RNA is bound to the interior of the NP oligomeric ring. The RNA binding site of the influenza virus NP contains amino acids widely distributed in sequence, explaining why previous attempts to identify a single RNA-binding domain were not successful. In addition, the first 20aa stretch, which contains a nuclear localization sequence (NLS), is located on the outer surface of the NP trimer and is disordered, allowing importin-α binding and further nuclear import.

Therefore, the crystal structure of NP provides direct evidence that RNA is exposed on the external surface of the influ-

Qiaozhen Ye

Yizhi Jane Tao

enza virus RNPs (**Figure 1**). The tail loop of NP likely mediates the lateral interaction of neighboring NP molecules, which are likely to be slightly offset along the symmetry axis to facilitate the formation of a continuous helix. Because of the tail loop linker flexibility, the same NP-NP interaction can be preserved when the double-helical RNP is unwound to loose polymers during RNA synthesis.

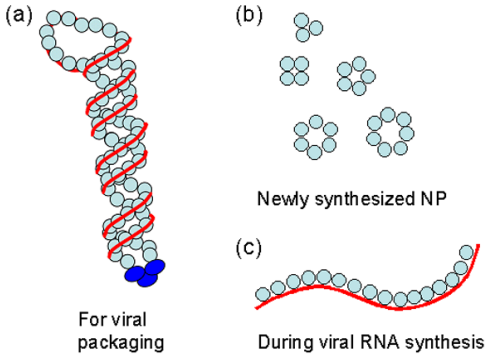

Figure 1. *NP in different functional states. (a) RNP. (b) Newly made NP proteins. (c) Loose NP-RNA polymer. NP molecules are shown by blue circles, RNA by red lines, and viral polymerase by dark-blue ovals.*

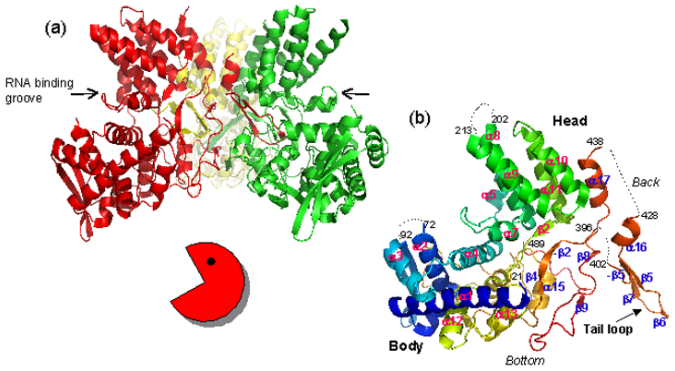

Figure 2. *NP crystal structure. (a) An NCS trimer with three subunits colored differently. (b) The red subunit from (a) colored continuously from N-terminus in blue to C-terminus in red. The disordered termini are marked by amino acid numbers.*

BEAMLINES
X9A, X29

PUBLICATION
I.C. Lorenz, J. Marcotrigiano, T.G. Dentzer, and C.M. Rice, "Structure of the Catalytic Domain of the Hepatitis C Virus NS2-3 Protease," *Nature* **442,** 831-835 (2006).

FUNDING
The National Inst. of Health; the Greenberg Medical Research Inst.; the Swiss National Science Foundation; the Roche Research Foundation; the Swiss Foundation for Medical-Biological Stipends; Life Sciences Research Foundation

FOR MORE INFORMATION
Charles M. Rice, The Rockefeller University
ricec@rockefeller.edu

Crystal Structure of the Catalytic Domain of the Hepatitis C Virus NS2-3 Protease

I.C. Lorenz, J. Marcotrigiano, T.G. Dentzer, and C.M. Rice

The Rockefeller University, Laboratory of Virology and Infectious Disease

Hepatitis C virus (HCV) is an important human pathogen leading to cirrhosis and liver cancer. The viral RNA genome encodes a polyprotein that is processed into 10 distinct proteins by action of host cellular and viral proteases. Recently, we have determined the crystal structure of the catalytic domain of the HCV NS2-3 protease, which mediates one cleavage reaction in the viral polyprotein essential for viral replication. NS2 contains a dimeric cysteine protease with a novel fold. Interestingly, the dimer contains a pair of composite active sites, with both monomers contributing residues to each active site. This unusual feature may enable the virus to regulate proteolytic processing and thus the onset of RNA replication. Moreover, the structure may serve as a basis for the development of new antiviral therapies.

An estimated 120 million people are infected worldwide with HCV. Chronic infection is common and causes severe liver damage and hepatocellular carcinoma. A vaccine has not yet been developed, and only 55-60% of the patients respond to the currently available therapies. Therefore, approaches to identify novel drug targets are sorely needed.

The single-stranded, positive-sense RNA genome contains one open reading frame, which codes for ten viral proteins. Three proteins are structural components of the virus particle, whereas the remainder is involved in viral replication and host interactions. Synthesis of the HCV proteins occurs by translation of the viral genome into a polyprotein precursor, which is processed into individual proteins by two host cellular and two viral proteases (**Figure 1**). One of them, the HCV NS2-3 protease, mediates cleavage of the viral polyprotein at the junction between non-structural proteins (NS) 2 and 3. This step is required for replication of the viral RNA both *in vivo* and *in vitro*.

We have recently determined the crystal structure of the catalytic domain of the NS2-3 protease, which spans the carboxy-terminal half of NS2 ($NS2^{pro}$, residues 94-217). The functional unit of $NS2^{pro}$ appears to be a dimer, with each monomer consisting of an amino-terminal alpha-helical subdomain and a carboxy-terminal subdomain forming an antiparallel beta sheet (**Figure 2a and b**). The two subdomains are connected by an extended linker, resulting in an exchange of the carboxy-terminal subdomains.

Early mutagenesis experiments led to the identification of a putative catalytic triad consisting of amino acid residues histidine 143, glutamate 163, and cysteine 184. In the crystal structure, these residues form an active site with a geometry similar to those of other viral and cellular cysteine proteases. Surprisingly, each active site consists of residues from both monomers: histidine 143 and glutamate 163 are contributed by one monomer, whereas the nucleophilic cysteine 184 originates from the other chain (**Figure 3a and b**). The dimeric form of the protease suggests a mechanism for regulated polyprotein processing and viral RNA replication.

Authors (from left to right) Joe Marcotrigiano, Charlie Rice, lab mascot Sadie, Thomas Dentzer, and Ivo Lorenz

The $NS2^{pro}$ structure corresponds to the post-

cleavage form of the protease. The carboxy-terminal leucine 217 remains coordinated in the active site after cleavage, forming hydrogen bonds with the adjacent atoms of the catalytic cysteine and histidine residues (**Figure 3b**). Binding of leucine 217 to the active site has two implications: (I) the protease becomes inaccessible for other substrates, and (II) NS2 is 'locked' as a dimer, which may have other functions in the viral life cycle after proteolytic processing.

To demonstrate that NS2 can form dimers with composite active sites *in vivo*, we used two mutant NS2-3 polypeptides, either containing a histidine 143 to alanine or a cysteine 184 to alanine point mutation in the NS2 active site. Each of these NS2-3 variants expressed individually cannot undergo cleavage at the NS2/3 junction. However, if a composite active site can form, then mixing of the two NS2-3 mutants should lead to the reconstitution of a functional active site, resulting in partial proteolytic processing. This was indeed the case when these mutants were analyzed in a series of experiments in tissue culture. Thus, we were able to demonstrate the *in vivo* relevance of the mechanism we proposed based on the crystal structure.

Proteolysis through formation of a composite active site has never been observed in a cysteine or serine protease before. However, these features are reminiscent of human immunodeficiency virus (HIV), which encodes a dimeric aspartic protease with a single active site at the dimer interface. Thus, HCV and HIV may have evolved similar strategies to control the timing of events during their viral life cycles.

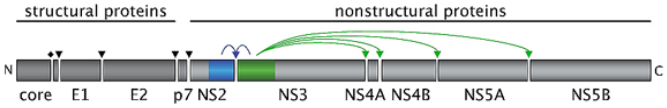

Figure 1. *The hepatitis C virus polyprotein. Schematic representation of the HCV polyprotein containing the structural proteins (core, envelope proteins E1 and E2), a small hydrophobic protein (p7), and the nonstructural (NS) proteins (NS2 to NS5B). Cleavages in the structural region and at the amino-terminus of NS2 occur by action of the host signal peptidase (arrowheads) and signal peptide peptidase (diamond). The NS2-3 protease, which consists of residues 94-217 of NS2 (blue) and residues 1-181 of NS3 (green), cleaves at the NS2/NS3 junction (blue arrow). All cleavages downstream of NS3 are mediated by the NS3-4A protease (green arrows). N, amino-terminus; C, carboxy-terminus.*

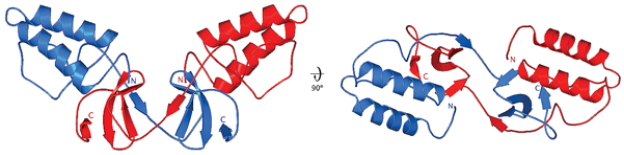

Figure 2. *Structure of the NS2 protease domain.* ***a****, Ribbon diagram showing the structure of the NS2^{pro} dimer, with one monomer in blue, the other in red.* ***b****, Ribbon diagram of the NS2^{pro} dimer rotated 90º around the horizontal axis in* ***a****. The amino- and carboxy-termini are labeled.*

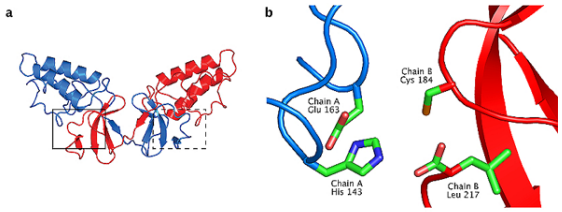

Figure 3. *The active site of NS2.* ***a****, Location of the two active sites in the NS2^{pro} dimer, shown within the boxed regions.* ***b****, Close-up view of the NS2^{pro} active site in the solid-lined box in* ***a****. The amino acid residues His 143, Glu 163, Cys 184, and Leu 217 are shown as ball-and-stick drawings. The active site is composed of His 143 and Glu 163 from one molecule of the dimer (chain A, drawn in blue), and Cys 184 from the other molecule (chain B, drawn in red). The C-terminal residue, Leu 217, originates from the same chain as Cys 184.*

Tiny Tubes and Rods Show Promise as Catalysts, Sunscreen

New ways to make, modify titanium oxide nanostructures for industrial, medical uses

Scientists at Brookhaven have developed new ways to make or modify nanorods and nanotubes of titanium oxide, a material used in a variety of industrial and medical applications. The methods and new titanium oxide materials may lead to improved catalysts for hydrogen production, more efficient solar cells, and more protective sunscreens. The research is published in two papers, one in *Advanced Materials* (published online August 22, 2007), and the other in the *Journal of Physical Chemistry* (online September 8, 2007).

In the first study, the scientists enhanced the ability of titanium oxide to absorb light.

"Titanium dioxide's ability to absorb light is one the main reasons it is so useful in industrial and medical applications," said Wei-Qiang Han, a scientist at Brookhaven's Center for Functional Nanomaterials (CFN) and lead author on both papers.

It is used as a photocatalyst for converting sunlight to electricity in solar cells and also has applications in the production of hydrogen, in gas sensors, in batteries, and in using sunlight to degrade some environmental contaminants. It is also a common ingredient in sunscreen.

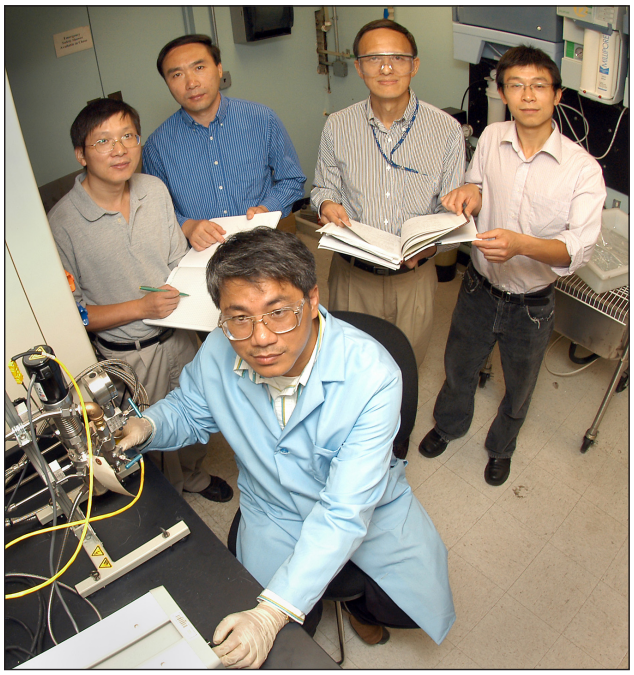

Authors, (sitting) Wei-Qiang Han, (standing, from left) Lijun Wu, Zhenxian Liu, Yimei Zhu, and Wen Wen

Many scientists have explored ways to improve the light-absorbing capability of titanium oxide, for example, by "doping" the material with added metals. Han and his coworkers took a new approach. They enhanced the material's light-absorption capability by simply introducing nanocavities, completely enclosed pockets measuring billionths of a meter within the 100-nanometer-diameter solid titanium oxide rods.

The resulting nanocavity-filled titanium oxide nanorods were 25 percent more efficient at absorbing certain wavelengths of ultraviolet A (UVA) and ultraviolet B (UVB) solar radiation than titanium oxide without nanocavities.

"Our research demonstrates that titanium oxide nanorods with nanocavities can dramatically improve the absorption of UVA and UVB solar radiation, and thus are ideal new materials for sunscreen," Han said.

The cavity-filled nanorods could also improve the efficiency of photovoltaic solar cells and be used as catalysts for splitting water and also in the water-gas-shift reaction to produce pure hydrogen gas from carbon monoxide and water.

The method for making the cavity-filled rods is simple, says Han. "We simply heat titanate nanorods in air. This process evaporates water, transforming titanate to titanium oxide, leaving very densely spaced, regular, polyhedral nanoholes inside the titanium oxide."

In the second paper, Han and his collaborators describe a new synthesis method to make iron-doped titanate nanotubes, hollow tubes measuring approximately 10 nanometers in diameter and up to one micrometer (one millionth of a meter) long. These experiments were also aimed at improving the material's photoreactivity. The scientists demonstrated that the resulting nanotubes exhibited noticeable reactivity in the water-gas-shift reaction.

"Although the activity of the iron-doped nanotubes was not as good as that of titanium oxide loaded with metals such as platinum and palladium, the activity we observed is still remarkable considering that iron is a much less expensive metal and its concentration in our samples was less than one percent," Han said.

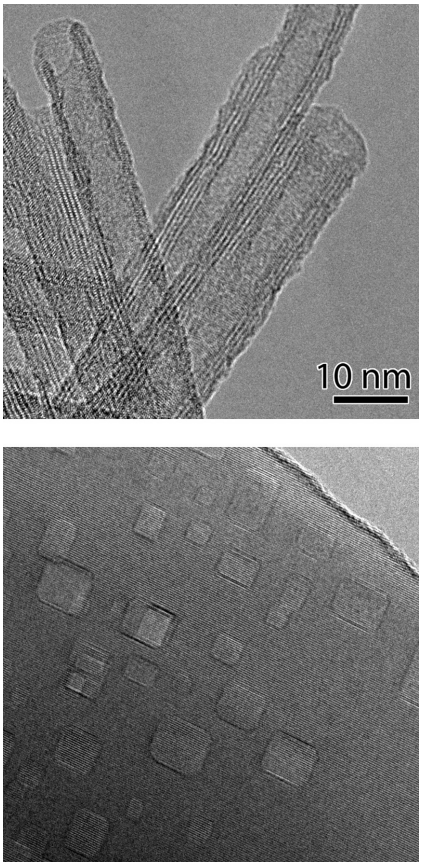

Transmission electron micrographs of nanocavity-filled titanium oxide nanorods (bottom) and iron-doped titanate nanotubes (top). Both are being investigated as photocatalysts for reactions to produce hydrogen gas. The improved light-absorption of the nanocavity-filled nanorods also makes them ideal new materials for sunscreen.

The scientists also observed interesting magnetic properties in the iron-doped nanotubes, and will follow up with future studies aimed at understanding this phenomenon.

Materials developed in these studies were analyzed using several of Brookhaven Lab's unique tools and methods for the characterization of nanostructures, including transmission electron microscopy and various x-ray and infrared techniques at NSLS beamlines X7B and U2A.

This research, which has clear connections to improved energy technologies, was funded by the Office of Basic Energy Sciences within the U.S. Department of Energy's Office of Science.

Collaborators on the *Advanced Materials* paper include Lijun Wu, Robert F. Klie, and Yimei Zhu, all of Brookhaven's CFN. For the *Journal of Physical Chemistry* paper, collaborators include Brookhaven chemists Wen Wen and Jonathan Hanson; Ding Yi, Mathew Maye, and Oleg Gang of the CFN; Zhenxian Liu of the Carnegie Institution of Washington; and Laura Lewis, formerly at the CFN and now at Northeastern University.

For more information, see: W.-Q. Han, L.J. Wu, R.F. Klie, and Y.M. Zhu, "Enhanced Optical Absorption Induced by Dense Nanocavities inside Titania Nanorods," Advanced Materials, ***19****, 2525-2529 (2007).*

W.-Q. Han, W. Wen, D. Yi, Z. Liu, M. Maye, L. Lewis, J. Hanson, and O. Gang, "Fe-Doped Trititanate Nanotubes: Formation, Optical and Magnetic Properties, and Catalytic Applications," J. Phys. Chem. C., ***111****, 14339-14342 (2007).*

— Karen McNulty Walsh

BEAMLINE
X27C

PUBLICATIONS
B.N. Wang, R.D. Bennett, E. Verploegen, A.J. Hart, and R.E. Cohen "Quantitative Characterization of the Morphology of Multiwall Carbon Nanotube Films by Small-Angle X-ray Scattering," *J. Phys. Chem. C,* **111**, 5889 (2007).

FUNDING
MIT's Institute for Soldier Nanotechnologies; Fannie and John Hertz Foundation; DURINT on Microstructure, Processing and Mechanical Performance of Polymer Nanocomposites

FOR MORE INFORMATION
Eric Verploegen, Department of Materials Science and Engineering, Massachusetts Institute of Technology
ericv@mit.edu

Quantitative Characterization of the Morphology of Multiwall Carbon Nanotube Films by Small-Angle X-ray Scattering

E. Verploegen[1], B. Wang[2], R. Bennett[2], A.J. Hart[3], and R.E. Cohen[2]

[1]Departments of Materials Science and Engineering, [2]Chemical Engineering, and [3]Mechanical Engineering, Massachusetts Institute of Technology

Films of multiwall carbon nanotubes (MWCNTs) grown by thermal chemical vapor deposition were studied using small-angle x-ray scattering (SAXS). We assessed the extent of alignment of carbon nanotubes (CNTs) by examining relative SAXS intensities as a function of azimuthal angle. We also identified features in the SAXS patterns that correspond well to CNT diameters measured through high-resolution transmission electron microscopy. We determined that the alignment of CNTs as well as their average diameter can vary significantly throughout the film. This demonstrates the utility of SAXS for quantitative structural analysis of CNT films, indicating the potential to reveal new information about the CNT growth process, and relating variations in morphology to evolution of the catalyst and reaction conditions.

We have that shown small-angle x-ray scattering (SAXS) is a powerful tool for investigating the morphologies of multiwall carbon nanotube (MWCNT) films. CNT films have attracted significant interest from the engineering community because of their remarkable thermal, electrical, and mechanical properties, and because they show promise for use in nanoelectronics, energy-absorbing foams, superhydrophobic films, and power applications. MWCNT films can be grown by thermal chemical vapor deposition, resulting in films that range from vertically aligned to entangled and tortuous.

The extent of CNT alignment can only be assessed qualitatively using scanning electron microscopy, but we have shown that it can be characterized quantitatively in various regions of the CNT film by examining the relative SAXS intensities as a function of azimuthal angle. Additionally, by fitting the SAXS data to a model for cylindrical form factor, the average CNT diameter, and an estimate of the standard deviation, can be determined. The diameters determined through SAXS correspond well to high-resolution transmission electron microscopy (HRTEM) data. SAXS provides the advantage of sampling millions of CNTs in a single image, and also provides spatial resolution not accessible through HRTEM. The ability to characterize the CNTs as a function of position within the film allowed us to observe a systematic increase in the diameter as a function of height from the substrate as well as smaller diameter CNTs near the edge, relative to the center of the film. Systematic studies of the morphologies of the CNT forests as a function of variations in the growth conditions are underway and will provide insights into the fundamental mechanisms of the CNT growth process. Developing a complete understanding of this process is critical for enabling materials' structures and properties to be optimized and customized for specific applications.

Eric Verploegen

We have also investigated the effects of mechanical manipulations upon the morphologies of these MWCNT forests, including uniaxially compression and densification through solvent evaporation. A low-angle scattering feature in the data, corresponding to the interparticle structure factor, allows us to extract information about the packing density of the CNTs. We have recently performed USAXS measurements that confirm this result and additionally reveal the presence of CNT aggregates in these films. This analysis allows

for determination of the average spacing between the CNTs, which varies significantly with mechanical manipulation.

SAXS provides rich morphological information that is not accessible through conventional microscopy techniques. This type of analysis can easily be applied to single-wall CNTs, zinc oxide nanowires, and a variety of other similar systems.

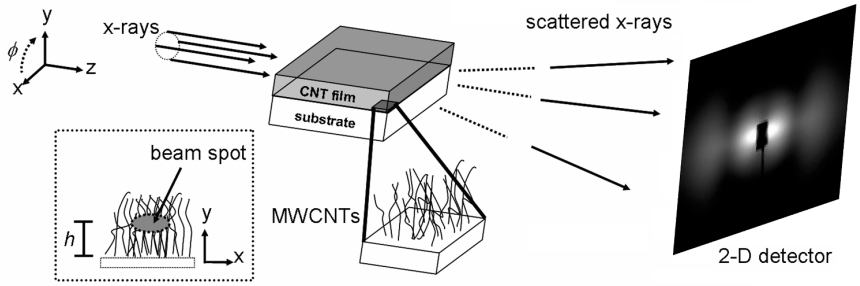

Figure 1. *Schematic of the experimental setup for small-angle x-ray scattering of multiwall carbon nanotube forests. A motorized stage provides spatial resolution allowing for the morphology to be investigated as a function of position within the film.*

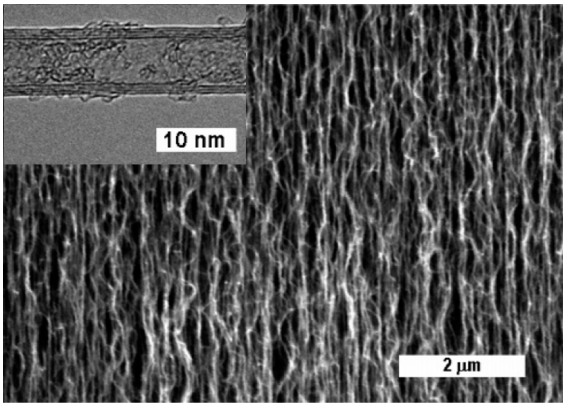

Figure 2*. Scanning electron microscopy (SEM) image of a vertically aligned multiwall carbon nanotube forest. Inset: transmission electron microscopy image of a single multiwall carbon nanotube. Small angle x-ray scattering (SAXS) provides quantitative characterization of the alignment, where only qualitative assessments of orientation can be made with SEM. SAXS measurements yield a "locally averaged" measurement of the CNT diameter, where TEM requires imaging of individual nanotubes.*

BEAMLINE
U7A

PUBLICATION
L.R. Pattison, A. Hexemer, E.J. Kramer, S. Krishnan, P.M. Petroff, and D.A. Fischer, "Probing the Ordering of Semiconducting Fluorene-Thiophene Copolymer Surfaces on Rubbed Polyimide Substrates by Near-Edge X-ray Absorption Fine Structure," *Macromolecules*, **39**(6), 2225-2231, (2006).

FUNDING
Microelectronics Advanced Research Corporation
National Science Foundation
Office of Naval Research

FOR MORE INFORMATION
Edward J. Kramer, Department of Materials and Department of Chemical Engineering, University of California Santa Barbara
edkramer@mrl.ucsb.edu

Probing the Ordering of Semiconducting Fluorene-Thiophene Copolymer Surfaces on Rubbed Polyimide Substrates by Near-Edge X-ray Absorption Fine Structure

L.R. Pattison[1*], A. Hexemer[1], E.J. Kramer[1,2**], S. Krishnan[5] P.M. Petroff[1,3], D.A. Fischer[4]

[1]Department of Materials, University of California Santa Barbara; [2]Department of Chemical Engineering, University of California Santa Barbara, [3]Department of Electrical Engineering, University of California Santa Barbara; [4]National Institute of Standards and Technology; [5]Department of Materials Science and Engineering, Cornell University

The temperature-dependent alignment of semiconducting liquid crystalline (LC) fluorene-thiophene copolymer (F8T2) thin film surfaces on rubbed polyimide underlayers was investigated using the near-edge x-ray absorption fine structure (NEXAFS) technique. The NEXAFS data show that: a) in thin F8T2 films at all temperatures, the stiff polymer molecular axis lies in the plane of the substrate but the plane of conjugation of the F8T2 molecules is rotated randomly with respect to the surface normal, and b) after annealing in the LC phase the molecular axis is aligned with the rubbing direction of the rubbed polyimide alignment underlayer throughout the entire F8T2 film.

Conjugated organic polymers are increasingly being developed as functional materials for various devices including organic thin film transistors (OTFTs), photovoltaics, and organic light emitting diodes (OLEDs). Higher carrier mobilities and polarized photon emission are usually obtained when the conjugated polymer films are macroscopically ordered. Poly(9,9-dioctylfluorene-*co*-bithiophene) alternating copolymer (F8T2) has several characteristics that make it convenient for studying electrical characteristics of aligned polymer films: conjugated segments for charge transport, relatively good stability in air, and solubility in a wide range of solvents. It also exhibits a thermotropic liquid crystal LC phase.

Polarized UV-vis spectroscopy and polarized light microscopy showed that F8T2 thin films deposited on rubbed polyimide alignment layers can be macroscopically aligned when annealed in the nematic phase. The polymer chain alignment and charge carrier mobility for the F8T2 molecules presented in this study are strongly correlated. We found that when polymer chains were aligned parallel to the transistor channel length, the field-effect mobility values are 2-3 times greater than mobility for as-deposited (amorphous) films, and 4-6 times greater than values obtained for devices with channel lengths perpendicular to polymer chain alignment.

Strong optical evidence of bulk polymer alignment on rubbed polyimide alignment layers exists, yet we do not know whether this alignment persists throughout the film to the surface. For certain device architectures in OTFTs, photovoltaics, and OLEDs, the alignment of the top surface will play a large role in the device performance. For instance, in OLEDs and photovoltaics, the F8T2 alignment affects charge injection and separation at the interfaces, and for non-inverted transistor structures, the top surface of the semiconductor is crucial to the carrier

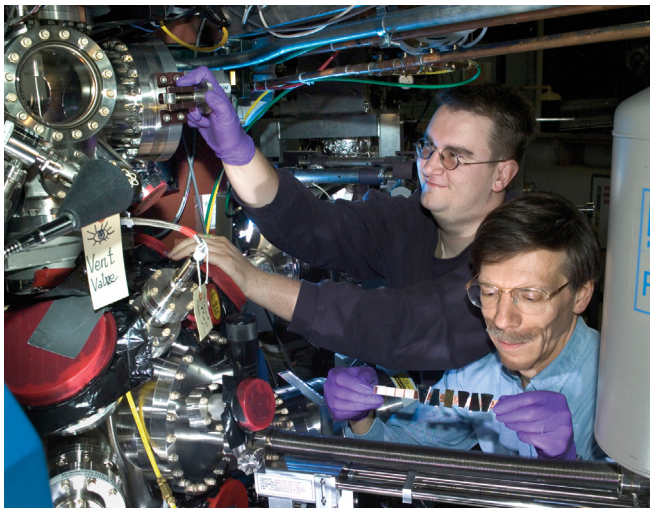

Authors (from left) Alex Hexemer and Daniel Fischer

mobility, since this is the region of current flow in the transistor operation.

In this work, we look at the reorientation of fluorene-thiophene copolymer induced by deposition on a rubbed polyimide alignment layer after various thermal treatments. We use NEXAFS to determine the molecular orientation at the surface, observing the strong alignment of the F8T2 main-chain axis to the rubbing direction, and the temperature stability of these results.

The carbon K-edge NEXAFS spectra were recorded at angles θ=90°, 80°, 70°, 60°, 55°, 40°, 30°, and 20°, where θ is the angle between the electric field vector (E) of the polarized soft x-rays and the sample normal as well as the angle between the incident photon beam and the sample surface. Rubbing the polyimide aligns the surface molecules along the rubbing direction (RD), creating an asymmetry in the molecular bonds at the surface. The unidirectional molecular alignment at the surface of the rubbed polyimide provides a template for the F8T2 orientation when heated to the mesophase. The NEXAFS spectra were recorded for two orientations of RD with respect to the plane of rotation E, parallel, where RD is always in the plane, and perpendicular, where RD is always normal to E.

In **Figure 1(a,b)**, we show the C K-edge NEXAFS partial electron yield (PEY) signal as a function of soft x-ray photon energy. The peak with strongest intensity at 284.4eV is the result of the transitions of electrons from the C1s to π^* orbitals of the conjugated C=C segments in the aromatic fluorene and thiophene rings. The transition dipole moment (TDM) of π^* orbitals is normal to the plane of conjugation. The NEXAFS PEY intensity at 20, 55, and 90° differed for the C=C 1s to π^* resonance at 284.4eV.

At 90° RD is parallel to the E of the incident soft x-ray radiation (parallel configuration). In this case, absorption is low because the electric field vector lies along the main-chain axis, whereas the TDM of π^* orbitals are perpendicular to this axis. As expected, there is stronger absorption at a 20° angle of incidence, where a large component of E is out of plane, and the NEXAFS signal decreases with increasing angle. In the case of perpendicular geometry, the angular dependence provides information as to the orientation of the aromatic rings about molecular chain axis, i.e. are the rings in the plane of the substrate, normal to the surface or rotated at random? In this configuration, the sample is being rotated about the main-chain axis with respect to the electric field vector of the incident soft x-ray radiation. Absorption occurs when the TDMs of the π^* orbitals are parallel to the E of the incident light. In Figure 2b, we see that the 20°, 55°, and 90° C1s to π^* resonances overlap. This indicates that the orientation of the aromatic rings at the surface is nearly random.

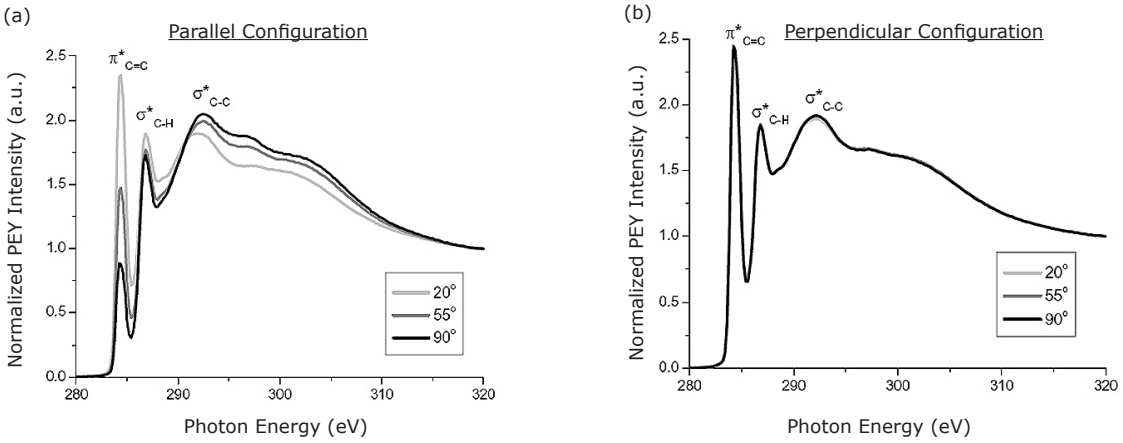

Figure 1. *Partial electron yield data for F8T2 thin film sample that was annealed at a temperature of 280°C, then quenched to room temperature. Scans taken at room temperature at θ = 20°, 55°, and 90° incidence in the parallel (a) and perpendicular (b) geometries. The strong overlap of curves in (b) makes it difficult to distinguish between the three scans.*

BEAMLINE
U5UA

PUBLICATION
J.I. Flege, E. Vescovo, G. Nintzel, L.H. Lewis, S. Hulbert, and P. Sutter, "A New Soft X-ray Photoemission Microscopy Beamline at the National Synchrotron Light Source," *Nucl. Instrum. Meth. in Phys. Res. B,* **261**, 855 (2007).

FUNDING
U.S. Department of Energy

FOR MORE INFORMATION
Jan Ingo Flege or Peter Sutter
Center for Functional Nanomaterials
Brookhaven National Laboratory
jiflege@bnl.gov
psutter@bnl.gov

Spectroscopic Imaging of Heterogeneous Nanomaterials – X-Ray Photoemission Microscopy at the NSLS

J.I. Flege[1], E. Vescovo[2], G. Nintzel[2], S. Hulbert[2], and P. Sutter[1]

[1]Center for Functional Nanomaterials, Brookhaven National Laboratory; [2]National Synchrotron Light Source, Brookhaven National Laboratory

We report the present status of a newly installed low-energy electron microscopy and photoelectron microscopy end station at NSLS beamline U5UA. In the first test experiments on sub-monolayer Au coverages deposited on Ru(0001), we demonstrate core-level and valence band photoelectron imaging with a lateral resolution of about 65 nm at a field of view of 10 μm. In contrast to other installations for photoelectron microscopy, the new NSLS end station uses illumination under normal incidence, maximizing the photon flux and enhancing the sensitivity for future in-plane characterization of magnetic materials.

Low-energy electron microscopy (LEEM) has contributed considerably to the understanding of dynamic surface processes such as adsorption, thin film growth, or chemical reactions under ultra-high vacuum conditions. The contrast observed in LEEM arises from local changes in atomic surface structure, resulting in pronounced modulations of the local reflectivity for electrons impinging on the sample with kinetic energies of typically a few electron volts. In general, these variations may reflect atomic steps, co-existing surface phases, or chemical inhomogeneities. While the biggest advantages of LEEM are its *in-situ*, video-rate imaging capability of sample areas of about 2-50 μm in diameter with a lateral resolution better than 10 nm and high surface sensitivity, this technique only probes surface structure and does not generally provide element or chemical specificity. If combined with an energy filter and a tunable photon source of sufficient flux and brilliance, however, the low-energy electron microscope may also be used for *spectroscopic imaging*, i.e., for laterally resolved element-sensitive surface mapping known as x-ray photoemission electron microscopy (XPEEM) (see **Figure 1**). Here, we illustrate the capabilities of our new setup at NSLS beamline U5UA, consisting of a recently installed Elmitec LEEM III instrument with an imaging energy analyzer, by discussing first experimental results on the model system Au/Ru(0001).

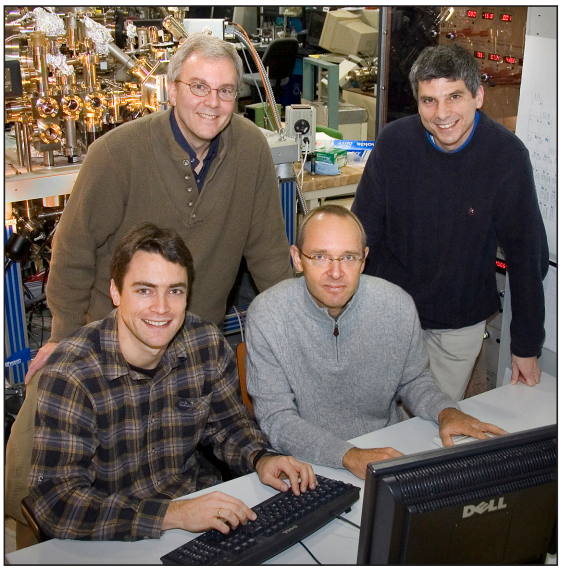

Authors (from left) Jan Ingo Flege, Steve Hulbert, Peter Sutter, and Elio Vescovo

Au/Ru(0001) was chosen as a model system for initial LEEM/XPEEM imaging because it constitutes a heteroepitaxial system in which the film nearly perfectly wets the substrate, and in which there is negligible intermixing between film and substrate materials. Hence, sharply delineated two-dimensional (2D) Au islands on Ru can be grown at submonolayer coverage, providing an ideal test structure for element-specific surface imaging. In **Figure 2**, bright-field LEEM micrographs are displayed that show the evolution of the surface morphology upon Au deposition onto a Ru(0001) single crystal. Starting from the clean surface on which only atomic steps and step bunches are visible as dark bands **(Figure 2a)**, the heterogeneous nucleation of Au

islands (dark patches) is observed, which starts at the lower side of the substrate step edges **(Figure 2b)**. Upon further deposition, dendritic 2D island growth by Au adatom capture, i.e. adsorption of Au atoms and subsequent diffusion to the edges of the growing islands, and the nucleation of additional islands at substrate steps are competing processes. Finally, the growth is stopped at about a half-monolayer Au coverage **(Figure 2c)** to obtain a patterned surface for the photoemission electron microscopy (PEEM) experiments.

In the following, we will provide examples for three different modes of photoemission microscopy based on the kinetic energy of the detected electrons: In PEEM, the slow inelastically scattered electrons, which exhibit kinetic energies close to 0 eV, are employed, generally providing chemical image contrast due to local work function variations at high overall intensity. Such an image is shown in **Figure 3a**, in which the Au-covered regions appear dark due to an increase of the work function as compared to the clean Ru surface.

In contrast, XPEEM makes use of photoelectrons that can be attributed to specific atomic core-levels, thereby providing direct access to the spatial distribution of the corresponding elements or chemical states. This elemental or chemical specificity is demonstrated in **Figure 3b**, which shows an image that has been acquired using Au $4f_{7/2}$ core-level photoelectrons. This can be interpreted as an intensity map of the elemental Au distribution, thus confirming the previous identification of monolayer gold islands.

Finally, a different type of contrast may be achieved in valence band photoelectron emission microscopy (VPEEM) when the electron energy analyzer is tuned onto distinct features about 4.5 eV below the Fermi level in the valence band structure of the sample **(Figure 3c)**. Since all bright regions in this image also show up bright in Figure 3(b), this electronic state can be localized at the Au atoms. Hence, if the lateral element distribution is already known, e.g. as a result of preceding XPEEM investigations, then it is possible to identify contributions to the electronic structure from VPEEM micrographs.

Future research will comprise in-situ studies of oxidation and catalysis on transition metals, growth of organic thin-film semiconductors, and characterization of magnetic materials.

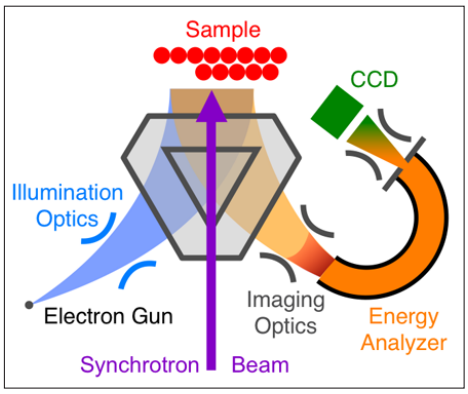

Figure 1. *Schematic of the LEEM/PEEM setup at beamline U5UA.*

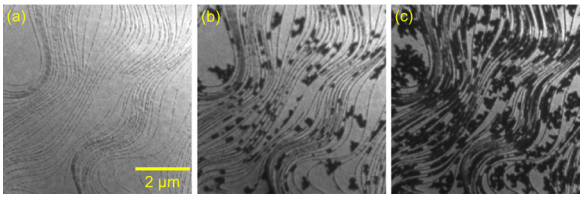

Figure 2. *LEEM image sequence (E = 6.5 eV) acquired during Au evaporation onto Ru(0001). (a) Clean Ru(0001) surface. Only step edges are visible. (b) and (c) Nucleation and 2D fractal growth of Au islands (dark) at the substrate step edges.*

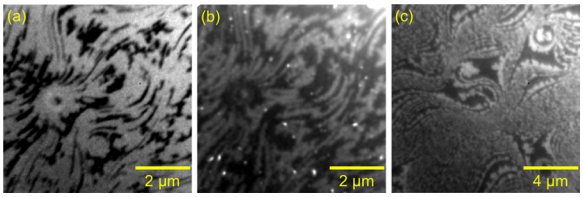

Figure 3. *(a) PEEM image obtained with secondary electrons. (b) XPEEM image obtained with Au $4f_{7/2}$ core-level photoelectrons. The bright spots are artifacts from the CCD camera. (c) XPEEM image obtained with valence band photoelectrons.*

BEAMLINE
U7A

PUBLICATION
V.M. Prabhu, S. Sambasivan, D. Fischer, L.K. Sundberg, and R.D. Allen, "Quantitative Depth Profiling of Photoacid Generators in Photoresist Materials by Near-edge X-ray Absorption Fine Structure Spectroscopy," *Appl. Surf. Sci.*, ***253*** (2), 1010-1014 (2006).

FUNDING
National Institute of Standards and Technology

FOR MORE INFORMATION
Vivek M. Prabhu, Polymers Division, National Institute of Standards and Technology
vprabhu@nist.gov

Quantitative Depth Profiling of Photoacid Generator Molecules in Photoresist Materials by Near-Edge X-ray Absorption Fine Structure Spectroscopy

V.M. Prabhu[1], S. Sambasivan[1], D. Fischer[2], L.K. Sundberg[3], and R.D. Allen[3]

[1]Polymers Division, National Institute of Standards and Technology; [2]Ceramics Division, National Institute of Standards and Technology; [3]IBM Almaden Research Center

Near-edge x-ray absorption fine structure (NEXAFS) spectroscopy was used to quantify the surface composition and depth profiling of photoacid generators in thin film photoresist materials. By considering model compositional profiles, NEXAFS distinguishes the surface molar excess within the top 6 nm from the bulk. A surface enriched system, triphenylsulfonium perfluorooctanesulfonate (TPS-PFOS), is contrasted with a perfluorobutanesulfonate (TPS-PFBS) photoacid generator, which displays an appreciable surface profile within a 6 nm segregation length scale. These results, while applied to 193-nm photoresist materials, highlight a general approach to quantifying NEXAFS partial electron yield data and find application to immersion lithography fundamentals.

Vivek Prabhu

Robert Allen

Linda Sundberg

Sharadha Sambasivan and Daniel Fischer

Chemically amplified photoresist materials are the enabling technology for photolithography –the process by which all modern microelectronics are manufactured by the semiconductor industry. These multi-component materials are comprised primarily of polymeric photoresist, photoacid generators, and base-quencher additives. The exposure of the photoresist to radiation through a mask leads to the generation of photoacids that catalyze a chemical reaction rendering exposed areas soluble in a developer. Perturbations in the component distributions therefore are critical to print sub-65 nm features by 193 nm photolithography. The industry is ready to extend this technology to 32 nm half-pitch dimensions by immersion lithography, which increases the resolution by applying a high refractive index fluid between the lens and resist thin film to reduce the effective wavelength of light. This process change leads to additional demands and constraints on the photoresist material.

Any change in surface structure or chemistry from the top few nanometers due to leaching of photoacid generator and base additives during immersion can compromise the performance of the resist as well as contaminate the lens system. Near-edge x-ray absorption fine structure (NEXAFS) spectroscopy provides a sensitive bond-selective and depth-selective method to quantify the thin film surface structure. In a NEXAFS experiment, tunable soft x-rays are preferentially absorbed by the sample when the incident radiation is at the appropriate energy to allow the excitation of a core shell electron of a specific element (C, N, O, or F) to a chemical bond specific unoccupied molecular orbital. Due to the well-defined energy gap associated with a core shell to unoccupied orbital transition, NEXAFS is sensitive to the bond-

ing characteristics of the element giving a discrete peak(s) for each chemical bond. Electrons originating from near the top (1 nm to 6 nm for carbon *K*-edge electron yield spectra) of the film surface will have different final kinetic energies upon detection, depending on their inelastic energy loss (depth of creation). By applying a negative voltage entrance grid bias at the partial electron yield detector, electrons of low kinetic energy can be rejected. As the negative entrance grid bias voltage is gradually increased, lower kinetic energy electrons are discriminated and the effective electron yield sampling depth gets closer to the film surface.

Figure 1 shows the NEXAFS carbon *K*-edge spectra for the pure methacrylate photoresist (dotted line) and photoresist containing TPS-PFOS (solid lines) shown in **Figure 2**. The incident photon energy is scanned from 280 eV to 330 eV and the electron yield is measured at the detector as a function of the entrance grid bias from -250 V (immediate surface) to -50 V (top several nm). The sharp peak at 285 eV is the C 1s $\rightarrow \pi^*_{C=C}$ transition arising from the triphenyl groups on the photoacid generator as highlighted in the inset. This region is of specific interest for depth profiling as seen from the strong bias dependence for the resist/photoacid generator mixture. The integrated peak intensity is directly proportional to the C=C molar bond (number) density allowing a quantification of the PAG composition as a function of depth without interference of the photoresist chemistry.

The measurement method is described in the *Applied Surface Science* article as well as approaches to quantify the photoacid generator depth profile over the top 2 nm to 6 nm. This method can be extended to a diverse set of materials systems without the need for special labeling or preparatory procedures.

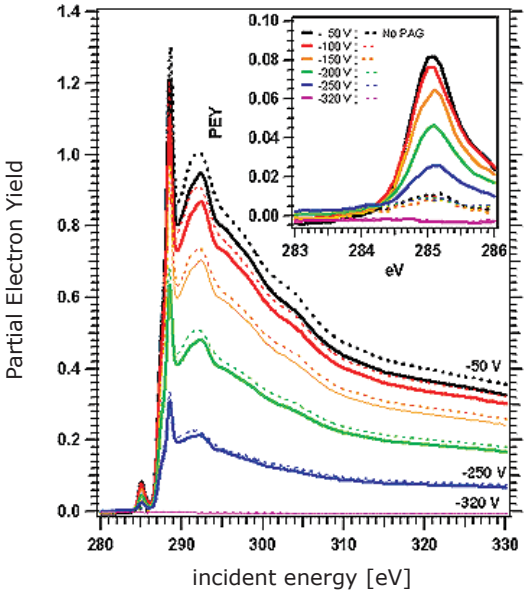

Figure 1. *NEXAFS spectra of the pure photoresist (dotted lines) and resist containing 6.7 % by mass TPS-PFOS photoacid generator (solid lines) as a function of entrance-grid bias from -50 V to -250 V. At -320 V, no signal is detected. The inset highlights the* $\pi^*_{C=C}$ *region which allows direct quantification of the triphenyl groups of the photoacid generator.*

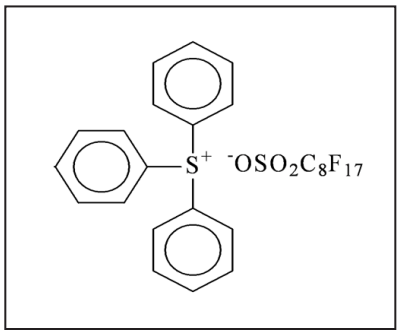

Figure 2. *Triphenysulfonium perfluorooctanesulfonate photoacid generator.*

BEAMLINE
X21

PUBLICATIONS
V. Kiryukhin, E.P. Bernard, V.V. Khmelenko, R.E. Boltnev, N.V. Krainyukova, and D.M. Lee, "Noble-Gas Nanoclusters with Fivefold Symmetry Stabilized in Superfluid Helium," *Phys. Rev. Lett.*, **98**, 195506 (2007).

FUNDING
NASA
National Science Foundation
U.S. Civilian Research & Development Foundation

FOR MORE INFORMATION
Valery Kiryukhin, Department of Physics and Astronomy, Rutgers University
vkir@physics.rutgers.edu

Platonic Solids on the Nanoscale

V. Kiryukhin[1], E.P. Bernard[2], V.V. Khmelenko[2], D.M. Lee[2], R.E. Boltnev[3], and N.V. Krainyukova[4]

[1]Rutgers University; [2]Cornell University; [3]Institute of Energy Problems of Chemical Physics, Russia; [4]Institute for Low Energy Physics and Engineering, Ukraine

Nanometer-scale chunks of matter (nanoclusters) often possess properties that are very different from those of the bulk crystals. Understanding the behavior of nanoscale-patterned materials is necessary for technological progress in many areas, including electronics, data storage, and catalysis. Using synchrotron diffraction, it was for the first time demonstrated that bulk amounts of highly symmetric icosahedral and decahedral noble-gas nanoclusters can be produced by injecting the noble-gas atoms into superfluid helium. These results open new opportunities for fundamental and applied research of various nanoscale systems in previously unavailable quantities and in new experimental environments.

Growth of any solid from the liquid or gas phase begins with formation of small particles. The properties of such nanometer-scale particles, the nanoclusters, can be dramatically different from their macroscopic counterparts. This is true even for the simplest possible solids – those made of noble-gas atoms, such as neon and argon. Noble gases crystallize in the so-called face-centered cubic structure (fcc). However, due to surface energy effects, noble-gas nanoclusters are predicted to exhibit a variety of exotic shapes. The smallest clusters are expected to be icosahedral, the larger ones – decahedral, and even larger clusters should exhibit the hexagonal close-packed (hcp) structure. Such highly symmetric shapes are not coincidental. They result from the general principle of energy minimization requiring the densest possible packing of the attractive structural units combined with the minimum possible surface area. In other words, simple principles give rise to simple shapes. It is not, therefore, surprising that some of the famous Platonic solids, such as icosahedra and dodecahedra, spontaneously appear in the world of nanoparticles. Because of the generality of the underlying principles, such shapes are observed not only in inorganic systems. Some viruses and even higher organisms possess the shape of the Platonic solids.

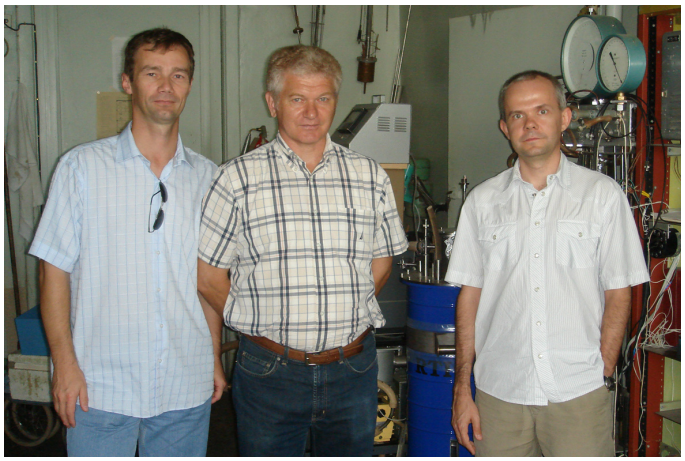

Authors (from left) R.E. Boltnev, V.V. Khmelenko, and V. Kiryukhin

Noble gases are important because of their simplicity: they are the best possible model systems to study. Noteworthy, even these simple systems are not understood completely. For example, the origin of the fcc structure in the bulk is currently unknown. It is, therefore, important to study noble-gas nanoclusters that are accessible to model calculations. For this, it is important to produce the clusters in bulk quantities. Until now, only minute quantities of icosahedral nanoclusters were produced in supersonic beams and on the surfaces. In this study, the nanoclusters were produced by injection of a helium jet with added noble-gas atoms into superfluid helium. As a result, bulk jelly-like samples were obtained. High-intensity x-ray beam from beamline X25, combined with the unique cryostat installed there, made it possible to determine the structure of these samples conclusively

for the first time. The samples were made of argon, krypton, and neon. They were found to consist of loose nanoclusters, 5-6 nanometer in diameter, suspended in liquid helium. Icosahedral and decahedral clusters were produced. Some of these results are shown in **Figure 1**. Importantly, bulk amounts of the nanoclusters were produced: the sample sizes exceeding 1 cm^3, and the atomic densities exceeding 10^{20} cm^{-3} were obtained. Thus, properties of the nanoclusters can now be studied with previously inaccessible techniques and in previously unattainable stable environments. Another key advantage of this technique is that the clusters can be made of a huge variety of materials, including technologically important magnetic materials, organic materials, water, and other important systems. These results open up numerous intriguing opportunities, and these studies are, therefore, only beginning.

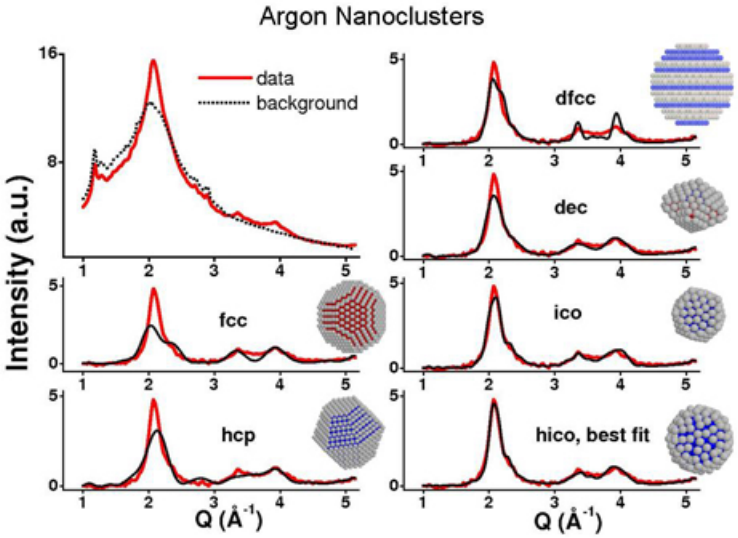

X-ray diffraction data (red lines) and model calculations (black lines) for argon nanoclusters. Various structural models, including face-centered cubic (fcc), hexagonal close-packed (hcp), fcc with stacking faults (dfcc), decahedra (dec), icosahedra (ico), and icosahedra covered with one hexagonal overlayer (hico) are shown. The hico particles clearly describe the experimental data best for this sample.

BEAMLINE
X21

PUBLICATION
A. Ozcan, Y. Wang, G. Ozaydin, K. Ludwig, A. Bhattacharyya, T. Moustakas, and D. Siddons, "Real-Time X-ray Studies of Gallium Adsorption and Desorption, " *J. Appl. Phys.*, **100**, 084307 (2006).

FUNDING
National Science Foundation
U.S. Department of Energy

FOR MORE INFORMATION
Karl Ludwig, Physics Department, Boston University
ludwig@buphy.bu.edu

Real-Time X-Ray Studies of Gallium Adsorption and Desorption

A.Ozcan[1*], Y. Wang[1], G. Ozaydin[1,2], K. Ludwig[1], A. Bhattacharyya[3], T. Moustakas[3], and D. Siddons[4]

[1]Physics Department, [2]Aerospace and Mechanical Engineering Department, and [3]Department of Electrical and Computer Engineering, Boston University; [4]National Synchrotron Light Source, Brookhaven National Laboratory; *Currently at IBM Microelectronics, Fishkill, NY

Real-time grazing-incidence small-angle x-ray scattering has been employed to study the adsorption and desorption of Ga on c-plane sapphire and Ga-polar GaN surfaces. Formation of liquid Ga nano-droplets has been observed on sapphire during Ga exposure from an effusion cell at high flux. Following the Ga deposition, the nano-droplets were nitridated in situ by a nitrogen plasma source, which converted the droplets into GaN nanodots. In addition to the droplet studies, at lower Ga flux the adsorption and desorption of Ga has been studied in the pre-droplet regime. Significantly different Ga adsorption/desorption rates were observed on sapphire and GaN surfaces.

Wide-bandgap III-V nitrides (e.g. GaN) have important applications in optoelectronics and high-power devices. During the growth of these materials by molecular beam epitaxy (MBE) the best films are grown in a Ga-rich environment; it is believed that the excess Ga forms a wetting layer on the surface that promotes lateral diffusion of atoms arriving at the growing surface. Thus, it is important to understand the kinetics and behavior of Ga adsorption and desorption on sapphire substrates and GaN films. We have recently used the NSLS for the real-time study of surface- and thin-film processes on beamline X21 to investigate these issues.

Figure 1 shows the real-time grazing-incidence small-angle x-ray scattering (GISAXS) evolution during Ga adsorption onto c-plane sapphire at 700 °C. Initially, the scattering profile shows only the intensity of the near-specular reflection from the sample surface. At approximately t = 15 s, the Ga shutter was opened and, as Ga exposure continues, the broad diffuse scattering background evolves into symmetric peaks centered on approximately $|q_{//}| = 0.12$ nm^{-1}. These peaks indicate the formation of laterally correlated Ga droplets with an average real-space separation of approximately 50 nm.

Absorption and desorption rates on sapphire substrates were examined systematically as a function of Ga deposition rate and substrate temperature by monitoring the Ga K-edge fluorescence, which is proportional to the number of Ga atoms on the surface, as shown in **Figure 2**. These are being analyzed to determine the activation energy for Ga desorption and the temperature dependence of the Ga sticking coefficient.

After formation of Ga nanodroplets on the sapphire surface, some of the samples were nitridated with a nitrogen plasma to form GaN nanodots. This allowed the real-space morphology of the droplets to be examined by post-facto atomic force microscopy (AFM) and electron microscopy with results that can be compared to existing simulations of droplet nucleation, growth, and coalescence. In addition, we found that this nanodroplet liquid phase epitaxy offered a novel approach to the formation of wide-bandgap semiconductor nanodots with size and density parameters that can be controlled by varying the absorption/desorption/nitridation times while monitoring the evolv-

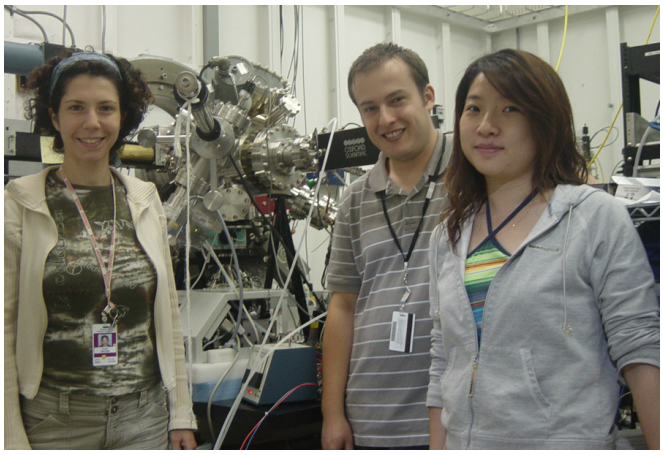

Authors (from left) Gozde Ozaydin, Ahmet Ozcan, and Yiyi Wang

ing morphology with real-time GISAXS. A typical post-facto AFM micrograph is shown in **Figure 3**; in this case, the average GaN dot diameter is approximately 30 nm and the typical height of the dots is 2-3 nm. Separate in-situ x-ray grazing-incidence diffraction experiments show that the GaN nanodots are epitaxial and almost completely strain relaxed.

Significant variations in the adsorption/desorption behavior are observed for different substrates. Gallium desorption is significantly higher from Ga-polar GaN surfaces than from sapphire surfaces. In order to better understand the adsorption and desorption of Ga on sapphire and GaN, the surface atomic structures have to be considered. On the c-plane sapphire surface, Ga adatoms can interact directly with O terminating atoms. In contrast, on Ga-polar GaN surfaces, the Ga adatoms will interact only with other Ga atoms forming weak, delocalized Ga-Ga metallic bonds. We are preparing to investigate further how this affects the actual film growth processes.

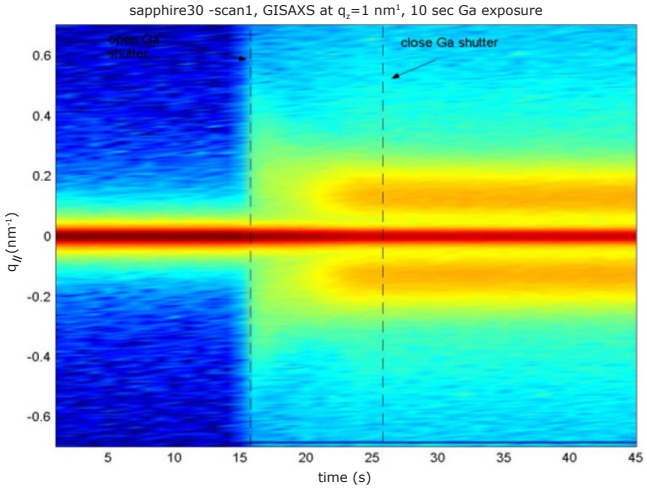

***Figure 1**. The real-time GISAXS evolution of the sapphire surface during Ga adsorption and desorption at 700 °C. The scan was taken at q_z = 1 nm^{-1}.*

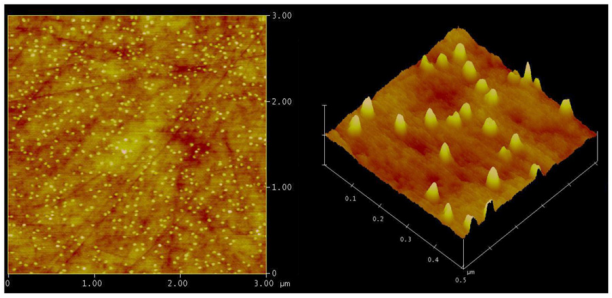

***Figure 3**. AFM analysis of the Ga nanodots on sapphire, showing a 3 x 3 micron AFM topograph. There is little or no wetting layer beneath the dots the polishing scratch marks are still clearly visible on the sapphire substrate.*

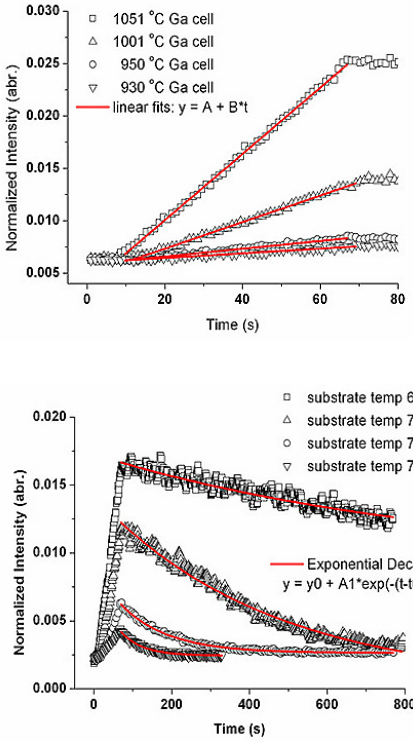

***Figure 2**. Ga fluorescence during (left) the absorption of Ga onto c-plane sapphire at different Ga cell temperatures and (right) during the desorption at different substrate temperatures.*

BEAMLINE
U7A

PUBLICATION
D.M. DeLongchamp, M.M. Ling, Y. Jung, D.A. Fischer, M.E. Roberts, E.K. Lin, and Z. Bao, "Thickness Dependence of Microstructure in Semiconducting Films of an Oligofluorene Derivative," *J. Am. Chem. Soc.*, **128**(51), 16579-16586 (2006).

FUNDING
National Institute of Standards and Technology

FOR MORE INFORMATION
Dean M. DeLongchamp, Polymers Division, National Institute of Standards and Technology
deand@nist.gov

Thickness Dependence of Microstructure in Semiconducting Films of an Oligofluorene Derivative

D.M. DeLongchamp[1], M.M. Ling[2], Y. Jung[1], D.A. Fischer[1], M.E. Roberts[2], E.K. Lin[1], and Z. Bao[2]

[1]National Institute of Standards and Technology; [2]Stanford University

The measurement and optimization of microstructure development in organic semiconductor films is valuable because microstructure critically impacts performance. We use surface-sensitive near edge x-ray absorbance fine structure (NEXAFS) spectroscopy to study the thickness dependence of microstructure in thin films of an organic semiconductor. We find that the molecule exhibits two different microstructure phases: one with large terraces within which molecules exhibit a strongly vertical orientation, and one with much smaller domains within which molecules exhibit a mildly horizontal orientation. We create transistors from each phase and confirm that the vertical microstructure with optimal π orbital alignment delivers superior charge carrier mobility.

Organic semiconductors will soon enable the low-cost fabrication of electronics on flexible substrates because they can be deposited directly from fluids. Unlike monolithic inorganic semiconductors such as silicon, organic semiconductors form a microstructure dynamically after deposition in a manner unique to each molecular structure. Measuring this microstructure is particularly challenging because the films are typically 20-50 nm thick, polycrystalline, and composed of complex molecules with chemically diverse subunits; x-ray diffraction alone is often not sufficient to solve the structure. The microstructure critically impacts performance because it determines the π orbital alignment in the film, and π orbital overlap enables charge carriers to move between molecules.

We used near edge x-ray absorbance fine structure (NEXAFS) spectroscopy to study the thickness dependence of microstructure in thin films of organic semiconductors. The application of surface spectroscopy to a well-ordered crystalline film allows us to isolate the configurations of the diverse chemical moieties of the molecules forming the lattice. The surface sensitivity of NEXAFS allows us to follow the development of these configurations as a film grows. We apply this technique to an oligofluorene derivative DDFTTF, which consists of an aromatic fluorene – bithiophene – fluorene core that is end-substituted with aliphatic dodecyl groups, as shown in **Figure 1**.

The substrate-relative orientations of the aromatic core and aliphatic end chains of DDFTTF can be isolated by the Carbon K-edge NEXAFS resonances illustrated in **Figure 1**. The 1s → π* orientation is orthogonal to the aromatic conjugated plane, while the 1s → σ* is dominated by the long axes of the aliphatic end chains. Incident angle-dependent NEXAFS spectra of thin DDFTTF films deposited on a heated substrate are shown in **Figure 2A**. The variation in the π* resonance indicates that the conjugated plane is edge-on upon the substrate surface. This vertical microstructure is optimal for carrier mobility in transistors because the π orbitals are aligned in the plane of the film, which is the transport direction. The variation in the σ* resonance indicates that the end chains are preferentially vertical but somewhat tilted. Comparing the allowed end chain tilt to the vertical lattice spacing proves that the end chains must be interdigitated or folded.

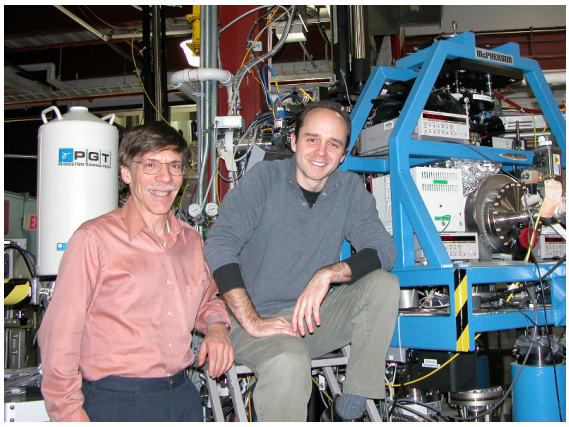

Authors Dan Fischer (left) and Dean DeLongchamp

When DDFTTF is deposited on colder substrates, it exhibits a transition from this vertical microstructure to a more horizontal microstructure, which reverses the variations of the resonances, as shown in **Figure 2B**. By

varying thickness and temperature over a larger range, we find that the relative distribution of these two preferential microstructures depends on the distance of the domains from the substrate and the substrate temperature during deposition.

The value of this method is confirmed using a lamination technique to create field effect transistors that can be both bottom- and top-gated. A laminated elastomer is used as a dielectric on the top interfaces. From these transistors we measure the saturation hole mobility at the top and bottom interfaces of DDFTTF films. We find that local microstructures with greater π orbital alignment in the transistor source-drain plane, such as those deposited in thin films at elevated substrate temperature, correlate directly to better local saturation hole mobilities. These correlations illustrate how fundamental microstructure studies can lead to practical guidelines for the knowledge-based process improvement and performance enhancement of organic electronics materials.

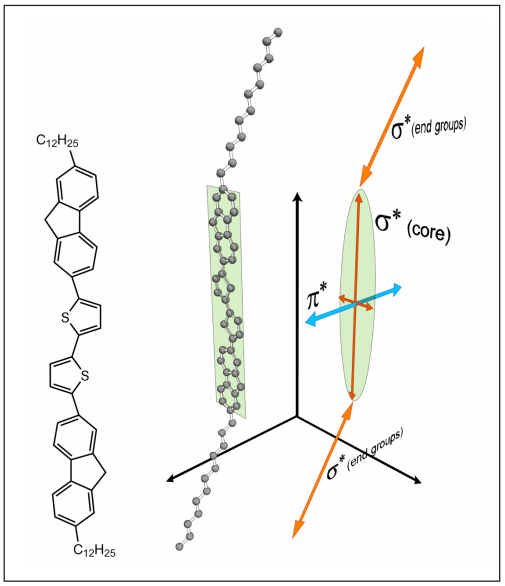

Figure 1. The DDFTTF molecule from three perspectives. From left to right: the DDFTTF primary chemical structure; an isometric view of DDFTTF as optimized by MOPAC (alone in vacuo); and a corresponding view of the directionality of DDFTTF carbon-carbon vector orbitals in the NEXAFS carbon K-edge. The conjugated plane is represented in green, the σ* orbital vectors are in orange, and the π* orbital vector is in blue.

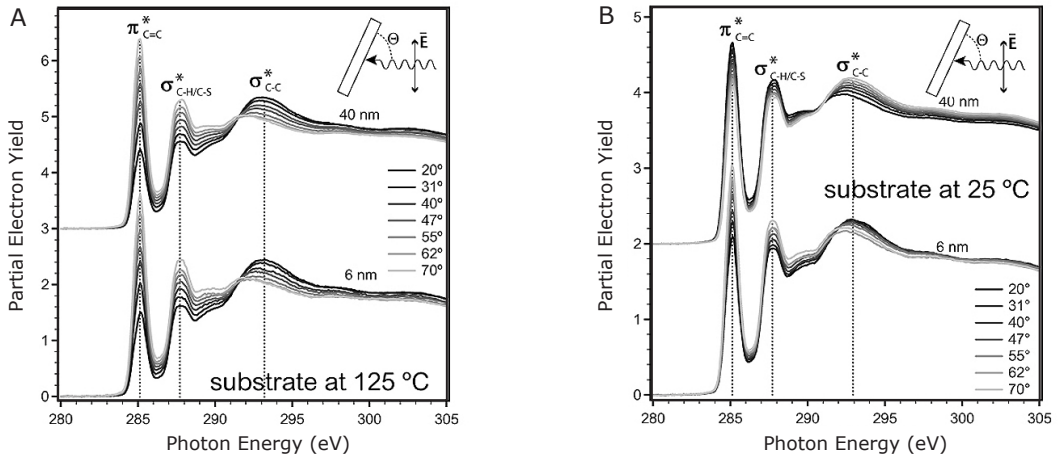

Figure 2 . (A) NEXAFS PEY spectra variation with incident angle for films deposited on hot substrates to 6 nm and 40 nm. (B) NEXAFS PEY spectra variation with incident angle for films deposited on room temperature substrates to 6 nm and 40 nm.

BEAMLINE
U7A

PUBLICATION
J.F. Douglas, K. Efimenko, D.A. Fischer, F.R. Phelan, and J. Genzer, "Propagating Waves of Self-Assembly in Organosilane Monolayers," *PNAS*, **104**, 10324-10329 (2007).

FUNDING
National Science Foundation

FOR MORE INFORMATION
Jack Douglas, Polymer Division
National Institute of Standards & Technology
Jack.Douglas@nist.gov

Jan Genzer, Department of Chemical & Biomolecular Engineering, North Carolina State University
Jan_Genzer@ncsu.edu

Progress in Self-Assembly: High Resolution NEXAFS Study of the Wave-like Growth of Self-Assembling SAM Layers on a Silicon Substrate

J. F. Douglas[1], K. Efimenko[3], D.A. Fischer[2], F.R. Phelan[1], and J. Genzer[3]

[1]Polymers and [2]Ceramics Divisions, National Institute of Standards and Technology; and [3]Department of Chemical and Biomolecular Engineering, North Carolina State University

Wavefronts associated with reaction–diffusion and self-assembly processes are ubiquitous in the natural world. Although it is often claimed that self-sustaining or autocatalytic front propagation is well described by mean-field "reaction–diffusion" or "phase field" ordering models, it has recently become appreciated from simulations and theoretical arguments that fluctuation effects in lower spatial dimensions can lead to appreciable deviations from the classical mean-field theory (MFT) of this type of front propagation. The present work explores these fluctuation effects in a real physical system. In particular, we consider a high-resolution near-edge x-ray absorption fine structure spectroscopy (NEXAFS) study of the spontaneous frontal self-assembly of organosilane (OS) molecules into self-assembled monolayer (SAM) surface-energy gradients on oxidized silicon wafers.

We examined the spontaneous self-assembly of organosilane molecules on an oxidized silicon surface. Upon exposure of the wafer to volatile source of the organosilane molecules placed to the side of the wafer in a closed container, a carpet-like layer spontaneously organizes from the edge of the wafer where the organosilane concentration is initially higher and this self-assembly process advances from the wafer edge at a constant velocity, ultimately covering the surface at long times (**Figure 1**).

By using high resolution X-ray synchrotron measurements in combination with simulation studies, we established that these wavefronts do not follow the constant width predicted by mean-field growth models widely assumed to model such "self-propagating" or "autocatalytic" growth processes. Instead, the interface region separating the ordered and disordered regions became progressively rougher in time and this broadening was described by a power-law growth predicted by previous simulation studies and theoretical arguments. The position of the wavefront is described by a relatively narrow interfacial region separating the ordered and disordered regions on the substrate that can be determined and tracked by NEXAFS measurements (**Figure 2**), which provide unique information about the density and ordering of the molecules on the surface. The novel aspect of this work is that the observations were being made for a real physical, rather than simulated, system.

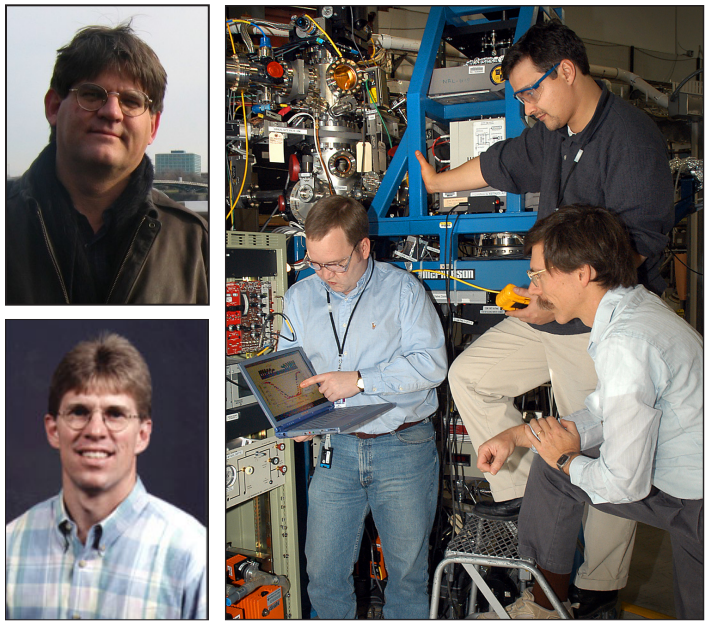

Authors: (from left, top) Jack Douglas, (bottom) Frederick Phelan, (Group, from left) Jan Genzer, Kirill Efimenko, and Daniel Fischer

Simple diffusion is not the process by which these SAM surface energy gradients fronts organize, as people had formally assumed. Unstable situations exist generically in the natural world and the

emergence of new, more stable, patterns of behavior having a lower energy or competitive advantage is a rather universal 'evolutionary' process. By studying this type of process in detail through high resolution measurement, as exemplified by the NEXAFS study of growth of SAM surface energy gradients, and by simulation studies, the group hopes to obtain insights into this fundamental growth phenomenon. This project offers the opportunity to compare the growth dynamics of the SAM layers with growth fronts found in numerous other (physical, biological and social dynamics) contexts such as crystallization, the polymerization of actin and the frontal polymerization of synthetic polymers, the spread of diseases, tumor growth, wound healing, and the spread of languages, and agricultural practices.

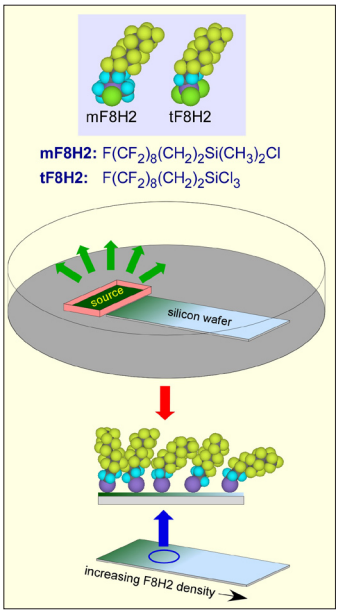

Figure 1. *Schematic illustration of the formation of self-assembled monolayer (SAM) surface energy gradients. Semifluorinated chlorosilane molecules are mixed with paraffin oil to control the rate of organosilane evaporation and this mixture is placed in a small container positioned at the edge of a silicon wafer subjected to a UV-ozone treatment. The evaporated chlorosilane molecules deposit on the wafer where the ordering process initiates from the edge of the wafer where the concentration is higher. The deposition is performed in a "confined" geometry (covering the OS source and wafer by a Petri dish).*

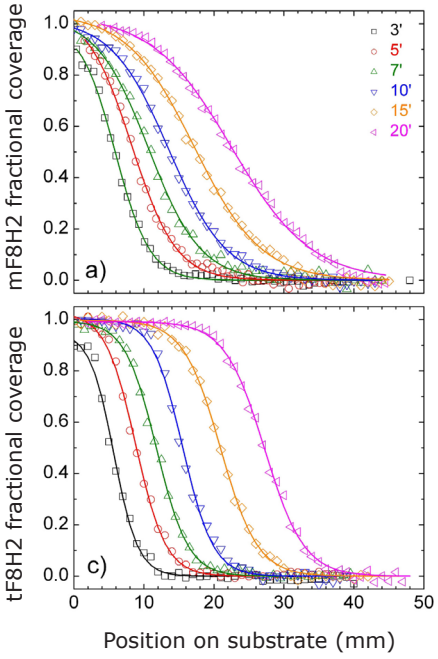

Figure 2. *Time development of mF8H2 and tF8H2 surface energy gradients. The figures indicate mF8H2 and tF8H2 fractional coverage, respectively, as a function of substrate position for a succession of times. Fractional coverage refers to the OS concentration relative that for the fully ordered layer. Lines represent best fits to a hyperbolic tangent function as discussed in the original publication.*

BEAMLINE
X20C

PUBLICATIONS
Delia J. Milliron, Simone Raoux, Robert M. Shelby, and Jean Jordan-Sweet. "Solution-Phase Deposition and Nanopatterning of GeSbSe Phase-Change Materials," *Nat. Mater.* **6,** 352-356 (2007).

FUNDING
IBM

FOR MORE INFORMATION
Delia J. Milliron, IBM Almaden Research Center
milliron@us.ibm.com

Solution-Phase Deposition and Nanopatterning of GeSbSe Phase-Change Materials

D.J. Milliron[1], S. Raoux[1], R.M. Shelby[1], and J. Jordan-Sweet[2]

[1]IBM Almaden Research Center; [2]IBM Watson Research Center

Chalcogenide films with reversible amorphous-crystalline phase transitions have been commercialized as optically rewritable discs, and intensive effort is now focused on integrating them into electrically addressed nonvolatile memory devices (phase change random access memory, or PCRAM). While optical data storage is accomplished by laser-induced heating of local spots within continuous films, electronic memory requires integration of discrete nanoscale phase-change material features with read/write electronics. Currently, phase-change films are most commonly deposited by sputter deposition, and patterned by conventional lithography. We are exploring an alternative, solution-phase deposition method for metal chalcogenide phase-change materials.

Soluble precursors for metal chalcogenide thin films are synthesized in the reducing solvent hydrazine. Isolated by removing the solvent, the resulting powders contain metal-chalcogen clusters, spaced apart by hydrazine molecules and hydrazinium ions. For phase-change material development, two precursors were synthesized: one containing Sb and Se, and another containing Ge and Se. These precursors decompose at low temperature (<200 °C), forming the extended bonding networks of metal chalcogenide materials. Upon thermal annealing, the Sb-Se precursor yields crystalline Sb_2Se_3, and the Ge-Se precursor yields an amorphous powder.

To deposit thin films, the precursors are dissolved and spin coated, then thermally annealed to form the phase-change material, an alloy of Ge, Sb, and Se. The precursors may be combined in solution in different ratios to tune the composition of the final film. For example, Ge-Se and Sb-Se precursors are mixed to prepare GeSbSe films, which are amorphous as deposited, while films of Sb_2Se_3, like the associated powder, are crystalline after annealing to decompose the precursor.

Crystallization of the phase-change films is characterized at the NSLS by continuously monitoring diffraction peaks during ramped thermal annealing. The crystallization temperature at which peaks first appear can be tuned by adjusting the level of Ge doping in GeSbSe films (**Figure 1a-d**). Higher Ge content stabilizes the amorphous state until crystallization is no longer observed above about 15% Ge.

Contrast in electrical resistivity between the amorphous and crystalline phases indicates the state of a PCRAM device – a digital 1 or 0. We characterize the resistivity contrast of our phase-change materials by measuring the resistance across two contacts as we thermally anneal the film. Since conduction is thermally activated, the resistance of the amorphous film drops slowly as it is heated. At the crystallization temperature, the resistance drops sharply since the crystalline state is more conductive. Upon cooling, the material remains in the crystalline state and the resistance is reduced from its initial value.

Delia Milliron

The kinetics of the amorphous-crystalline transition are probed by annealing local areas of the film with laser pulses and observing the time-dependent reflectivity. Enhanced reflectivity is indicative of crystallization, while decreased reflectivity indicates amorphization. A GeSbSe film is deposited on a 40 nm thick layer of Al_2O_3, which moderates heat transfer to the silicon substrate so that local areas may be melt-quenched and frozen in the amorphous state following a high-powered laser pulse. The amorphous spots formed by melt-quenching can be recrystallized by moderately powered laser pulses. The observed minimum recrystal-

lization time is about 100 ns.

During deposition of the precursor film, capillary forces can be leveraged to fill nanoscale patterns. Nanodot patterns of phase-change material can be formed using a block copolymer template (**Figure 2a**). The resulting phase-change nanodots (**Figure 2b,c**) crystallize in the same orthorhombic phase as the bulk film (**Figure 7d**), at a crystallization temperature reduced by 35 °C. Capillary filling can also fill high-aspect ratio via structures. Filling such vias with phase-change material can potentially reduce the critical RESET current in a PCRAM device.

We have demonstrated solution deposition of phase-change materials with tunable composition and crystallization temperature. Fast (~100 ns) switching is possible in spin-on GeSbSe films. Small- and/or high-aspect ratio vias can be filled easily with phase-change material deposited from solution. Next, we plan to integrate spin-on materials into prototype PCRAM devices and to explore new applications for spin-on metal chalcogenide materials.

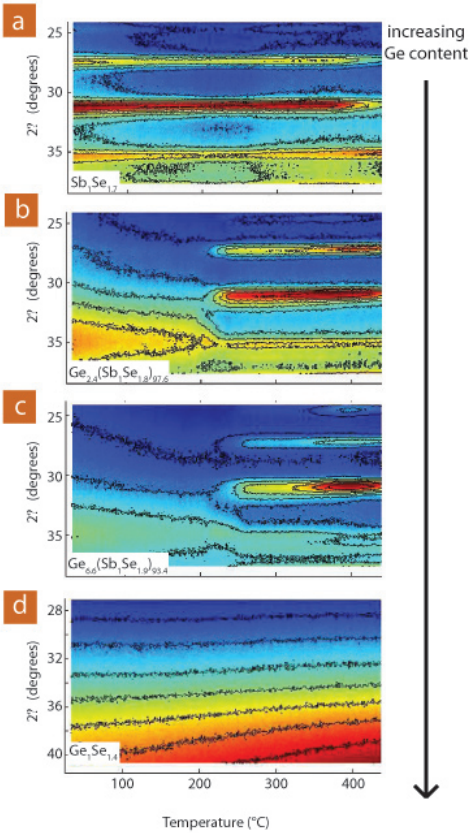

***Figure 1**. Thermal crystallization of GeSbSe films followed by temperature-dependent x-ray diffraction.*

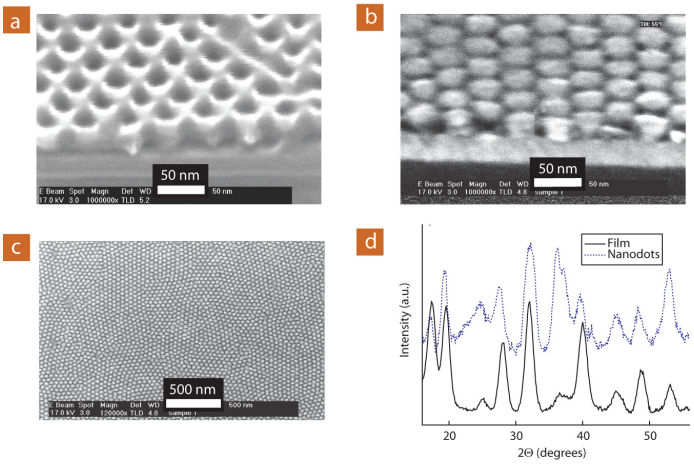

***Figure 2**. Nanopatterns of GeSbSe phase-change material formed using a block copolymer template.*

Featured Highlight

Breaking the Barrier Toward Nanometer X-ray Resolution
Possible advances for nanoscience, energy, biology, and materials research

A team of researchers at Brookhaven has overcome a major obstacle for using refractive lenses to focus x-rays. This method will allow the efficient focusing of x-rays down to extremely small spots and is an important breakthrough in the development of a new, world-leading light source facility that promises advances in nanoscience, energy, biology, and materials research.

At the NSLS, the scientists exceeded a limit on the ability to focus "hard," or high-energy, x-rays known as the "critical angle." Their results are described online in the September 28, 2007 edition of *Physical Review Letters*.

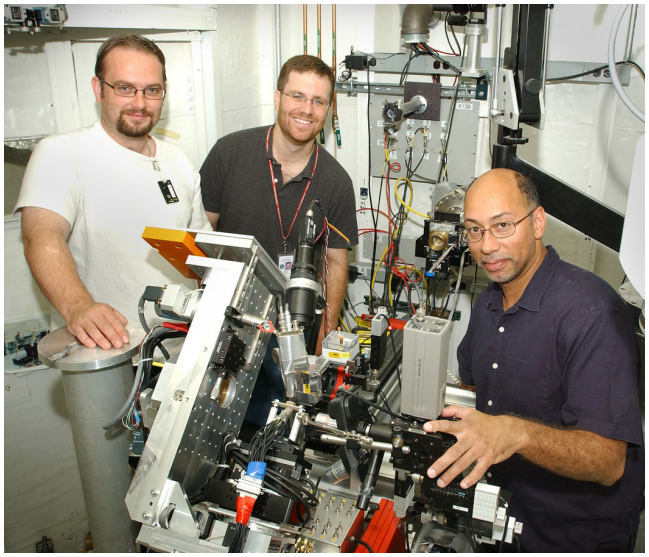

The research team at NSLS beamline X13B, from left: James Ablett, Aaron Stein, and Kenneth Evans-Lutterodt.

The critical angle is the maximum angle that light can be deflected, or bent, by a single surface. Imagine a beam of laser light traveling toward a glass lens. Depending on the characteristics of the lens material and the angle at which the beam is pointed, the light can be refracted, that is, transmitted through the lens but deflected. However, when this light approaches the lens at angles less than the critical angle, the beam does not pass through the lens but is instead reflected. This results in a maximum deflection angle for light that passes through the lens.

The maximum deflection angle determines the minimum spot size to which x-rays can be focused. This poses a problem for researchers who are using x-rays to study molecules, atoms, and advanced materials at the nanoscale – on the order of billionths of a meter. Such small subjects require tightly focused beams.

"One measure of the quality of an x-ray optic is how small a focused spot it can make," said NSLS researcher Ken Evans-Lutterodt. "The problem is that nature does not allow a single lens to deflect the x-rays very much. This limits how small of a spot you can create, and this translates to some fuzziness in the image. To get a sharper image, you need a lens that's more able to deflect the x-rays."

In 2003, a trio of Brookhaven researchers – Evans-Lutterodt, Aaron Stein, and James Ablett – were the first to notice the critical angle limit while investigating the properties of a so-called kinoform lens for focusing hard x-rays. This efficient type of refractive lens is similar to those found in lighthouses. The research team proposed a solution to the critical angle problem of a compound kinoform lens, and both the problem and proposed solution were also suggested later by other researchers in the field.

In the current publication, the researchers implemented their idea by creating a compound lens from a series of four kinoform lenses placed one after the other. Using this setup at NSLS beamline X13B, they showed that the critical angle can be surpassed with hard x-rays, while still focusing like a single lens.

"Thanks to the excellent fabrication resources at Brookhaven's Center for Functional Nanomaterials and at Alcatel-Lucent, we are able to fabricate the lenses to the precision required," Stein said.

This is an important step for the National Synchrotron Light Source II (NSLS-II), a state-of-the-art synchrotron facility that will produce x-rays up to 10,000 times brighter than those generated by the current NSLS and could lead to advances such as alternative-energy technologies and new drugs for fighting disease. One of the major goals of the facility is to probe materials and molecules with just one-nanometer resolution – a capability needed to study the intricate mechanisms of chemical and biological systems.

"Without exceeding the critical angle, the refractive lens resolution would be limited to 24 nanometers or more," Ablett said. "Even though in this experiment

we just barely exceeded this limit, we've shown that it can be done. This is just the first step."

Next, the researchers will measure the resolution their new lens system produces, and will continue to fabricate and test optics that push further beyond the critical angle, and closer to the one-nanometer benchmark.

"We've broken the barrier, now there's still more work to be done to get down to those small x-ray spots," Evans-Lutterodt said. "Hopefully this will be one of the routes that NSLS-II and others will use."

Natasha Bozovic, from San Jose State University, also collaborated on this research. Funding was provided by the Office of Basic Energy Sciences within the U.S. Department of Energy's Office of Science.

For more information, see: K. Evans-Lutterodt, A. Stein, J. Ablett, N. Bozovic, A. Taylor, and D. Tennant, "Using Compound Kinoform Hard X-Ray Lenses to Exceed the Critical Angle Limit," Phys. Rev. Lett., ***99****, 134801 (2007).*

—Kendra Snyder

Featured Highlight

Researchers Produce Firsts with Bursts of Light

Team generates most energetic terahertz pulses yet, observes useful optical phenomena

BNL researchers have generated extremely short pulses of light that are the strongest of their type ever produced and could prove invaluable in probing the ultra-fast motion of atoms and electrons. The scientists also made the first observations of a phenomenon called cross-phase modulation with this high-intensity light – a characteristic that could be used in numerous new light source technologies.

The work, which was done at Brookhaven's Source Development Laboratory, an offshoot of the Lab's National Synchrotron Light Source (NSLS), is described online in the July 23, 2007, edition of *Physical Review Letters*.

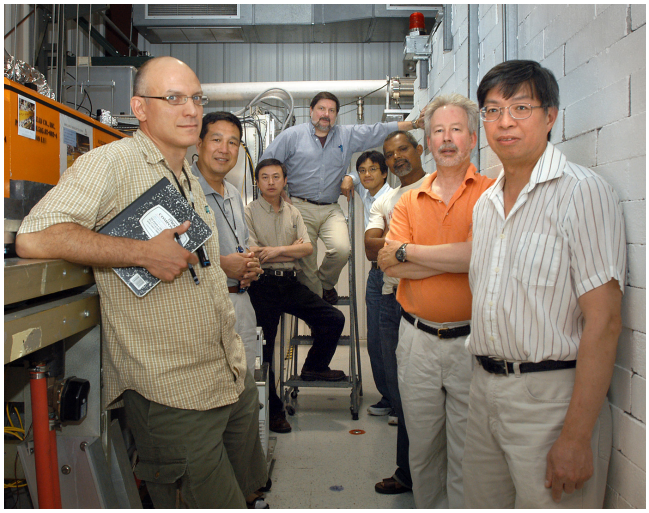

Authors (from left) Dario Arena, Xijie Wang, Yuzhen Shen, Larry Carr, Takahiro Watanabe, Boyzie Singh, James Murphy, and Thomas Tsang at the Source Development Lab.

The light pulses used were in the terahertz (THz) range of the broad electromagnetic spectrum, found between the microwave and infrared range. Scientists send tight bunches of electrons at nearly the speed of light through a magnetic field to produce THz radiation at a trillion cycles per second — the terahertz frequency that gives the light its name and that makes them especially valuable for investigating biological molecules and imaging, ranging from tumor detection to homeland security.

The Brookhaven team is looking to expand the potential uses for this type of light by increasing the strength of individual THz pulses, a longtime goal for scientists in the field. By slamming an electron beam from an accelerator into an aluminum mirror, the researchers produced 100 megajoule (100 megawatt) single-cycle pulses – the highest energy ever achieved to date with THz radiation. For comparison, 100 megawatts is about the output of a utility company's electrical generator.

The combination of this newfound strength with ultra-fast pulses provides researchers with a powerful new tool to study the movement of a material's electrons (which zip around at the femtosecond, or quadrillionth of a second, timescale) or atoms (which move at the picosecond, or trillionth of a second, timescale).

"The goal is really to understand the properties of materials," said NSLS researcher Yuzhen Shen, the lead author of the paper. "One might ask what happens in a solid when light, electricity, or sound goes through it, and it's all related to atoms in a crystal wiggling around or the movement of electrons. So the effort surrounding ultra-fast pulses is going into making tools to probe the real fundamental properties of materials on the scales at which they move."

Using this strong light, researchers can "kick" molecular processes such as catalysis or electronic switching (important for developing data storage media) into action and watch their mechanisms on a very short timescale.

The team also found something surprising: the intensity of their THz pulses is so great that they introduce so-called "nonlinear optical effects," specifically, a phenomenon known as cross-phase modulation.

"When you pull on a spring, if you pull twice as hard, it stretches twice as much," said NSLS researcher Larry Carr. "But there's a limit where if you pull twice as hard, the spring doesn't move anymore. That's when it's called nonlinear. The same thing happens in materials. You let these short pulses pass through a material, and they stress it and pull some of the charges apart so they don't act in a linear manner."

As a result, the researchers can manipulate both the ultra-fast THz pulses and the material they interact with. Some of the simplest examples include changing the color of the light or turning the material into a focusing lens.

This is the first time cross-phase modulation has been observed in single-cycle THz pulses. Learning how to control this characteristic could lead to even more light source technologies.

This research was supported by the Office of Basic Energy Sciences within the U.S. Department of Energy's Office of Science, the Office of Naval Research, and Brookhaven's Laboratory Directed R&D funds.

For more information, see: Y. Shen, T. Watanabe, D.A. Arena, C.-C. Kao, J.B. Murphy, T.Y. Tsang, X.J. Wang, and G.L. Carr, "Nonlinear Cross-Phase Modulation with Intense Single-Cycle Terahertz Pulses," Phys. Rev. Lett., ***99****, 043901 (2007).*

— Kendra Snyder

Boosting Speed, Precision of X-ray Fluorescence Microprobes

Combining large, high-resolution detector arrays with an advanced analysis technique, researchers from the NSLS, BNL's Instrumentation Department, and Australia's Commonwealth Scientific and Industrial Research Organization (CSIRO) have developed an x-ray fluorescence microprobe system that will be about 1,000 times faster than previous methods.

X-ray fluorescence is a powerful technique usually used in the environmental and geological sciences for measuring trace element concentrations in a sample. Typically, a very tiny x-ray spot is focused on a sample, which ionizes electrons from the material's atoms. These excited atoms relax, filling the vacancies, and in doing so, emit x-rays at energies characteristic of specific elements. However, scientists can only determine the elements present in the portion of the sample that's exposed to the x-ray spot. To get an idea of the entire sample's chemical composition, the spot must be manually moved from one location to another – a process that can take many hours to produce low-resolution maps of just a few thousand pixels.

"You have to stop and start and it's a pain in the neck," said NSLS physicist Peter Siddons. "So we came up with a method that would allow us to scan the scheme continuously along a line. The exposure time is just a few milliseconds at each point so, like previous 'on-the-fly' scanning systems, it never really stops moving. However, we collect full spectral data as we go.

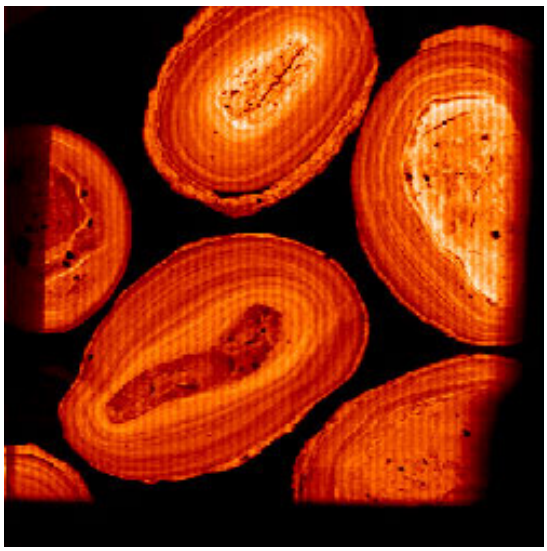

Iron-oxide nodules imaged using the 32-element prototype detector array at NSLS beamline X27A. (12x12mm^2, 375x375 pixels at 32ms/pixel)

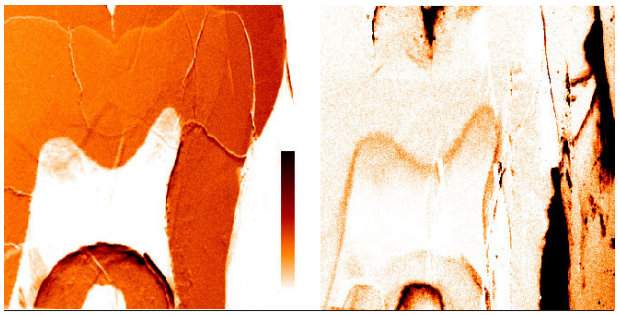

Calcium (left) and lead in a 14th century tooth imaged using the 32-element prototype detector array at NSLS beamline X27A. The color legend distinguishes high (top) from low concentrations. The tooth was supplied by *Rudiger Brenn, University of Freiberg. (12x12 mm^2, 2000x2000 pixels at 6ms/pixel, 6.7 hours acquisition).*

That not only makes it fast, but allows a high-quality quantitative analysis as well."

The new scanning method, which has been tested at NSLS beamline X27A, also includes two other improvements upon the old technique. The first is the use of a multi-element detector, which incorporates many small detectors (32 in the test run) into one device, instead of using one large detector.

"These experiments are limited not only by mechanical speed, but also by how many photons you're detecting from the x-ray spot," Siddons said. "There are always more than enough photons in the synchrotron spectrum to excite these samples and saturate the detector. By making the detectors smaller and making more of them, we can collect more signal at each position in the map, or do it much faster."

The final pieces of the new fluorescence microprobe system are advanced data analysis techniques that can handle the increased data processing speed and map the x-ray energies in real time. Led by physicist Chris Ryan, scientists at CSIRO developed software and hardware to unfold the signals from chemical elements at up to 100 million events per second.

"The combination of large multi-element detectors, fast scan mapping, and real-time processing means we can tackle challenging new approaches in a realistic timescale," Ryan said. "Techniques such as chemical-state imaging and fluorescence tomography will now become practical tools, made possible with this massive increase in speed and throughput."

In the first demonstration of this technique, which was detailed in the *2006 Goldschmidt Conference Abstracts*, the research team produced a 4 mega pixel image of a 14th century tooth and looked for lead accumulation that might indicate the presence of lead poisoning hundreds of years ago.

"The image was produced in just about six hours, a task that would normally take days", Siddons said. "No one ever did a 4 mega pixel image before because it would just take too long."

Now, the group is building two 400-element detectors: one for the NSLS and one for the Australian Synchrotron. They are expected to produce scanning images 1,000 times faster than the traditional x-ray fluorescence technique.

Other scientists involved in the research include Gareth Moorhead, Paul Dunn, Robin Kirkham, Robert Hough, and Barbara Etschmann, all of CSIRO; and Angelo Dragone and Gianluigi De Geronimo, from BNL. This research was funded by the U.S. Department of Energy and the CSIRO Emerging Science program.

For more information, see: C. Ryan, D. Siddons, G. Moorhead, P. Dunn, R. Kirkham, A. Dragone, G. De Geronimo, R. Hough, and B. Etschmann, "The Next Generation of Synchrotron Fluorescence Imaging for Geological Applications," Geochim. Cosmochim. Acta, ***70****, A550 (2006).*

— Kendra Snyder

Featured Highlight

Researchers Observe Superradiance in a Free Electron Laser
Technique paves way for generating ultra-short pulses in future light sources

A team of researchers at the U.S. Department of Energy's (DOE) Brookhaven National Laboratory has generated extremely short light pulses using a new technique that could be used in the next generation of light source facilities around the world to catch molecules and atoms in action. Published on January 19, 2007 in *Physical Review Letters*, the research team's findings describe the use of a laser to control the pulse duration of light from a free electron laser (FEL), a type of light source with a brightness up to one billion times higher than that of ordinary synchrotron light. The team also reports the first experimental observation of a phenomenon called superradiance.

Most of the world's light sources – facilities such as Brookhaven's National Synchrotron Light Source (NSLS) that produce x-ray, ultraviolet, and infrared light for research in fields ranging from biology to nanotechnology – produce a broad range of wavelengths, or colors of light. This is ideal for hosting a wide variety of experiments, but to understand how molecules change their structure in chemical and biological systems, scientists need extremely short pulses of light (shorter than one trillionth of a second) with short wavelengths. This is where FELs are valuable, as they can provide pulses of light that are a thousand times shorter than those produced at existing light sources and contain a million more photons per pulse. Like a strobe flash, the ultra-short FEL allows scientists to take time-resolved images of biological and chemical processes and various other atomic-scale events.

"In existing light sources, we just take a static snapshot of a sample," said NSLS physicist Takahiro Watanabe, one of the paper's authors. "We get the location of the pieces, but what happens if the pieces move? You don't know how they actually got there. What you want is to take images along the way to see these things move, and that's where these ultra-fast sources come into play."

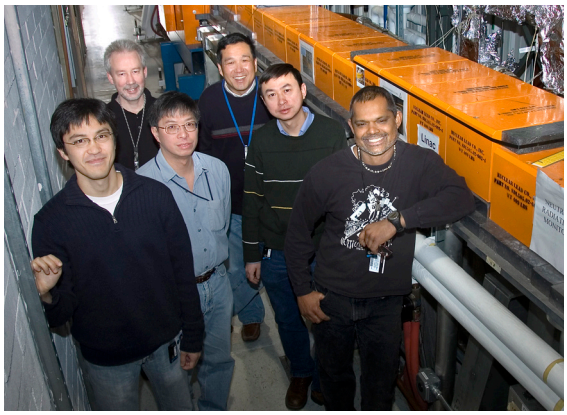

From left, Takahiro Watanabe, James Murphy, Thomas Tsang, Xijie Wang, Yuzhen Shen, and Boyzie Singh at the Brookhaven Source Development Lab.

Synchrotron light is produced by accelerating of a beam of electrons and sending it through a magnetic field. Generally, the pulse duration of both synchrotron and FEL light is determined by that of the electron beam. Tremendous effort has been devoted to generating short electron pulses, but scientists have been unable to shorten the electron pulse past a certain point because of forces that repel the electrons in the beam away from each other. At Brookhaven's Source Development Lab (SDL), researchers found a way to generate a very short FEL pulse that doesn't depend on the length of the electron pulse. This was done using a titanium-sapphire laser that combines a femtoseconds pulse of light with the much longer electron beam. A femtosecond is extremely fast – one billionth of one millionth of a second. This leads to a femtosecond FEL pulse that keeps growing in intensity and shortening in time duration, which is attributed to a phenomenon called superradiance.

"The electron beam and the laser beam don't move at the same speed, they slip a little bit," Watanabe said. "So this scenario provides new areas on the electron beam for the interaction to continue and allows the intensity of light to keep growing."

Superradiance was first proposed in 1954 as the most efficient way to extract energy from either atomic or molecular systems, but the SDL research group is the first to experimentally observe its effects in this type of FEL setup. Understanding how to produce these intense, ultrafast pulses of light could help scientists around the world as they begin to construct the next generation of light source facilities.

Other members of the group include James Murphy, Xijie Wang, James Rose, Yuzhen Shen, and Thomas Tsang of Brookhaven National Laboratory; Luca Giannessi of the ENEA, Frascati, Italy; Pietro Musumeci of the National Institute of Nuclear Physics, Italy; and Sven Reiche of the University of California, Los Angeles. The Office of Naval Research provided funding for this study. NSLS operations are funded by the DOE's Basic Energy Sciences program within the Office of Science.

For more information, see: T. Watanabe, X.J. Wang, J.B. Murphy, J. Rose, Y. Shen, T. Tsang, L. Giannessi, P. Musumeci, and S. Reiche, "Experimental Characterization of Superradiance in a Single-Pass High-Gain Laser-Seeded Free-Electron Laser Amplifier," Phys. Rev. Lett., ***98****, 034802 (2007).*

— Kendra Snyder

BEAMLINE
BNL-SDL

PUBLICATION
J. Wu, P.R. Bolton, J.B. Murphy, and X. Zhong, "Free Electron Laser Seeded by IR Laser Driven High-Order Harmonic Generation," *Appl. Phys. Letts.*, **90**, 021109 (2007).

FUNDING
U.S. Department of Energy
U.S. Office of Naval Research

FOR MORE INFORMATION
Juhao Wu, Stanford Linear Accelerator Center
Jhwu@SLAC.Stanford.edu

Getting Closer to Fully Coherent Hard X-ray Femtosecond Free Electron Lasers

J. Wu[1], P.R. Bolton[1], J.B. Murphy[2], and X. Zhong[3]

[1]Stanford Linear Accelerator Center, Stanford University; [2]National Synchrotron Light Source, Brookhaven National Laboratory; [3]Institute of Low Energy Nuclear Physics, Beijing Normal University

We have achieved a crucial step that bridges the femtosecond high-order harmonic generation (HHG) community and the free electron laser (FEL) community. This research provides convincing proof that a femtosecond HHG seed with a wavelength of tens of nanometers can be up-converted in frequency to produce hard x-ray FEL emission with both spatial and temporal coherence. The duration of the seeded x-ray FEL emission is still tens of femtoseconds, almost the same as the HHG seed duration. Thus, fully coherent hard x-ray femtosecond FELs are feasible.

Juhao Wu

James Murphy

Paul Bolton

As scientific research continues to explore the limits of smaller (nanometer and sub nanometer) and faster (femtosecond and attosecond) phenomena, light pulses are commonly used as probing tools. Investigating such phenomena requires a hard x-ray pulse of femtosecond duration or less. Hard x-ray sources exist at light sources around the world. However, their duration is typically tens of picoseconds (one picosecond is 1,000 femtoseconds) because the x-ray pulse duration is determined by the electron bunch duration. Although femtosecond x-ray pulses can be obtained by using only a short temporal slice of an electron bunch, these "sliced" x-ray sources have significantly reduced flux and are incoherent.

Alternatively, in free electron lasers (FELs) electrons of a single bunch wiggle their way through an undulator, initiating instability. Exponential growth of this instability greatly enhances the peak power of the FEL emission toward saturation. FELs are therefore capable of generating light levels that exceed those of conventional synchrotron sources by many orders of magnitude. Yet, the duration of this FEL emission is still comparable to the electron bunch duration. By simply relying on the FEL instability, with a 100-meter long undulator, x-ray FEL emission can have good transverse (spatial) coherence, but lacks longitudinal (temporal) coherence. This is because the FEL instability is initiated by spontaneous undulator radiation, which is not temporally coherent.

A proposed solution is seeded FEL emission, in which the instability is initiated by a coherent seed laser pulse. In this scheme, electrons are modulated by the seed laser such that they know each other's relative phase. Fortunately, FEL emission can also occur at harmonics of the seed laser wavelength. This is crucial, because we can then up-convert the seed laser frequency to hard x-ray regime. However, there are upper limits to the FEL up-conversion factor. In such a seeded FEL scheme, the final FEL pulse duration is determined by the seed laser pulse duration, which can be much shorter than the electron bunch duration.

A promising seed candidate is the high-order harmonic generation (HHG) generated by ultrashort infrared or visible laser pulses in gas targets. The HHG wavelength can be as low as tens of nanometers. But the HHG generation efficiency imposes lower limits to the seed pulse wavelength. So up-conversion in the FEL process by a factor of 100 would bring us to the exciting Angstrom wavelength regime. The HHG pulse duration

is typically tens of femtoseconds and the up-converted, seeded FEL duration is comparable.

A more detailed view of an HHG seed pulse shows that it is comprised of many harmonics of the IR (or visible) laser frequency and temporally amounts to a series of attosecond spikes (an attosecond pulse train) as the red curve shown in **Figure 1**. So within the FEL community, the extent to which an HHG seed pulse can drive the FEL instability maintaining phase coherence has been contemplated. This is a challenge for numerical simulation, because one has to numerically resolve the attosecond structure of the unique HHG pulse train. Instead, we took an analytical approach to show that the attosecond structures of the seed pulse would be smeared out within a very short distance inside the undulator. For the example in our paper, at a distance of 18 cm into the undulator, the attosecond structures are almost smeared out as the blue curve in **Figure 1**. The HHG seed would effectively act as a harmonic pulse that is generated via standard wave mixing in a crystal, since the light pulse approaches the smooth green curve very quickly as in **Figure 1**. We further proved that the FEL acts as an extremely narrow band filter to the extent that only one particular harmonic order in the HHG seed pulse interacts with the electron bunch, and experiences exponential gain. The other very important pioneering development in this work is clarification of the noise issue in seeded FELs by distinguishing the undulator amplifier bandwidth and the seeded FEL bandwidth. We present crucial proof that the undulator noise will not significantly degrade the phase coherence of the final x-ray FEL, even after the 100 times up-conversion to the FEL frequency. This has been a concern for years. Finally, we have established convincingly that the HHG-seeded FEL duration would remain almost the same as the original HHG seed pulse duration.

So what have we achieved? — A clear analytical basis that establishes the feasibility of hard x-ray femtosecond FEL emission with both spatial and temporal coherence.

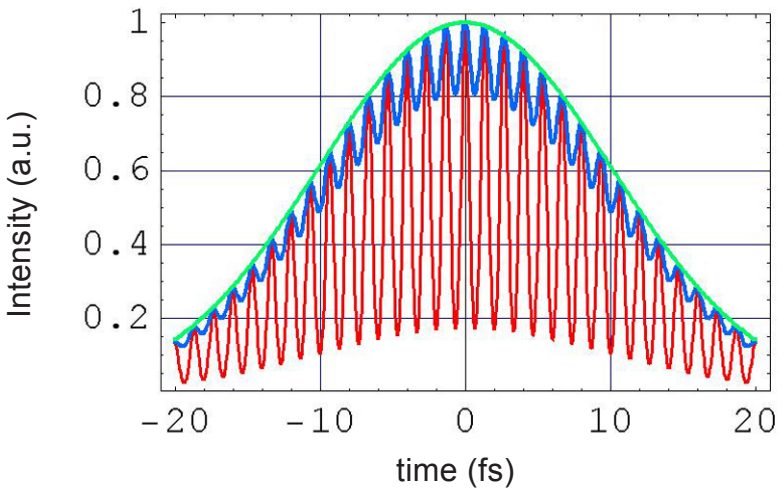

Figure 1. *Illustration of the smearing effect in the FEL process. The red curve is the initial HHG seed pulse with attosecond structures. For the example in the paper, the blue curve is at a distance of 18 cm into the undulator, where the attosecond structures are quickly smeared out to approach the smooth pulse as the green curve.*

BEAMLINES
X17B1, X6A

PUBLICATION
J. Jakoncic, M. Di Michiel, Z. Zhong, V. Honkimaki, Y. Jouanneau, and V. Stojanoff. "Anomalous Diffraction at Ultra-High Energy for Protein Crystallography," *J. Appl. Cryst.*, **39**, 831-841 (2006).

FUNDING
National Institute of General Medical Sciences; U.S. Department of Energy; European Synchrotron Radiation Facility

FOR MORE INFORMATION
Jean Jakoncic and Vivian Stojanoff, Brookhaven National Laboratory, National Synchrotron Light Source
jakoncic@bnl.gov and stojanof@bnl.gov

Anomalous Diffraction at Ultra High Energy for Macromolecular Crystallography

J. Jakoncic[1], M. Di Michiel[2], Z. Zhong[1], V. Honkimaki[2], Y. Jouanneau,[3] and V. Stojanoff[1]

[1]Brookhaven National Laboratory, National Synchrotron Light Source; [2]European Synchrotron Radiation Facility, France; [3]CNRS CEA, France

Ultra high-energy x-rays were employed for the first time in a macromolecular crystallography experiment. High-resolution diffraction data recorded on frozen samples allowed for the determination of the crystal structure of a model protein. Phases were determined at high resolution using various methods such as Multiple-wavelength Anomalous Diffraction (MAD), Single-wavelength Anomalous Diffraction (SAD) and Single Isomorphous Replacement with Anomalous Scattering (SIRAS). 1.25 Å diffraction resolution was achieved for the best sample. No radiation damage was observed from the experimental data an indication that at ultra high-energy x-ray radiation damage is minimized as the mass-energy absorption coefficient is much smaller therefore resulting in a lower energy dose absorbed by the sample.

Radiation damage to biological crystals is a major challenge in the determination of the crystal structure of macromolecules at conventional x-ray energies. At 12 keV, the dominance of the photoelectric effect leads to energy deposition that causes premature radiation-induced death of the crystals. Typical sample lifetimes can be extended somewhat with the use of cryogenic temperatures, but it has been shown that it will be insufficient for third-generation, synchrotron-based beamlines. The use of higher energy x-rays, advocated by Helliwell and Fourme (Helliwell and Fourme, 1983), lowers the risk of radiation damage due to the lower photoelectric effect cross section while higher scattering cross section can be preserved by the use of heavy elements.

The purpose of the experiments pursued on X17B at the NSLS and ID15B at the ESRF, two beamlines dedicated to material sciences, was to exploit the use of ultra high-energy x-rays, in the 55 keV range, for the crystal structure determination of macromolecules. Only a couple of experiments so far have been performed in the 35 keV range, mainly because this is the limit in the achievable energy for macromolecular crystallography beamlines at synchrotron facilities.

The data collected on a chicken lysozyme sample co-crystallized with holmium allowed us to explore a large variety of phasing methods (**Figure 1**). A Bijvoet-difference Fourier map calculated with the high-energy remote data (SAD) approximately 1 keV below the holmium K edge (at 56.5 keV) is shown in **Figure 2**. The map, contoured at 11σ level, clearly indicates three occupied sites. The Bijvoet ratio, calculated with the refined occupancies is 2.5 %, indicating the potential use for holmium as one of the standard heavy atoms for ultra high-energy measurements. The quality of the phases after density improvement (**Figure 1**) allowed us to automatically build the totality of the molecule for all the phasing methods tested.

Marco Di Michiel (left) and Veijo Honkimaki

Additional data collected at ID15B at the high-energy remote, 56.5 keV, corresponding to a total cumulated exposure of 93 min and an estimated cumulated dose of 1.7 x 10^6 J.kg^{-1}, was compared to data collected on NSLS beamline X6A at 12keV

(total cumulated exposure 93 min and estimated dose 7 x 10^6 J.kg^{-1}). Crystals grown under the same conditions, with similar sizes presenting the same diffracting resolution, 1.3 Å, exposed to 12keV, showed the onset of radiation damage after a cumulated exposure of 18 min, while no radiation damage was observed in the data collected at ultra high-energy x-ray for the total cumulated exposure. In conclusion, high- and ultra high-energy can be efficiently used to determine a crystal structure while minimizing radiation damage effects.

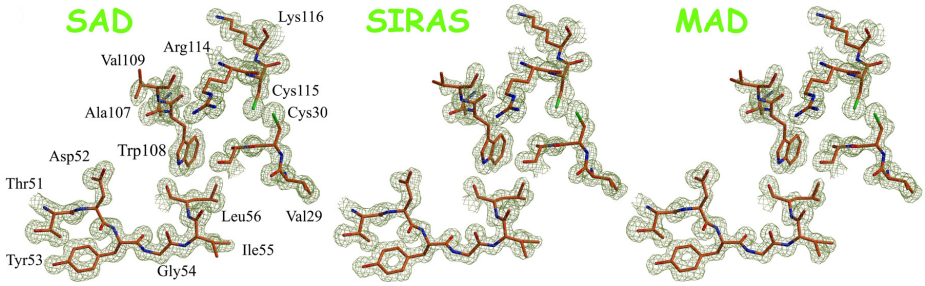

Figure 1. *Experimental electron density maps after density improvement (before model building and refinement). All 3 maps are contoured at 1σ level and calculated around the same region, the residues indicated in the left panel.*

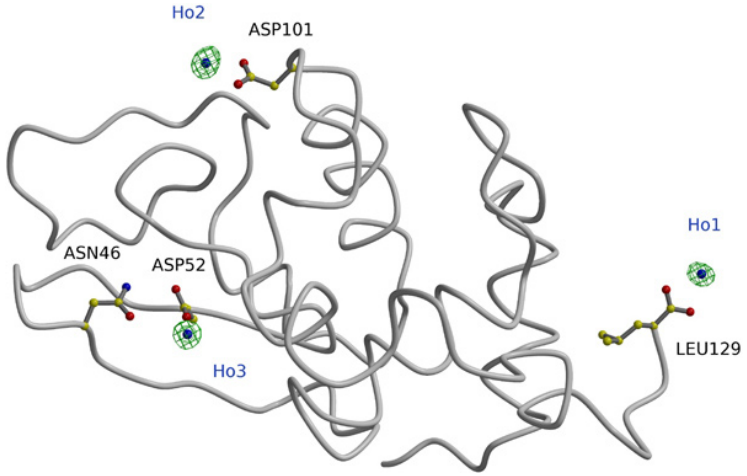

Figure 2. *Bijvoet-difference Fourier map. The map is contoured at the 11s level and calculated with Bijvoet pairs from the high-energy remote (56.5 keV) data collected on X17B1.*

BEAMLINE
X1A

PUBLICATIONS
M. Feser, B. Hornberger, et. al,. "Integrating Silicon Detector with Segmentation for Scanning Transmission X-ray Microscopy," *Nucl. Instrum. and Meth. in Phys. Res. A*, **565**, 841-854, (2006).

B. Hornberger, et al., "Quantitative Amplitude and Phase Contrast Imaging in a Scanning Transmission X-ray Microscope," *Ultramicroscopy*, **107**, 644-655, (2007).

FUNDING
National Institutes of Health; National Science Foundation; U.S. Department of Energy; Max Planck Society

FOR MORE INFORMATION
Benjamin Hornberger, Dept. of Physics and Astronomy, Stony Brook University
hornberg@xray1.physics.sunysb.edu

Phase Contrast Made Quantitative With New Detector and Advanced Analysis Techniques

M. Feser[1], B. Hornberger[1], C. Jacobsen[1], G. De Geronimo[2], P. Rehak[2], P. Holl,[3] and L. Strüder[3]

[1]Department of Physics and Astronomy, Stony Brook University; [2]Instrumentation Division, Brookhaven National Laboratory; [3]Max Planck Semiconductor Laboratory, Germany

It's gentler on a specimen if it can bend x-rays rather than absorb them. Scientists at Stony Brook University have developed a way to use this beam-bending effect to obtain quantitative phase contrast images in scanning x-ray microscopes and microprobes, by using a special detector developed in collaboration with Brookhaven Lab and the Max Planck Semiconductor Lab.

An x-ray beam passing through a specimen can be absorbed as well as refracted. Traditionally, absorption has been used to produce contrast in x-ray microscopes, but this does not work well if the specimen is damaged by the absorbed radiation, or just does not absorb enough to produce sufficient contrast – as it happens at higher photon energies. However, consider the effect of a rough water surface in a swimming pool: although the water absorbs light barely at all, we see bright and dark patches at the bottom of the pool. This is because refraction redirects the light depending on the surface angle of the water, so that some areas receive more light than others. This redirection produces phase contrast, and this effect can also be exploited in x-ray imaging.

A variety of approaches to phase contrast x-ray imaging have been developed worldwide. Our goal was to make phase contrast available in a scanning microscope, because these kinds of microscopes also let you collect other useful signals (x-ray fluorescence from trace elements, for example) and are already good in minimizing damage to the specimen. An x-ray lens (Fresnel zone plate in this case) is used to focus the beam to a tiny, 35 nm resolution spot through which the specimen is scanned. The usual approach is to measure the total transmitted intensity for each image pixel, which produces an absorption image of the specimen. However, if a detector that is divided into segments is used, the difference image of opposing segments provides a measure of the beam deflection of the specimen at each scan pixel. At the same time, the signals from all segments can be added up to produce the same absorption image of a traditional single detector.

Benjamin Hornberger (left) and Michael Feser displaying the segmented detector

A key step was to develop a segmented detector with high efficiency and rapid readout. Such a detector has been developed by our team, which includes Michael Feser, Benjamin Hornberger, and Chris Jacobsen from Stony Brook University, and Pavel Rehak and Gianluigi De Geronimo from BNL's Instrumentation Division along with Lothar Strüder and Peter Holl from the Max Planck Semiconductor Laboratory in Munich, Germany.

With this detector, it is easy to display difference signals between detector segments and thus provide what are called differential phase contrast images. However, going from these images of differences in the specimen, to

direct images of the phase shift of the specimen, is desirable (for example for measuring the mass of the specimen as needed in quantitative concentration calculations of trace element fluorescence) yet not straightforward. We have built upon previous work in electron microscopy to develop a Fourier filtering method, which can be used to obtain quantitative phase contrast images from the segmented detector. We represented the imaging process in the x-ray microscope mathematically, and then inverted the process to recover the specimen from the images obtained. This procedure recovers amplitude *and* phase of the specimen, while removing the blurring effects of the optical system.

The method has been demonstrated with a Germanium test pattern imaged at NSLS beamline X1A, where the recovered values of absorption and phase shift compared well with the numbers expected from tabulated material properties. Currently, the method is being implemented at Argonne National Laboratory's Advanced Photon Source because it is particularly useful when using higher photon energies, as is commonly done there. In the future, it could be very attractive for the upcoming NSLS-II and its proposed x-ray nanoprobes.

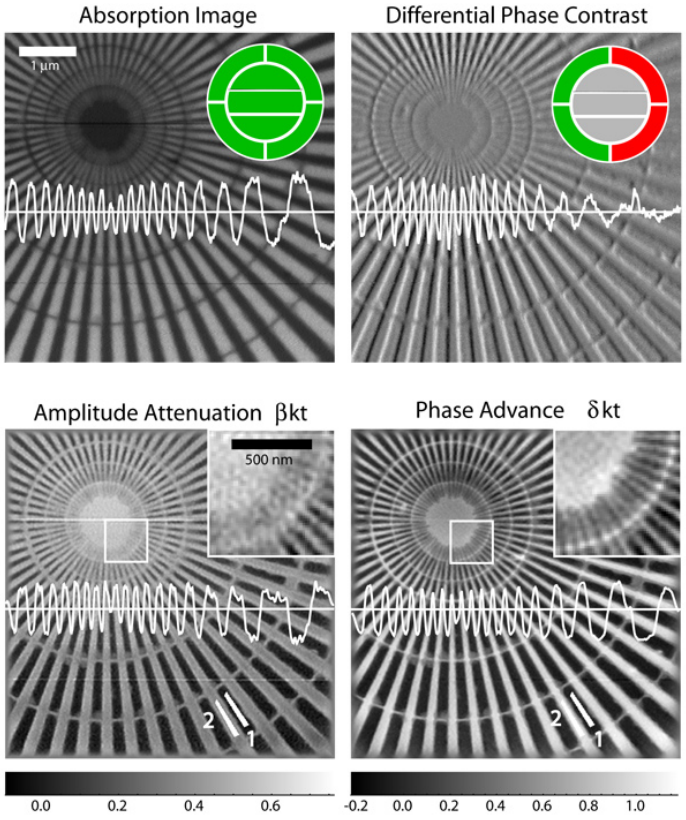

Images of a Germanium test pattern. Top left: Traditional absorption image, obtained by summing up all detector segments (see inset). Top right: Differential phase contrast image, obtained from the difference signal of left and right segments. The differential nature of the image leads to a three-dimensional appearance. Bottom left: Amplitude attenuation reconstructed by Fourier filtering. Bottom right: Reconstructed phase shift. Note that the phase image shows more detail than the amplitude image in particular at the center of the pattern, which is mostly due to the phase shift being stronger than the amplitude attenuation for Germanium at the photon energy of 525 eV used for this experiment.

BEAMLINES
U10B, X26A

PUBLICATIONS
L.M. Miller, Q. Wang, R.J. Smith, H. Zhong, D. Elliott, and J. Warren, "A New Sample Substrate for Imaging and Correlating Organic and Trace-Metal Composition in Biological Cells and Tissues," *Anal. & Bioanal. Chem.*, **387(5)**,1705-15 (2007).

FUNDING
National Institutes of Health (NIH)
U.S. Department of Energy

FOR MORE INFORMATION
Lisa M. Miller, National Synchrotron Light Source, Brookhaven National Laboratory
lmiller@bnl.gov

A New Sample Substrate for Imaging and Correlating Organic and Trace-Metal Composition in Biological Cells and Tissues

L.M. Miller[1], Q. Wang[1], R.J. Smith[1], H. Zhong[1], D. Elliott[2], and J. Warren[3]

[1]National Synchrotron Light Source, Brookhaven National Laboratory; [2] Instrumentation Division, Brookhaven National Laboratory; [3] Center for Functional Nanomaterials, Brookhaven National Laboratory

Synchrotron-based infrared (FTIRM) and x-ray fluorescence (XRF) microscopes are complementary tools for imaging the organic and trace metal composition of biological and environmental materials, respectively, without the need for extrinsic labels or stains. However, in order to directly correlate organic composition and trace metal content, it is important to precisely overlap the IR and XRF images. We have developed a gold-patterned sample substrate, where the grid pattern is sensitive to both x-ray and infrared light, and the resulting images can be used as fiducial markers for spatially overlapping the FTIRM and XRF images from the tissue. We show that FTIRM and XRF images can be correlated precisely. By combining FTIRM and XRF microprobe imaging on the same sample utilizing this sample substrate, a more complete picture of many disease states and exposure to environmental contaminants can be achieved by directly correlating the organic and trace metal ion distribution in the tissue.

In many biological and environmental systems, organic composition and trace metal content and distribution are often highly correlated. For example, plaques in Alzheimer's diseased brain consist of both aggregates of the misfolded amyloid protein and the accumulation of metal ions such as copper and zinc. In the environment, metal-reducing bacteria and hyperaccumulating plants represent promising methods for remediation of contaminated soils.

Synchrotron-based Fourier transform infrared microspectroscopy (FTIRM) and x-ray fluorescence (XRF) microprobe are becoming increasingly popular for imaging the organic and trace metal composition of biological and environmental materials without the need for extrinsic labels or stains. FTIRM provides chemical information on the organic components of a material at a diffraction-limited spatial resolution of 2-10 μm in the mid-infrared region. XRF microprobe is a complementary technique used to probe trace element content in the same systems with a similar spatial resolution. However, most published studies utilize either FTIRM or XRF microprobe, but not both, and therefore examine only one aspect of the problem, resulting in the missing information about the relationship between the alterations of the organic and metal contents. This is likely due to technical difficulties such as sample preparation, sample substrates, and image registration.

In this highlight, we describe the development of a sample substrate that contains a gold grid pattern on its surface, which can be imaged with both the IR and XRF microscopes. The substrate consists of a metal-free glass slide that has a gold grid patterned on its surface, where the major and minor parts of the grid contain 25 and 12 nm gold, respectively. Alternate substrates can also be used including polypropylene, mylar, or silicon nitride. The sample is placed on top of the patterned substrate.

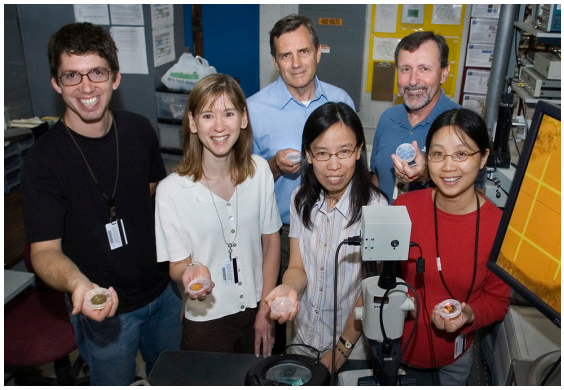

Authors (from left) Randy Smith, Lisa Miller, John Warren, Qi (Adele) Wang, Don Elliott, and Hui Zhong

The Au grid pattern can be imaged with the IR microscope because the reflectivity of gold differs as a function of thickness. The relationship between IR reflectivity and Au thickness can be seen in **Figure 1A**. Between 10 and 20 nm of Au, there is a sharp increase in reflectivity from 10% to 90%. Thus, the Au thickness for the grid pattern was chosen to be 12 – 15 nm, to provide high enough reflectivity to collect FTIRM spectra, but low enough re-

flectivity to differentiate the thick (25 nm, 100% reflectivity) from the thinner Au.

The pattern can also be imaged with the XRF microprobe because the Au fluorescence intensity is proportional to the thickness of the gold (**Figure 1B**). The integrated gold fluorescence intensity of the grid (12 nm thick gold) was approximately half of the integrated intensity from the remainder of the substrate (25 nm thick gold).

Figure 1C shows the light micrograph (top), infrared reflectivity (middle), and Au XRF fluorescence images of the substrate. From the images, it can be seen that the grid pattern's IR reflectivity image and the gold SXRF image can be used as fiducial markers for spatially overlapping the IR and XRF images from the same sample.

As an example, the sample substrate was used to study trace metal uptake in human hair. FTIRM has been shown to be a unique method for examining the chemical makeup of hair. Especially with the high-resolution of a synchrotron-based IR source, it is possible to separately analyze the different regions of the hair cross-section, i.e. the cuticle, cortex, and medulla. It has been used to study drug abuse by examining the uptake of drugs into the medulla, i.e. central core, of human hair. This technique eliminates the question of externally contaminated hair by analyzing only that portion of the hair that is formed from within the root where ingested material would be transported. FTIRM has also been used to study the effects of bleaching and coloring on different regions of the hair, and the process of ancient mummification.

Hair analysis has also frequently been used to study environmental metal contaminants such as methyl mercury uptake from eating contaminated fish, lead poisoning in children from drinking water pipes, and lead accumulation in smelter workers. Yet to date, very little work has been done comparing the organic composition of the hair with the propensity for metal uptake. By combining FTIRM and SXRF microprobe, this can be accomplished.

Figure 2A shows a cross-section of a human hair that has been embedded in paraffin wax, microtomed to a thickness of 7 µm, and deposited onto a gold-patterned substrate. The grid pattern is clearly visible under the light microscope. FTIRM analysis of the Amide I protein band (1600 – 1700 cm^{-1}) can be seen in **Figure 2D**. The protein distribution is lower in the medulla and cuticle and relatively uniform throughout the cortex of the hair.

For the SXRF microprobe images, the Cu image shows an elevated amount of Cu in the cuticle of the hair (**Figure 2E**). By overlaying the FTIRM and XRF images, results show that the elevated ring of Cu is outside of the cortex where protein concentration is lower. These findings indicate that the protein content is inversely correlated with Cu content in the hair. Since the cuticle is the outmost layer of the hair, this suggests that the elevated copper content in the cuticle is due to exogenous copper binding. Prior studies on copper content in hair have shown that damage to the cuticle of the hair can increase the cysteic acid and anionic sulfonate groups in keratin, which enhance copper adsorption. Conversely, if the metabolic levels of copper were elevated in the body, this would most likely be transported to the hair through the medulla, which was not observed in this study.

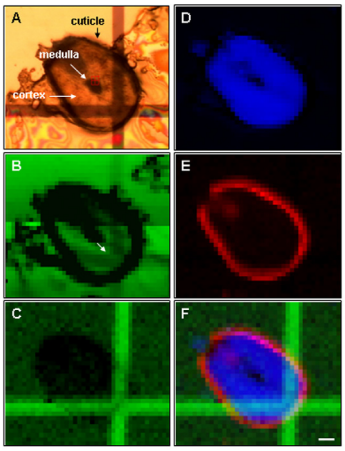

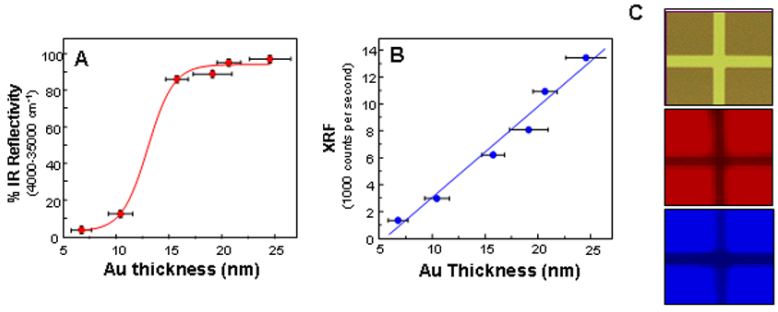

Figure 1. (A) *Infrared reflectivity of gold as a function of thickness. The substrate was produced with a bar thickness of 12 nm (~85% IR reflectivity), and the remaining part of the grid was 25 nm (100% reflectivity).* ***(B)*** *XRF intensity of gold as a function of thickness. The Au XRF intensity from the bar was approximately half the intensity from the remaining part of the grid.* ***(C)*** *visible light micrograph (top), FTIRM reflectivity image (middle), and Au XRF intensity image (bottom) from the sample substrate.*

Figure 2. (A) *Cross-section of human hair under visible light illumination. The cuticle, cortex, and medulla are indicated.* ***(B)*** *FTIRM reflectivity image of the Au grid. The white arrow indicates the grid intersection, used for the image correlation.* ***(C)*** *Au SXRF microprobe image of the Au grid.* ***(D)*** *FTIRM image of the protein content in the hair, generated by plotting the Amide I peak area from 1600 – 1700 cm^{-1}.* ***(E)*** *XRF microprobe image of copper content in the hair.* ***(F)*** *A red-green-blue (RGB) color image illustrating the correlation of the protein from FTIRM (blue channel) and Cu content from XRF microprobe (red channel) in the tissue. The gold grid pattern from SXRF microprobe is placed in the green channel. Scale bar for all images is 20 µm.*

Spreading and Surface Freezing of Nanometer-Thick Oil Films on Water

Most kindergarteners can tell you that no matter how hard you try to mix them, a droplet of oil won't spread on water. However, things are different in the nano world. Recently, a team of researchers from Durham and Oxford universities in the United Kingdom, Bar-Ilan University in Israel, and BNL used x-ray experiments at the NSLS to show that a nanometer-thick layer of oil can be induced to spread on the surface of water by a minute amount of an additive called surfactant. More intriguing, these layers exhibit a very peculiar behavior known as the surface freezing effect.

"Surface freezing is unusual because in most situations, the bulk of a material freezes before the surface," said Bar-Ilan physicist Moshe Deutsch. "You can think of it as a crowd of people standing at a concert. The people in the center are more limited in movement than the people positioned on the outside, and therefore, they'll order first. Yet, if you replace the people with molecules, the surface freezing we've observed in liquids is exactly the opposite: the molecules at the boundary order (or freeze) first while the bulk remains liquid."

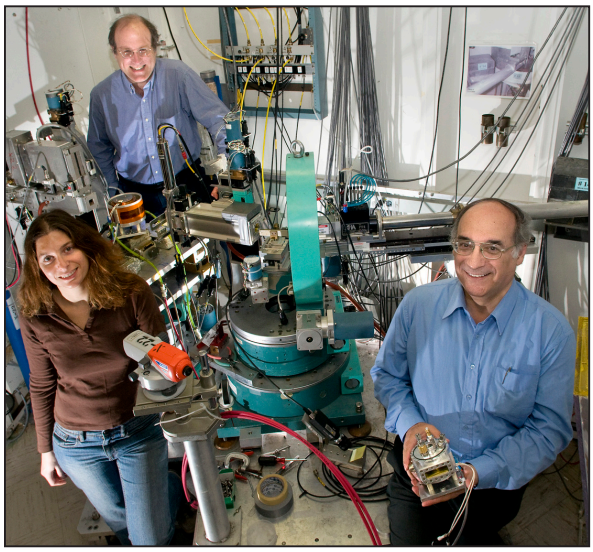

Authors (from left) Lilach Tamam, Ben Ocko, and Moshe Deutsch

Colin Bain

Eli Sloutskin

Among other applications, understanding surface freezing could be valuable to improving the function of diesel engines, which at cold climates, might be effected by the way oil is injected into the motor.

"It's such an unusual effect, and we still don't fully understand how it happens," said researcher and Durham University chemist Colin Bain.

To gain a better understanding of this phenomenon, the researchers put a drop of a liquid oil called alkane onto the surface of water containing a minute concentration of the surfactant cetyltrimethylammonium bromide (CTAB). This is not so different than making salad dressing by adding oil to vinegar – two liquids that don't naturally mix.

"If you take an oily plate and fill it with water, you'll notice these little droplets of oil on the surface," said Harvard physicist Eli Sloutskin, who took part in the study as a graduate student at Bar-Ilan. "The oil droplets won't spread. But the moment you drop a little bit of soap, which is a surfactant, on the plate, the oil droplets vanish: they spread out on the water's surface and also mix with the bulk."

On a much smaller scale than the kitchen sink, the research group determined that while an alkane won't naturally spread on water, a small amount of CTAB causes it to form a single liquid alkane layer on the surface. After the material is cooled past a certain point, the liquid layer turns crystalline. The type of crystal formed depends on whether the alkane chain is longer or shorter than the CTAB molecule's hydrocarbon tail. Using surface x-ray scattering techniques at NSLS beamline X22B, the researchers determined that if the alkane chain is shorter than the surfactant's tail, the liquid surface monolayer becomes a solid monolayer. If the alkane chain is longer, two layers form: an upper crystalline layer on top of a lower liquid one. Until now, this type of behavior has not been observed in any system.

Their results were published in the September 28, 2007 edition of *Physical Review Letters*.

"In forming these phases, spreading the oil on water and causing it to freeze as a monolayer or a double layer, we are doing nothing but self-assembly: we 'encourage' the molecules to self-organize by creating an environment that favors a particular phase," said Brookhaven physicist Ben Ocko. "We can fine tune the structure through the type of oil and surfactant used, and of course, the temperature. This is an exciting new system that certainly holds more secrets to be discovered and surprises to stumble upon. We are working hard to uncover the former, and keeping our eyes open for the latter"

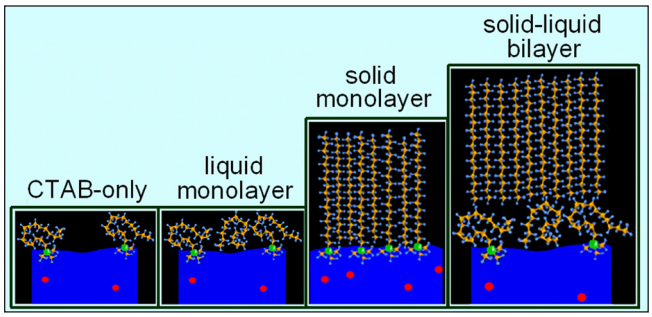

Molecular interpretations of the different phases of the alkane film on the CTAB-decorated water surface.

Other researchers involved included Zvi Sapir and Lilach Tamam (Bar Ilan), and Qunfang Lei and Katharine Wilkinson (Oxford). Funding was provided by the U.S. Department of Energy and the U.S.-Israel Binational Science Foundation.

For more information, see: E. Sloutskin, Z. Sapir, C. Bain, Q. Lei, K. Wilkinson, L. Tamam, M. Deutsch, B. Ocko, "Wetting, Mixing and Phase Transitions in Langmuir-Gibbs Films," Phys. Rev. Lett., ***99****, 136102 (2007).*

— Kendra Snyder

Featured Highlight

New DNA-Based Technique For Assembly of Nano- and Micro-sized Particles

Brookhaven scientists have developed a new method for controlling the self-assembly of nanometer and micrometer-sized particles. The method, based on designed DNA shells that coat a particle's surface, can be used to manipulate the structure – and therefore the properties and potential uses – of numerous materials that may be of interest to industry. For example, such fine-tuning of materials at the molecular level promises applications in efficient energy conversion, cell-targeted systems for drug delivery, and biomolecular sensing for environmental monitoring and medical applications.

The novel method, for which a patent application has been filed, was developed by Brookhaven researchers Mathew M. Maye, Dmytro Nykypanchuk, Daniel van der Lelie, and Oleg Gang, and is described in the September 12 online edition of *Small*, a leading journal on nanoscience and nanotechnology.

(From left) Dmytro Nykypanchuk and Mathew Maye load a sample into an atomic force microscope while Daniel van der Lelie and Oleg Gang review data at the CFN.

"Our method is unique because we attached two types of DNA with different functions to particles' surfaces," said Gang, who leads the research team. "The first type –complementary single strands of DNA – forms a double helix. The second type is non-complementary, neutral DNA, which provides a repulsive force. In contrast to previous studies in which only complementary DNA strands are attached to the particles, the addition of the repulsive force allows for regulating the size of particle clusters and the speed of their self-assembly with more precision."

"When two non-complementary DNA strands are brought together in a fixed volume that is typically occupied by one DNA strand, they compete for space," said Maye. "Thus, the DNA acts as a molecular spring, and this results in the repulsive force among particles, which we can regulate. This force allows us to more easily manipulate particles into different formations."

The researchers performed the experiments on gold nanoparticles – measuring billionths of a meter – and polystyrene (a type of plastic) microparticles – measuring millionths of a meter. These particles served as models for the possibility of using the technique with other small particles. The scientists synthesized DNA to chemically react with the particles. They controlled the assembly process by keeping the total amount of DNA constant, while varying the relative fraction of complementary and non-complementary DNA. This technique allowed for regulating assembly over a very broad range, from forming clusters consisting of millions of particles to almost keeping individual particles separate in a non-aggregating form.

"It is like adjusting molecular springs," said Nykypanchuk. "If there are too many springs, particles will 'bounce' from each other, and if there are too few springs, particles will likely stick to each other."

The method was tested separately on the nano- and micro-sized particles, and was equally successful in providing greater control than using only complementary DNA in assembling both types of particles into large or small groupings.

To determine the structure of the assembled particles and to learn how to modify them for particular uses, the researchers used transmission electron microscopy to visualize the clusters, as well as x-ray scattering at NSLS beamline X22 to study particles in solution, the DNA's natural environment.

The Office of Basic Energy Sciences within the U.S. Department of Energy's Office of Science funded this research.

For more information, see: M.M. Maye, D. Nykypanchuk, D. van der Lelie, and O. Gang, "DNA-Regulated Micro- and Nanoparticle Assembly," Small, ***3****, 1678-1682 (2007).*

— Diane Greenberg

Featured Highlight

Tiny DNA Molecules Show Liquid Crystal Phases, Pointing To New Scenario For First Life On Earth

The University of Colorado distributed the following news release about research performed in part by NSLS researchers Ron Pindak and Brandon Chapman. With a technique called microbeam x-ray diffraction, the scientists used powerful spots of light at Argonne's Advanced Photon Source to determine the structure of so-called nanoDNA – DNA molecules that are only a few nanometers in length. They found that like their longer counterparts, the nanoDNA molecules form chains that spontaneously arrange themselves into parallel strands when put in water, an orientation that is referred to as a liquid crystal phase. This discovery could provide clues about how DNA- and RNA-like molecules might have first appeared on Earth.

A team led by the University of Colorado at Boulder and the University of Milan has discovered some unexpected forms of liquid crystals of ultrashort DNA molecules immersed in water, providing a new scenario for a key step in the emergence of life on Earth.

CU-Boulder physics Professor Noel Clark said the team found that surprisingly short segments of DNA, life's molecular carrier of genetic information, could assemble into several distinct liquid crystal phases that "self-orient" parallel to one another and stack into columns when placed in a water solution. Life is widely believed to have emerged as segments of DNA- or RNA-like molecules in a prebiotic "soup" solution of ancient organic molecules.

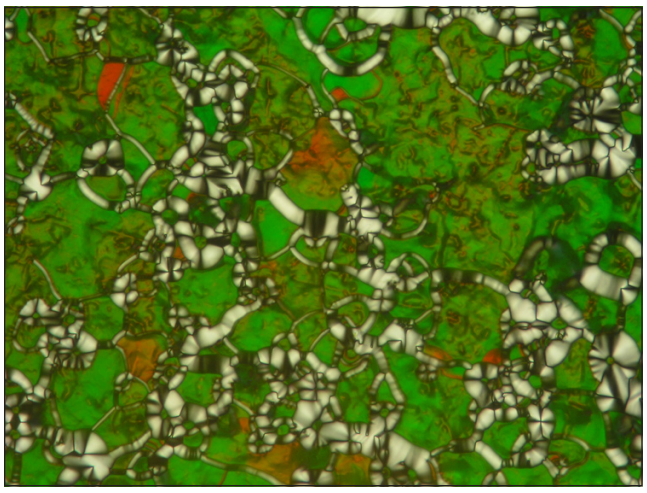

A microscope image showing that a solution of tiny DNA molecules has formed a liquid-crystal phase. The DNA molecules pair to form DNA double helices, which, in turn, stack end-to-end to make rod-shaped aggregates that orient parallel to one another. Image by Michi Nakata, University of Colorado.

A paper on the subject was published in the Nov. 23 issue of *Science*. The paper was authored by Clark, Michi Nakata and Christopher Jones from CU-Boulder, Giuliano Zanchetta and Tommaso Bellini of the University of Milan, Brandon Chapman and Ronald Pindak of Brookhaven National Laboratory and Julie Cross of Argonne National Laboratory. Nakata died in September 2006.

Since the formation of molecular chains as uniform as DNA by random chemistry is essentially impossible, Clark said, scientists have been seeking effective ways for simple molecules to spontaneously self-select, "chain-up" and self-replicate. The new study shows that in a mixture of tiny fragments of DNA, those molecules capable of forming liquid crystals selectively condense into droplets in which conditions are favorable for them to be chemically linked into longer molecules with enhanced liquid crystal-forming tendencies, he said.

"We found that even tiny fragments of double helix DNA can spontaneously self-assemble into columns that contain many molecules," Clark said. "Our vision is that from the collection of ancient molecules, short RNA pieces or some structurally related precursor emerged as the molecular fragments most capable of condensing into liquid crystal droplets, selectively developing into long molecules."

Liquid crystals – organic materials related to soap that exhibit both solid and liquid properties – are commonly used for information displays in computers, flat-panel televisions, cell phones, calculators and watches. Most liquid crystal phase molecules are rod-shaped and have the ability to spontaneously form large domains of a common orientation, which makes them particularly sensitive to stimuli like changes in temperature or applied voltage.

RNA and DNA are chain-like polymers with side groups known as nucleotides, or bases, that selectively adhere only to specific bases on a second chain. Matching, or complementary base sequences enable the chains to pair up and form the widely recognized double helix structure. Genetic information is encoded in sequences of thousands to millions of bases along the chains, which can be microns to millimeters in length.

Such DNA polynucleotides had previously been shown to organize into liquid crystal phases in which the chains spontaneously oriented parallel to each other, he said. Researchers understand the liquid crystal organization to be a result of DNA's elongated molecular shape, making parallel alignment easier, much like spaghetti thrown in a box and shaken would be prone to line up in parallel, Clark said.

The CU-Boulder and University of Milan team began a series of experiments to see how short the DNA segments could be and still show liquid crystal ordering, said Clark. The team found that even a DNA segment as short as six bases, when paired with a complementary segment that together measured just two nanometers long and two nanometers in diameter, could still assemble itself into the liquid crystal phases, in spite of having almost no elongation in shape.

Structural analysis of the liquid crystal phases showed that they appeared because such short DNA duplex pairs were able to stick together "end-to-end," forming rod-shaped aggregates that could then behave like much longer segments of DNA. The sticking was a result of small, oily patches found on the ends of the short DNA segments that help them adhere to each other in a reversible way — much like magnetic buttons — as they expelled water in between them, Clark said.

A key characterization technique employed was X-ray microbeam diffraction combined with in-situ optical microscopy, carried out with researchers from Argonne and Brookhaven National Laboratories. The team using a machine called the Argonne Advanced Photon Source synchrotron that enabled probing of the "nano DNA" molecular organization in single liquid crystal orientation domains only a few microns in size. The experiments provided direct evidence for the columnar stacking of the nano DNA pieces in a fluid liquid crystal phase.

"The key observation with respect to early life is that this aggregation of nano DNA strands is possible only if they form duplexes," Clark said. "In a sample of chains in which the bases don't match and the chains can't form helical duplexes, we did not observe liquid crystal ordering."

Subsequent tests by the team involved mixed solutions of complementary and noncomplementary DNA segments, said Clark. The results indicated that essentially all of the complementary DNA bits condensed out in the form of liquid crystal droplets, physically separating them from the noncomplementary DNA segments.

"We found this to be a remarkable result," Clark said. "It means that small molecules with the ability to pair up the right way can seek each other out and collect together into drops that are internally self-organized to facilitate the growth of larger pairable molecules.

"In essence, the liquid crystal phase condensation selects the appropriate molecular components, and with the right chemistry would evolve larger molecules tuned to stabilize the liquid crystal phase. If this is correct, the linear polymer shape of DNA itself is a vestige of formation by liquid crystal order."

For more information, see: M. Nakata, G. Zanchetta, B.D. Chapman, C.D. Jones, J.O. Cross, R. Pindak, T. Bellini, and N.A. Clark, "End-to-End Stacking and Liquid Crystal Condensation of 6– to 20–Base Pair DNA Duplexes," Science, ***318****, 1276-1279 (2007).*

— Jim Scott, University of Colorado

Hatching a New Model for Biomineralization

The idea started with an eggshell and ended with a new understanding of how minerals form to build exceptionally strong structures in the bodies of humans and other organisms. Biomineralization, the process by which organisms form materials such as bones, mollusk shells, and other structures, has captured the attention of scientists for years. Finding a way to mimic the properties of these sturdy and naturally made materials could lead to the medical engineering of replacement bone, teeth, and cartilage, as well as the development of new electronic and industrial materials. Most of the research surrounding biomineralization has looked at the multiple processes it involves and the diversity of its products. But at the NSLS, using inspiration from an egg, a team of researchers studied the earliest stages of biomineralization to find out what sets the process in motion.

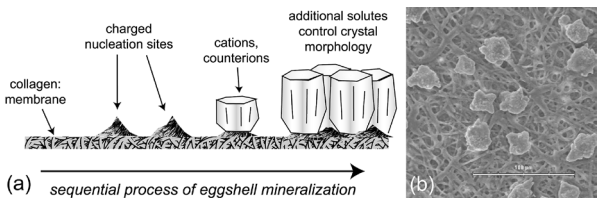

***Figure 1(a)**. The sequential mineralization stages of an eggshell. Upon the rough collagen membrane, charged sites of nucleating protein are deposited first, then exposed to calcium and carbonate to nucleate crystals. Subsequent chemical species in the fluid control the crystal growth and orientation. **(b)** Scanning electron micrograph of an eggshell membrane at the early stage, showing the fibers of collagen and the first nucleated crystals. (Courtesy of J. L. Arias, Universidad de Chile, Santiago Chile). Scale bar: 100 microns.*

A bird's eggshell is about a half-millimeter of layered calcium carbonate crystals, stabilized by a protein matrix. The shell forms during just about 12 hours of travel time through the bird's oviduct, an amazing natural feat, said NSLS physicist Elaine DiMasi, one of the authors of the biomineralization study that was published in the October 3, 2006 edition of the *Proceedings of the National Academy of Sciences*.

"It starts as a collagen membrane and goes through a series of different fluids with different species in them, and in the end, you have this hard mineral," she said. "We were looking for a system that would mimic some features of that eggshell."

To model extracellular biomineralization, the formation of materials on the outside of the cell wall, such as in the case of egg shell formation, the research team used a self-assembled protein network with both fibronetin and elastin – major connective tissue components in multicellular organisms. These proteins were incubated on negatively charged surfaces in two forms: structurally organized fibers and regions with a thin unorganized layer of protein wedged in between them.

After exposing the system to calcium carbonate for a varying set of times, the researchers used a relatively new technique called shear modulation force microscopy (SMFM) to compare the response of the two sets of protein fibers. SMFM is an atomic force microscopy-based technique in which a cantilever with a superfine tip just 40 nanometers wide is stuck into the soft material being studied. The tip is then vibrated to measure the stiffness of the material, and thus whether or not mineralization occurred on the protein fibers.

The group found that the calcium carbonate stiffened only the organized protein fibers, without affecting the unorganized regions between them. This demonstrates that mineralization requires structural organization of the protein in order to function, DiMasi said.

"It's exciting that there's a demonstration of disorganized and organized proteins side by side in the same exact environment," DiMasi said. "Any other experiment would have just inferred that an organized protein structure was necessary to nucleate, but there's never been a

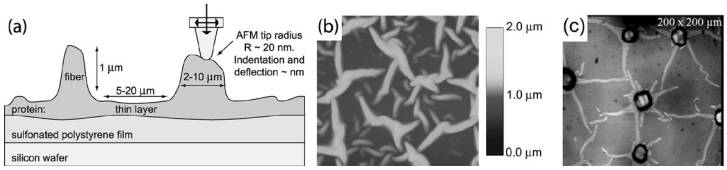

***Figure 2(a)**. Schematic of the model system showing how thin layer protein and micron fibers are layered upon the silicon wafer/sulfonated polystyrene substrate. **(b)** AFM image of the network of elastin fibers. Panel 50 microns wide. **(c)** The eggshell-mimicking result of our experiments: optical micrograph of the elastin network with calcite crystals located at the fiber vertices. Panel 200 microns wide.*

comparison like this between disorganized and organized protein."

Besides the actual results, the setup of the experiment itself, including the model system and the SMFM technique, provides valuable information for the scientific community – and not just to study eggs.

"This looks like a really good model system," DiMasi said. "Now one could take collagen and calcium phosphate and study bone nucleation or any other number of things. It just looks like a really good platform."

Other scientists involved in the study are Seo-Young Kwak (NSLS); Karthikeyan Subburaman, Nadine Pernodet, Shouren Ge, Vladimir Zaitsev, Xiaolan Ba, and Miriam Rafailovich (Stony Brook University); and Nan-loh Yang (City University of New York).

This research was funded by the National Science Foundation Materials Research and Engineering Centers and the Brookhaven National Laboratory-Stony Brook University Seed Grant Program.

For more information, see: K. Subburaman, N. Pernodet, S. Kwak, E. DiMasi, S. Ge, V. Zaitsev, X. Ba, N. Yang, and M. Rafailovich, "Templated Biomineralization on Self-Assembled Protein Fibers," Proc. Natl. Acad. Sci., ***103****, 14672-14677 (2006).*

— Kendra Snyder